AN ASSESSMENT OF THE AERODYNAMIC, THERMODYNAMIC, AND MANUFACTURING ISSUES FOR THE DESIGN, DEVELOPMENT, AND MICROFABRICATION OF A DEMONSTRATION MICRO ENGINE

by

Jonathan M. Protz

Bachelor of Science in Aeronautics and Astronautics, Massachusetts Institute of Technology, 1995
Master of Science in Aeronautics and Astronautics, Massachusetts Institute of Technology, 1997

Submitted to the Department of Aeronautics and Astronautics
in partial fulfillment of the requirements for the degree of

Doctor of Philosophy

at the

Massachusetts Institute of Technology

September 2000

Author _____
Department of Aeronautics and Astronautics
August 14, 2000

Certified by _____
Professor Alan H. Epstein
R.C. Maclaurin Professor of Aeronautics and Astronautics, Committee Chairman

Certified by _____
Professor Jack L. Kerrebrock
Professor of Aeronautics and Astronautics, Emeritus

Certified by _____
Professor S. Mark Spearing
Esther and Harold E. Edgerton Associate Professor of Aeronautics and Astronautics

Certified by _____
Professor Martin A. Schmidt
Minor Advisor, Professor of Electrical Engineering and Computer Science

Certified by _____
Professor Nesbitt W. Hagood
Chairman, Department Graduate Committee

[redacted]

AN ASSESSMENT OF THE AERODYNAMIC, THERMODYNAMIC, AND MANUFACTURING ISSUES FOR THE DESIGN, DEVELOPMENT, AND MICROFABRICATION OF A DEMONSTRATION MICRO ENGINE

by

Jonathan M. Protz

Submitted to the Department of Aeronautics and Astronautics
on September 12, 2000, in partial fulfillment of the requirements for the degree of

Doctor of Philosophy

ABSTRACT

Silicon microfabrication is an established technology for the manufacture of integrated circuits and micro-electromechanical systems (MEMS) devices such as pressure transducers and accelerometers. Recent advances in silicon microfabrication technology allow the possibility of designing high-precision mechanical devices for power conversion. Micro gas turbine engines (microengines) are one particular application of this technology. These tiny jet engines have immediate application as propulsion systems for Micro UAVs Other envisioned applications include portable electrical power generation for commercial, consumer, and military uses A microengine-based power or propulsion system could offer more than 10x the performance of a battery of the same weight. This would make it an enabling technology for long-duration portable computers, high-power mobile phones, and other portable power applications.

This thesis describes an assessment of the aerodynamic, thermodynamic, and manufacturing issues associated with the design, development, and microfabrication of an all-silicon demonstration microengine.

The design goal is the simplest feasible engine that can demonstrate the micro gas turbine engine concept. This demo microengine integrates high-speed, low Reynold's number turbomachinery, high-speed micro gas bearings, a compact hydrogen combustor, and an innovative turbine cooling scheme into a quarter-sized turbojet engine with a target thrust of 10 grams. Due to the scale of the device and the nature of the microfabrication process, the engine components are tightly coupled and the design involved a number of system trades not normally encountered in conventional engines. This thesis addresses several of these key design trades and identifies thermo-structural design and manufacturing constraints as the two principal limitations on current microengine design. The thesis also discusses the fabrication development effort and results culminating in a micro turbocharger that has been tested to speeds of up to 30,000 RPM. Rotor imbalance was identified as the probable limit on current operation.

Recommendations for future work include development of advanced turbine cooling schemes to improve device efficiency and development improved fabrication capabilities to reduce rotor imbalance.

Thesis Supervisor: Professor Alan Epstein
Title: R.C. Maclaurin Professor of Aeronautics and Astronautics

ACKNOWLEDGEMENTS

This thesis would not have been possible without the support and encouragement of a great many people.

I would first like to thank my family: my parents for giving me the opportunity to attend MIT in the first place and for giving me their constant support throughout school, and my brother, Chris Protz, for his encouragement and good humor while I worked on my thesis.

I would like to thank my advisor, Prof. Alan Epstein, for offering me the opportunity to work on the microengine as the 'project engineer' in the first place. This program provided many more learning experiences and opportunities than a typical PhD program would and I am grateful. I would also like to thank the other members of my committee, Prof. Mark Spearing, Prof. Jack Kerrebrock, and Prof. Marty Schmidt for their support particularly as my defense date drew near. I would also like to thank Prof. Ian Waitz, Prof. Kenny Breuer and all of the other faculty members and research staff involved with the project for their invaluable advice and assistance.

The engine design is the product of a terrific team of students and researchers. Dr. Stu Jacobson helped with the overall design and offered extremely valuable assistance with the experiments. Kuo-Shen Chen, Wenjing Ye, Dr. Eugene Huang, Kevin Lohner, and Bruno Miller carried out all of the detailed structural design work. Dr. Stu Jacobson, Prof. Kenny Breuer, Dr. Fred Ehrich, DJ Orr, and Ed Piekos helped identify bearing concepts and performed all of the bearing analysis. Amit Mehra, Steve Lukachko, Dr. Chris Cadou, Chris Spadaccini, Jin-Wook Lee, and Sumita Pennathur researched combustion and developed a 'hot static structure' based on the demo engine design. Dr. Choon Tan, Dr. Stu Jacobson, Dr. Harold Youngren, and Dr. Yifong Gong, Greg Shirley, and Kashif Khan worked on the turbomachinery design and testing. Chunmei 'May' Liu analyzed the microengine dynamics. Maddie Close cross-sectioned and epoxied the dies. Todd Harrison took care of all packaging needs. Many other students and researchers contributed ideas and suggestions based on their work with related devices and I would like to thank them as well.

In particular, I would like to thank Adam London, Luc Frechette, and CC Lin for their overall design advice. I would also like to wish the best of luck to follow on team of microengine students including Nick Savoulides, Baudoin Philippon, Dongwon Choi, Hyung-Soo Moon, and Chee Wei Wong.

The turbocharger and demo engine would never have been built were it not for the efforts of an outstanding microfabrication team. Dr. Arturo Ayon, Dr. Xin Zhang, and Dr. Ravi Khanna gave strong advice, helped identify and solve a host of fabrication problems, and carried out much of the fabrication effort themselves. Tom Takacs and Dennis Ward did the heavy lifting and made outstanding observations that greatly accelerated a sometimes frustrating fabrication process. Together this team built all of the devices described in this thesis.

Jimmy Letendre, Victor Dubrowski, and Bill Ames constructed all of the testing apparatus and made all necessary emergency repairs to the test facility. Their efforts are greatly appreciated. Thanks to Diana Park who drew many fine demo engine illustrations, several of which are presented here. I would also like to thank Anne Maynard and Holly Anderson for always making sure my stipend money was available.

Working on a project of this unique stature and nature also provided me with the opportunity to participate in the MIT $50K Entrepreneurship Competition. This was a very rewarding experience and I wish to thank Luc, Adam, Amit, Lee, Joe, Nick, Jeff, Diego, Chee Wei, and all of my '99 and '00 $50K team members for their participation. I would also like to thank Heather Wilding, the '00 $50K lead organizer, for encouraging us to enter and Sachin, the '99 communications coordinator for getting us into Newsweek.

Thanks to all of the students and staff of the GTL for making this a fun and rewarding experience.

This work was supported in part by a National Defense Science and Engineering Fellowship from the DoD. It was also sponsored by the United States Army Research Office, Dr. R. Paur and Dr. T. Doligalski, technical managers and by DARPA, Dr. R. Nowak, Dr. D. Fields and Dr. S. Wilson, program managers. This support is gratefully acknowledged.

CONTENTS

LIST OF FIGURES

LIST OF TABLES

CHAPTER 1

INTRODUCTION

This chapter introduces the microengine concept and motivates the demo engine research effort.

1.1 BACKGROUND

In 1994, Epstein *et al* [1] proposed the concept of a centimeter-scale gas turbine engine manufactured from refractory ceramic materials using semiconductor fabrication techniques. Figure 1-1 illustrates this concept. This initial concept led to a comprehensive multidisciplinary research program at MIT that is focused on developing all of the fundamental technologies required to build such a device. These technologies include modeling and micro-fabrication of high-speed turbomachinery, high-speed gas bearings, compact combustion systems, high-power micro electrical motors and generators, high-temperature micro-scale packaging, high-performance structures, and advanced materials. These fundamental technologies have a broad range of applications including jet engines for propulsion, gas turbine engines for electrical power generation, motor-driven compressors for fluidic pumping and pressurization, micro-coolers for microchip cooling, and micro-rockets for small-scale space propulsion. The reader interested in learning more about the background of the research program and its practical applications can consult numerous articles in the academic [1,2,3,4] and popular [5,6,7] literature.

Even at a conventional scale, aircraft gas turbine engine design is among the most challenging of engineering design problems. A gas turbine engine involves many individual components that must operate together in a reliable manner at high rotational speeds and temperatures. This makes the design problem highly interdisciplinary. Fluid dynamic, thermodynamic, and structural concerns must be satisfied simultaneously for every mechanical component. Electrical

components such as the ignition system, starter motor, and electrical generator must operate efficiently and reliably at elevated temperatures. For flight applications, these components must be lightweight and extremely rugged. All of this must be done within the constraints of a realizable manufacturing process.

The microengine is a micro electro-mechanical system (MEMS) device. MEMS design is also highly interdisciplinary. A common MEMS device such as a simple pressure transducer can involve the design and analysis efforts of a structural engineer, packaging engineer, circuit designer, controls engineer, and fabrication engineer. Component design is tightly coupled in a MEMS device to simplify the fabrication process and reduce the device size. In many cases, portions of a MEMS device must serve dual roles, serving as both mechanical and electrical components. Small length scales make component thermal and mechanical isolation extremely challenging.

Microengines represent the combination of both gas turbine engine and MEMS device design. As such, they span many fields of research including turbomachinery design, combustion, bearings and rotor dynamics, thermal and structural design, materials, electrical systems, and micro fabrication.

1.2 DEMO ENGINE RESEARCH

In 1997, MIT embarked on an effort to integrate fundamental microengine technologies into a working jet engine for demonstration purposes. This 'demo engine' is an all-silicon, hydrogen-fueled engine designed for simplicity and minimum technical risk. The fundamental research goal of the demo engine is to *identify the critical integration issues* associated with the microengine concept. These issues are driven by the integrated nature of the device and are separate from the research issues associated with each fundamental component technology. In addition, the demo engine will serve as the foundation for further development efforts aimed at small aircraft propulsion and portable electrical power generation.

The demo engine design is illustrated in Figures 1-2, and 1-3. The engine is a 2.1 cm square, 3.3 mm thick, all-silicon design with an 8 mm diameter compressor and a 6 mm diameter turbine spinning at 1.2 million RPM. The compressor and turbine blades are each designed to be 400 um

tall[1]. The compressor has a design pressure ratio of 1.8 and a design efficiency of 0.50. The combustor is designed for operation at 1600 K. The rotating turbomachinery is supported by a set of hydrostatic gas bearings that bleed 5% of the compressor flow. The engine's static and rotating structures are designed to operate at 1200 K and 950 K respectively.

The demo engine is designed to ingest 0.36 grams/sec of air, producing approximately 10 grams of thrust while consuming 16 grams/hour of hydrogen fuel. The engine has a predicted overall thermal efficiency of 2%.

The demo engine is fabricated from silicon using MEMS semiconductor microfabrication techniques. Each engine is assembled from six 10 cm diameter single-crystal silicon wafers that are etched to define features and then bonded together to form complete engines. Each wafer corresponds to one or more engine components. The bonded set of wafers is then cut into ten individual engines (called 'dies'). Figure 1-5 illustrates the fabrication concept.

1.3 OBJECTIVE AND APPROACH

The objective of the research presented here is to evaluate the feasibility of an all-silicon micro gas turbine engine. Three primary questions were considered:

(1) Is it possible to synthesize a closed-cycle demonstration engine design using the current state-of-the art design and analysis knowledge? To which parameters is the design most sensitive? What are the major integration issues?

(2) Can this design be fabricated using available state-of-the art microfabrication technology? What new fabrication capabilities, if any, would be required to achieve the design intent?

(3) Does the fabricated device deliver the intended performance? If not, what changes to the design or the fabrication are necessary to achieve the intended performance?

In order to answer these questions, the following steps were taken:

---

[1] The engine as finally fabricated had 200 um tall compressor and turbine blades. See Chapters 2 and 4 for details.

(1) An integrated, all-silicon, demonstration microengine was designed using the best available knowledge about micro-scale turbomachinery, bearings, combustion, structures, materials, and fabrication. This 'baseline' design was studied analytically to determine the impact of various design parameters on overall engine performance.

(2) A process flow to fabricate the engine was designed. This process was executed in MIT's Microsystem Technology Laboratory by MIT microfabrication experts. The design was modified as necessary to allow fabrication with available tools and techniques.

(3) Initial experiments were conducted with the fabricated devices to determine their operating limits, compare these limits to analytical predictions, and isolate areas of the design that require additional effort.

These steps represent the beginning of a complete development process. Future work should focus on realizing the design intent with the fabrication and on testing such devices to determine how the component performance compares to theory.

1.4 APPLICATIONS OF RESEARCH

If successful, microengines would represent a quantum leap in compact power generation. Such devices would have major performance advantages over traditional compact power sources such as conventional gas turbine engines, diesel engines, fuel cells, and batteries.

In comparison to conventional engines, microengines offer more power per unit weight. Microengines benefit from the cube-square law. The weight of a gas turbine engine scales with its volume while its power output scales with the area of its inlet. Therefore, all else being equal, the power-to-weight ratio of the engine scales inversely with its size. Smaller engines have higher power-to-weight ratios. A microengine could conceptually offer 10-100 times the power to weight ratio of a conventionally sized gas turbine engine [1]. In addition, microengines are better suited to produce power at a small scale. With an appropriate integrated electrical generator, a centimeter-sized microengine could produce between 10 and 25 Watts of electrical power. This makes them well suited for portable electronics and portable computing

applications. At the same time, many microengines can be ganged together to provide power at the kilowatt level for distributed residential power or to power automobiles and similar vehicles.

Microengines also offer benefits over batteries. Unlike batteries, which are closed chemical systems, microengines are mechanical heat engines that generate power by converting the energy of a fuel burning with air into mechanical or electrical power. The energy released by burning a hydrocarbon fuel (~43.3 MJ/kg) is much larger than the energy released in the chemical reactions of a battery (~0.5 MJ/kg). In addition, the oxygen used in the reaction is supplied by the ambient air. Due to the small scale of microengines, the weight of a microengine electrical power system is dominated by the weight of the fuel. Even if a microengine had a thermal efficiency as low as 5%, it would still offer an energy density 5-25 times better than today's batteries [1].

Turbojet propulsion of micro air vehicles is one specific application for microengine devices. In conjunction with its microengine research effort, MIT has undertaken an effort to develop a six-inch wingspan, jet-propelled micro air vehicle, illustrated in Figures 1-6 and 1-7. This aircraft is designed for a flight speed of 30 m/sec and a range of 30 km. For micro flight applications, a turbojet microengine eliminates the batteries, power electronics, and motor inefficiencies of a traditional motor-driven propeller approach. As part of the present work, the author conducted a system study comparing the performance of a turbojet powered MAV to a battery-powered MAV. The study, detailed in Appendix A, showed that microengines offer a substantial performance improvement over batteries. This performance improvement is illustrated in Figure 1-8.

1.5 Previous Work

As mentioned above, the development of the demo microengine is part of a comprehensive MIT effort covering all aspects of microengine technology. As such, the demo engine research is built on a large body of prior work in the field. The previous work fits into seven major areas of research, each addressing a specific aspect of microengine technology. These areas are: (1) systems integration, (2) thermal, structural, and material design, (3) combustion, (4) turbomachinery and fluid dynamics, (5) bearing design and rotor dynamics, (6) electrical machinery, and (7) fabrication. The previous work in each area is summarized below.

In addition, various aspects of microengine technology are covered under US Patent US5932940.

Systems Integration

Epstein initially proposed the microengine concept [1,2]. Groshenry studied the overall system [8]. This work laid the foundation for the demo engine, defining the initial geometry with its gas bearings, radial turbomachinery, and integrated combustor. This initial design was extended into a baseline gas turbine electrical generator concept presented in [1,2]. Esteve studied the role of the secondary flow system for this design [9]. Liu studied the dynamic response of microengines in general and found that fluid-thermo-structural coupling significantly altered the dynamics [10].

The baseline design of [1,2] was for a simple cycle, single-spool, single stage engine with a shrouded compressor and an integrated electrical generator/starter. The design had a nominal thickness of 3 mm, a die size of 10 mm, compressor and turbine diameters of 4 mm, and a journal bearing shaft diameter of approximately 900 um. There were eight wafers varying in thickness from 200 um to 800 um; one each for the fuel manifold, electrical generator/starter, compressor, gas bearing system, turbine, and exhaust nozzle. The combustor was made up of a combination of these wafers. The engine was designed to deliver a core mass flow of 0.16 g/sec at a pressure ratio of 4:1, with a compressor tip speed of 500 m/sec, a rotor speed of 2.4 million RPM, and a turbine inlet temperature of 1600K. The design called for silicon carbide as a structural material. The gas bearing system involves an eccentric hydrodynamic journal bearing along the spool shaft and hydrodynamic thrust bearings on the compressor and turbine disk backsides.

A number of researchers have considered other devices based on high-speed micro turbomachinery. These include motor-driven pumps [11,12] and micro rockets [13,38,15,16]. These devices laid some of the fabrication foundations for the demo engine design.

Thermal, Structural, and Materials Design

In order to achieve high pressure ratios and efficiencies, microengines must operate at the high temperatures (1400-2000 K gas and 800-1600 K structural), tip speeds (~500 m/sec), and stresses (100s of MPa) of conventional turbomachines. At the same time, the engine must use materials such as silicon that can be easily microfabricated. This requires precision structural analysis techniques and advanced materials. The thermal, structural, and fluidic analyses of a microengine are also tightly coupled, making the thermal design a challenging problem. Chen undertook a

comprehensive study of the material and structural issues of microengine design [17]. Chen especially focused on silicon as a material, performing much of the demo engine structural analysis [19,20]. Huang and Ye continued Chen's structural and thermal analysis, analyzing the design presented here [70,71]. Lohner studied silicon carbide and other advanced materials and showed that carbide could be incorporated into a silicon structure [22]. Miller extended Chen's work with silicon and Lohner's work with silicon carbide, developing the concept of a hybrid carbide/silicon structure [23]. Moon and Choi, are continuing work on a silicon carbide engine [24,25].

Combustion

Microengines are internal combustion engines requiring air ingestion, fuel injection, fuel-air mixing, and chemical reaction (combustion) of the fuel-air mixture. The combustion process is dominated by the need to mix and react the fuel within the time the flow is resident in the combustor. Because the chemical reaction times are independent of scale, this makes micro-scale combustion a challenging problem. Tzeng and Gauba first demonstrated pre-mixed combustion of hydrogen at micro-engine scales in a centimeter-scale steel and quartz combustor [26,27,28]. Mehra extended these results to a microfabricated silicon combustor [29,30]. Mehra also demonstrated hydrogen combustion in a microfabricated silicon 'hot static structure' that reflected the static structure of the demo engine [29,31,32,33]. Lee performed CFD studies of Mehra's rig [34]. Cadou and Spaddacinni are extending Mehra's results to hydrocarbon combustion with and without catalysts [35, 36].

Turbomachinery and Fluid Dynamics

Due to its small scale, microengine turbomachinery operates in laminar and transitional flow regimes with high heat transfer coefficients. The chord-based Reynolds number for the demo engine compressor is approximately 20,000. The heat transfer coefficients are in the range of 2000 W/m^2-K. In addition, microfabrication constraints lead to a very two-dimensional compressor geometry. Microengine turbomachinery was initially studied by Jacobson *et al* [37]. Mehra extended Jacobson's 2D CFD calculations to 3D [38,39]. Gong extended Mehra's compressor calculations to include the effects of heat transfer [40]. Phillipon is extending Mehra's turbine calculations to include high-temperature flows with heat transfer [41]. Jacobson,

Shirley, Khan, and Cadou studied micro turbomachinery in a dynamically scaled, conventionally sized, 'macro-rig' experimental facility [37,42,43,44].

Bearing Design and Rotor Dynamics

Microengines require low-friction bearings to support the rotating machinery against the rotor-dynamic loads experienced from running at millions of RPM. Orr, Piekos, Savoulides, Jacobson, Breuer, Ehrich, *et al* have studied gas bearings for microengines [45, 46, 47, 48, 49, 50]. These bearings operate in physical regimes well outside established bearing theory, requiring the development of new experimental and analytical models for bearing behavior. Orr demonstrated both hydrostatic and hydrodynamic gas bearings in a dynamically-scaled 'macro bearing rig' and identified rotor imbalance as a critical issue [45]. Lin, Wong, Frechette, Jacobson, *et al* demonstrated high-speed operation of a microfabricated bearing test rig [51, 52, 53, 54].

Electrical Machinery

The demo engine research presented here focuses on a turbojet engine without electrical generating capability. Ultimately, however, a complete gas turbine electrical generator would require an integrated electrical generator. The generator could also be run as a motor to make a motor-driven pump. Nagle designed and tested a non-rotating electrostatic 'tethered motor' to demonstrated microfabricated electrical machinery [55]. Frechette [11] designed and tested a microfabricated motor-driven compressor based on the microfabricated bearing device of Lin [51]. Livermore [56] is currently developing a metal-process, microfabricated electrical generator based on the work of [11]. Koser, Allen, *et al* are developing a microfabricated electromagnetic motor [57]. In addition, much of the research on microengine fabrication technology has focused on the electrical motor and generator.

Fabrication

Microengines are MEMS devices built using semiconductor fabrication technology for precision fabrication and batch processing. A number of researchers including Ayon, Zhang, Khanna, Ghodssi, and others have undertaken extensive efforts to develop deep etching and bonding processes for microengine fabrication [58, 59, 60, 61, 62, 63, 64, 65, 66, 67]. This work includes high precision, 300 um deep etches for gas bearing fabrication, 200 um and 400 um deep etches for turbomachinery blading, and multiple-wafer bonding processes. Harrison [68] studied glass-

bead micro packing for fluidic interconnects. Mehra studied electrical interconnects [69]. Lin [51], Frechette [11], Mehra [29], London [13], and Nagle [55] also performed considerable process development for their respective microengine-related devices.

1.6 ORGANIZATION OF THESIS

This chapter introduced the microengine concept and motivated the development and testing of a demonstration microengine. Subsequent chapters describe the demo engine design, development, and testing in detail.

Chapter Two presents the overall system design and layout of the demonstration engine. The chapter addresses issues of performance and mechanical design. It focuses on the impact of component behavior on overall system performance.

Chapter Three presents the individual component designs. The chapter summarizes the fundamental engineering issues associated with each component and addresses the impact of overall system requirements on individual component behavior.

Chapter Four describes the demo engine fabrication development effort. The chapter documents the fabrication process, identifies the important fabrication issues that are unique to the demo engine design, and summarizes the impact of fabrication capabilities on overall system design and performance.

Chapter Five describes the experimental setup used for testing the demo engine and related turbocharger devices.

Chapter Six describes the experimental results from tests that have been performed with the fabricated demo engine and turbocharger devices. The turbocharger devices reached a speed of 20,000 rpm and demonstrated behavior consistent with theoretical and empirical predictions. These experiments constitute the first successful operation of a two-wafer micro turbomachine.

Chapter Seven concludes the thesis by summarizing the demo engine research to date and identifying areas of focus for future research.

1.7 REFERENCES

[1] A. H. Epstein, Senturia, Anathasuresh, Ayon, Breuer, Chen, Ehrich, Esteve, Gauba, Ghodssi, Groshenry, Jacobson, Lang, Lin, Mehra, Mur Miranda, Nagle, Orr, Piekos, Schmidt, Shirley, Spearing, Tan, Tzeng, Waitz, "Power MEMS and Microengines," presented at IEEE Conference on Solid State Sensors and Actuators, Chicago, IL, June 1997.

[2] A. H. Epstein, Senturia, Al-Midani, Anathasuresh, Ayon, Breuer, Chen, Ehrich, Esteve, Frechette, Gauba, Ghodssi, Groshenry, Jacobson, Kerrebrock, Lang, Lin, London, Lopata, Mehra, Mur Miranda, Nagle, Orr, Piekos, Schmidt, Shirley, Spearing, Tan, Tzeng, Waitz, "Micro-Heat Engines, Gas Turbines, and Rocket Engines", AIAA 97-1773, 28th AIAA Fluid Dynamics Conference, 4th AIAA Shear Flow Control Conference, Snowmass Village, CO, June 29-July 2, 1997.

[3] A. H. Epstein, S. A. Jacobson, J. M. Protz, L. G. Frechette, "Shirtbutton-Sized Gas Turbines: The Engineering Challenges of Micro High Speed Rotating Machinery," Plenary Lecture, 8th International Symposium on Transport Phenomena and Dynamics of Rotating Machinery (ISROMAC-8), Honolulu, HI, March 2000.

[4] A. H. Epstein, S. A. Jacobson, J. M. Protz, C. Livermore, J. Lang, M. A. Schmidt, "Shirtbutton-Sized, Micromachined, Gas Turbine Generators," presented at 39th Power Sources Conference, Cherry Hill, NJ, June 2000.

[5] A. H. Epstein, "The Inevitability of Small," *Aerospace America*, March 2000, pp. 30-37

[6] A. H. Epstein and S. D. Senturia, "Macro Power from Micro Machinery," *Science*, p. 1211, Vol. 276, 23 May 1997

[7] S. Ashley, "Turbines on a Dime," *Mechanical Engineering*, pp. 78-81, October 1997.

[8] C. Groshenry, "Preliminary Design Study of a Micro-Gas Turbine Engine." MS Thesis, MIT, Department of Aeronautics and Astronautics, 1995.

[9] E. Esteve, "Secondary Flow System Modeling," Technical Report, MIT GTL, 1996.

[10] C. Liu, MS Thesis, MIT, Department of Aeronautics and Astronautics, 2000.

[11] L. Frechette, *Development of a Silicon Microfabricated Motor-Driven Compressor*, PhD Thesis, MIT, Department of Aeronautics and Astronautics, 2000

[12] L. G. Frechette, S. A. Jacobson, K. S. Breuer, F. F. Ehrich, R. Ghodssi, R. Khanna, C. W. Wong, X. Zhang, M. A. Schmidt, A. H. Epstein, "Demonstration of a Microfabricated High-Speed Turbine Supported on Gas Bearings," presented at Solid-State Sensor and Actuator Workshop, Hilton Head Island, SC, June 2000.

[13] A. P. London, *Development and Test of a Microfabricated Bi-Propellant Rocket Engine*, PhD Thesis, MIT, Department of Aeronautics and Astronautics, 2000.

[14] A. P. London, "A Systems Study of Propulsion Technologies for Orbit and Attitude Control of Microspacecraft," MS Thesis, MIT, Department of Aeronautics and Astronautics, 1996.

[15] R. L. Bayt, *Analysis, Fabrication, and Testing of a MEMS-Based Micropropulsion System*, PhD Thesis, MIT, Department of Aeronautics and Astronautics, 1999.

[16] C. S. Protz, "Systems Analysis of a Microfabricated Storable Bipropellant Rocket Engine," MS Thesis, MIT, Department of Aeronautics and Astronautics, 2000.

[17] K. S. Chen, *Materials Characterization and Structural Design of Ceramic Micro Turbomachinery*, PhD Thesis, MIT, Department of Aeronautics and Astronautics, 1999.

[18] S. M. Spearing, K. S. Chen, "Micro-Gas Turbine Engine Materials and Structures", presented at 21st Annual Cocoa Beach Conference and Exposition on Composite, Advanced Ceramics, Materials and Structures, January 1997.

[19] K-S Chen, A. A. Ayon, K. L. Lohner, M. A. Kepets, T. K. Melconian, and S. M. Spearing, "Dependence of Silicon Fracture Strength and Surface Morphology on Deep Reactive Ion Etching Parameters", presented at the MRS fall Meeting, Boston, MA, December 1998.

[20] K-S Chen, A. Ayon, and S. M. Spearing, "Silicon Strength Testing for Mesoscale Structural Applications", *MRS Proceedings*, Vol. 518, 1998, pp. 123-130.

[21] K-S Chen, A. Ayon, and S. M. Spearing, "Controlling and Testing the Fracture Strength of Silicon at the Mesoscale", *Journal of the American Ceramic Society*, 1999.

[22] K. A. Lohner, "Microfabricated Refractory Ceramic Structured for Micro Turbomachinery," MS Thesis, MIT, Department of Aeronautics and Astronautics, 1999.

[23] B. Miller, "Hybrid Silicon/Silicon Carbide Microstructures and Silicon Bond Strength Tests for the MIT Micorengine," MS Thesis, MIT, Department of Aeronautics and Astronautics, 2000.

[24] H. S. Moon, Personal Communication, MIT GTL, 2000, To be published in MIT PhD thesis

[25] D. Choi, Personal Communication, MIT GTL, 2000, To be published in MIT PhD thesis

[26] Y-S Tzeng, "An Investigation of Microcombustion Thermal Phenomena," MS Thesis, MIT, Department of Aeronautics and Astronautics, 1997.

[27] I. A. Waitz, G. Gauba, Y-S Tzeng, "Combustion for Micro-Gas Turbine Engines," *ASME J. of Fluid Eng.*, Vol. 120, March, 1998.

[28] I. A. Waitz, G. Gauba, and Y-S Tzeng, "Combustors for Micro-Gas Turbine Engines," *Proc. of the International Mechanical Engineering Congress and Exposition*, November 1996.

[29] A. Mehra, *Development of a High Power Density Combustion System for a Silicon Micro Gas Turbine Engine*, PhD thesis, MIT, Department of Aeronautics and Astronautics, 2000.

[30] Mehra and I. A. Waitz, "Development of a Hydrogen Combustor for a Microfabricated Gas Turbine Engine", Solid-State Sensor and Actuator Workshop, Hilton Head Island, SC, June 1998.

[31] A. Mehra, I. A. Waitz, and M. A. Schmidt, "Combustion Tests in the Static Structure of a 6-Wafer Micro Gas Turbine Engine," 1999 Solid State Sensor and Actuator Workshop, June 2-4, 1999.

[32] A. Mehra, A. A. Ayon, I. A. Waitz, and M. A. Schmidt, "Microfabrication of High Temperature Silicon Devices Using Wafer Bonding and Deep Reactive Ion Etching", *IEEE/ASME Journal of Microelectromechanical Systems*, Vol. 8, No. 2, June 1999, pp. 152-160.

[33] Mehra, X. Zhang, A. A. Ayon, I. A. Waitz, M. A. Schmidt and A. H. Epstein, "A 6-Wafer Combuston System for a Silicon Micro gas Turbine Engine," submitted to the *Journal of Micro Electro Mechanical Systems.*

[34] J-W. Lee, Personal Communication, MIT GTL, 2000, To be published in MIT MS thesis

[35] C. M. Spadaccini, Personal Communication, MIT GTL, 2000, To be published in MIT PhD thesis

[36] C. Cadou, Personal Communication, MIT GTL, 2000.

[37] S. A. Jacobson, "Aerothermal Challenges in the Design of a Microfabricated Gas Turbine Engine", AIAA 98-2545, 29th AIAA Fluid Dynamics Conference, Albuquerque, NM, June 1998.

[38] A. Mehra, "Computational Investigation and Design of Low Reynolds Number Micro-Turbomachinery," MS Thesis, MIT, Department of Aeronautics and Astronautics, 1997.

[39] A. Mehra, S. A. Jacobson, C. S. Tan, and A. H. Epstein, "Aerodynamic Design Considerations for the Turbomachinery of a Micro Gas Turbine Engine", presented at the 25th National and 1st International Conference on Fluid Mechanics and Power, New Delhi, India, December 1998.

[40] Y-F Gong, Personal Communication, MIT GTL, 2000.

[41] Baudoin Phillippon, Personal Communication, MIT GTL, 2000, To be published in MIT MS thesis.

[42] G. Shirley, "An Experimental Investigation of a Low Reynolds Number, High Mach Number Centrifugal Compressor," MS Thesis, MIT, Department of Aeronautics and Astronautics, 1998.

[43] K. Khan, Personal Communication, MIT GTL, 2000. To be published in MIT PhD thesis

[44] C. Cadou, Personal Communication, MIT GTL, 2000.

[45] D. J. Orr, *Macro-Scale Investigation of High Speed Gas Bearings for MEMS Devices.* PhD thesis, MIT, Department of Aeronautics and Astronautics, February 2000.

[46] E. S. Piekos, *Numerical Simulation of Gas-Lubricated Journal Bearings for Microfabricated Machines.* PhD thesis, MIT, Department of Aeronautics and Astronautics, February 2000.

[47] E. S. Piekos, D. J. Orr, S. A. Jacobson, F. F. Ehrich, and K. S. Breuer, "Design and Analysis of Microfabricated High Speed Gas Journal Bearings," AIAA Paper 97-1966, 28th AIAA Fluid Dynamics Conference, Snowmass Village, CO, June 29-July 2, 1997.

[48] E. S. Piekos and K. S. Breuer. "Pseudospectral Orbit Simulation of Non-Ideal Gas-Lubricated Journal Bearings for Microfabricated Turbomachines," Paper No. 98-Trib-48, presented at the Tribology Division of The Americal Society of Mechanical Engineers for presentation at the Joint ASME/STLE Tribology Conference, Toronto, Canada, October 1998. Also, to appear in *Journal of Tribology.*

[49] D. J. Orr, and S. A. Jacobson, "High Order Galerkin Models for Gas Bearings," submitted to the *Proceedings of the ASME/STLE Tribology Conference*, paper ASME/2000-TRIB-131, Seattle, WA, October 2000.

[50] N. Savoulides, "Low Order Models for Hybrid Gas Bearings," MS thesis, MIT, Department of Aeronautics and Astronautics, February 2000.

[51] C. C. Lin, *Development of a Microfabricated Turbine-Driven Air Bearing Rig.* PhD thesis, MIT, Department of Mechanical Engineering, 1999.

[52] C. C. Lin, R. Ghodssi, A. A. Ayon, D. Z. Chen, S. A. Jacobson, K. S. Breuer, A. H. Epstein and M. A. Schmidt, "Fabrication and Characterization of a Micro Turbine/Bearing Rig", presented at MEMS '99, January 1999, Orlando, FL.

[53] Frechette, L.G, Jacobson, S.A., Breuer, K.S., Ehrich, F.F., Ghodssi, R., Khanna, R., Wong, C.W., Zhang, X., Schmidt, M.A. and Epstein, A.H., "Demonstration of a Microfabricated High-Speed Turbine Supported on Gas Bearings," presented at Solid-State Sensor and Actuator Workshop, Hilton Head Island, SC, June 2000.

[54] C. Wong, Personal Communication, MIT GTL, 2000. To be published in MIT MS thesis

[55] S. Nagle, Personal Communication, MIT GTL, 2000, To be published in MIT PhD thesis.

[56] C. Livermore, Personal Communication, MIT GTL, 2000.

[57] H. Koser, Personal Communication, MIT GTL, 2000. To be published in MIT thesis.

[58] A. A. Ayón, Lin, C.C., Braff, R., Bayt, R., Sawin, H.H. and Schmidt, M., "Etching Characteristics and Profile Control in a Time Multiplexed Inductively Coupled Plasma Etcher," 1998 Solid State Sensors and Actuator Workshop, Hilton Head, SC, June 1998.

[59] A. A. Ayón, Ishihara, K., Braff, R., Sawin, H.H. and Schmidt, M., "Deep Reactive Ion Etching of Silicon," Invited Presentation at Materials Research Society Fall Meeting, Boston, MA, November 30-December 4, 1998.

[60] Mirza, A.R. and Ayón, A.A., "Silicon Wafer Bonding: Key to MEMS High-Volume Manufacturing," *SENSORS*, Vol. 15, No. 12, December 1998, pp. 24-33.

[61] A. A. Ayon, Ishihara, K,. Braff, R.A., Sawin, H.H., Schmidt, M.A., "Microfabrication and Testing of Suspended Structures Compatible with Silicon-on-Insulator Technology", submitted to the *Journal of Vacuum Science and Technology*, February 1999.

[62] Ayón, A.A., Epstein, A.H., Frechette, L., Nagle, S. and Schmidt, M. A., "Tailoring and Controlling Etch Directionality in a Deep Reactive Ion Etching Tool," submitted to Transducers'99, Sendai, Japan, June 1999.

[63] A. A. Ayón, Chen, D.-Z., Braff, R. A., Khana, R., Sawin, H. H., Schmidt, M. A., "A novel Integrated Process Using Fluorocarbon Films Deposited with a Deep Reactive Ion Etching (DRIE) Tool," Fall Meeting of the Materials Research Society, Boston, MA , November 29 - December 3, 1999.

[64] A. A. Ayón, Braff, R.A., Bayt, R., Sawin, H.H., Schmidt, M.A., "Influence of Coil Power in the Etching Characteristics in a High Density Plasma Etcher," *Journal of the Electrochemical Society*, Vol. 146, No. 7, 1999.

[65] A. A. Ayón, X. Zhang and R. Khanna, "Ultra Deep Anisotropic Silicon Trenches Using Deep Reactive Ion Etching (DRIE)," 2000 Solid State Sensors and Actuator Workshop, Hilton Head, SC, June 2000.

[66] A. A. Ayon, J. Protz, R. Khanna, X. Zhang and A. Epstein, "Application of Deep Silicon Etching and Wafer Bonding in the MicroManufacturing of Turbochargers and Micro-Air-Vehicles," 47th International Symposium of the American Vacuum Society, Boston, MA, October, 2000.

[67] X. Zhang, K.-S. Chen, R. Ghodssi, A. A. Ayón and S. M. Spearing, "Residual Stress Characterization of Thick PECVD TEOS Film for Power MEMS Applications," presented at 2000 Solid State Sensors and Actuator Workshop, Hilton Head, SC, June 2000.

[68] T. Harrison, MS Thesis, MIT, Department of Aeronautics and Astronautics, 2000.

[69] A. Mehra, X. Zhang, A. A. Ayon, I. A. Waitz and M. A. Schmidt, "A Through-Wafer Electrical Interconnect for Multi-Level MEMS Sevices," submitted to the *Journal of Vaccum Science and Technology.*

[70] E. Huang, "Thermal Design Trade Studies for A Silicon Turbojet Engine", MIT GTL Initial Report, October 1998.

[71] W-J Ye, Personal Communication, MIT GTL, 1999.

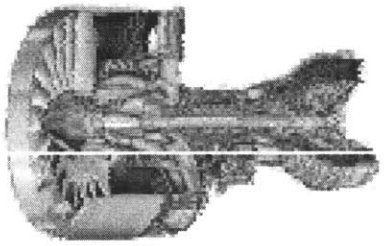

	Conventional Gas Turbine	Micro Engine (Potential)
Thrust	80,000 lbs.	20 grams
Weight	10:1	5:1
Part Count	10,000	2
Diameter	112 in.	1/2 in.

	(Potential)	($LiSO_2$)
Power	50 W	50 W
Energy	175 W-hr	175 W-hr
Weight	50 g	1000 g
Volume	60 cc	880 cc
Energy/Weight	3500 W-hr/kg	175 W-hr/kg

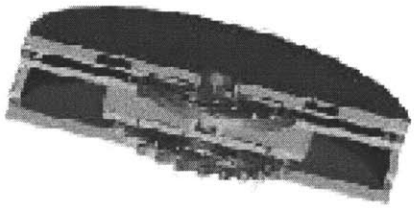

Figures courtesy D. Park

Figure 1-1: Illustration of microengine concept.

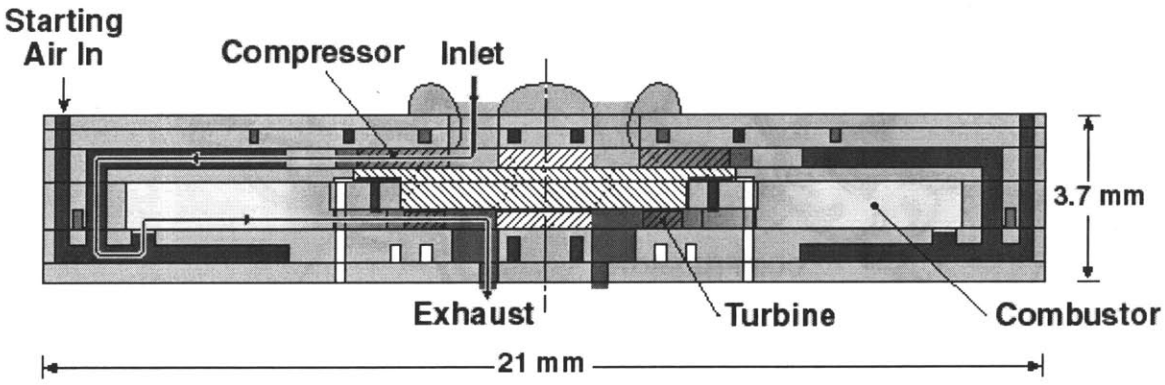

Figure 1-2: Cross-sectional illustration of demo engine showing flow path.

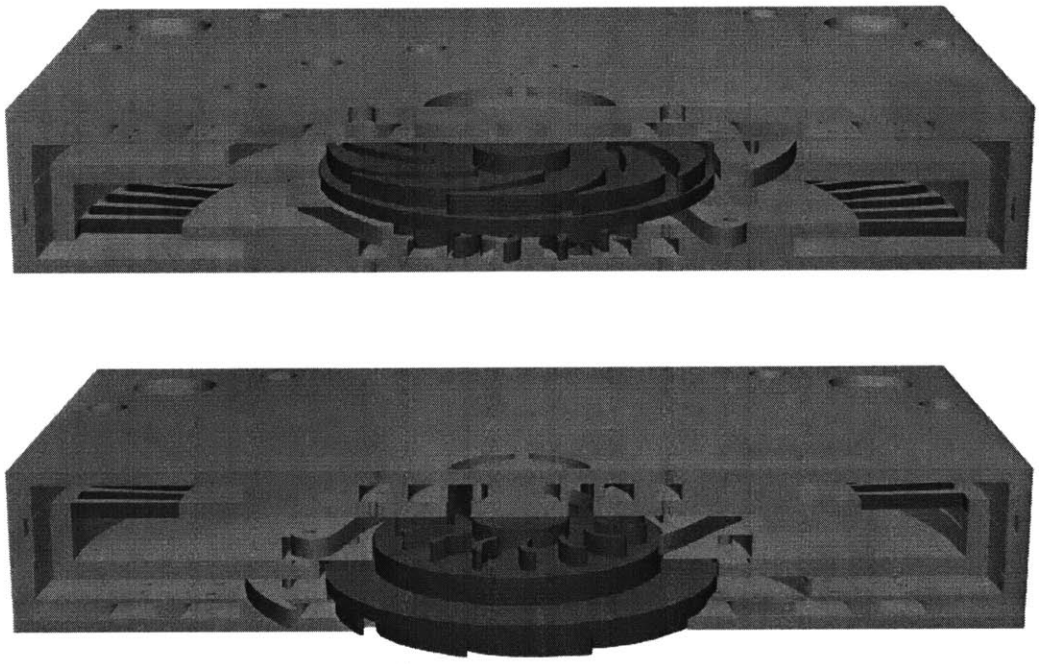

Figure 1-3: Three-dimensional illustration of demo engine cross section.

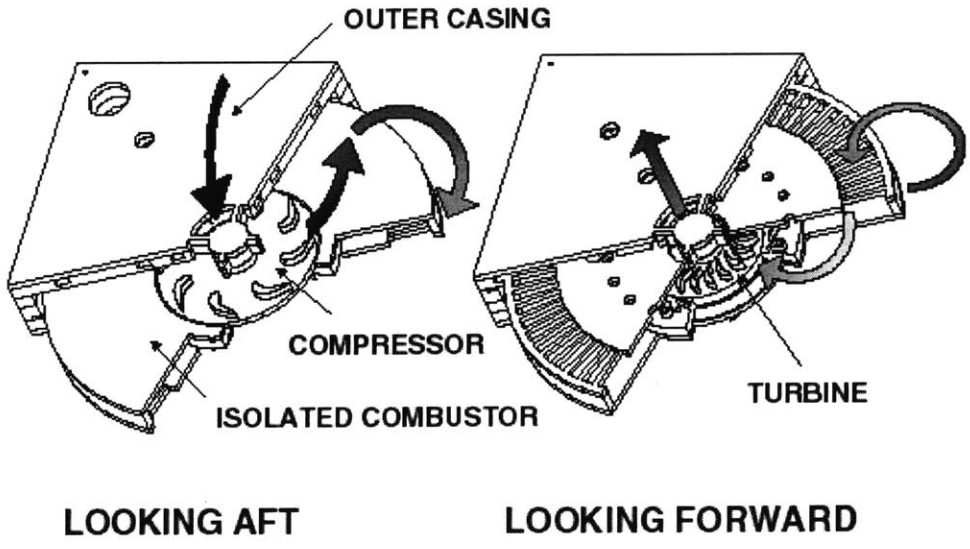

Figure 1-4: Three-dimensional illustration of demo engine cross section.

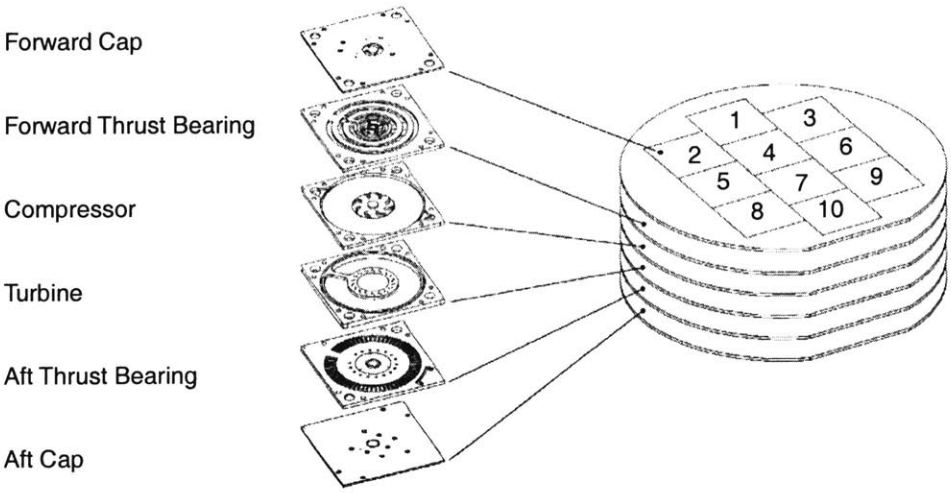

Figure 1-5: Illustration of demo engine fabrication concept.

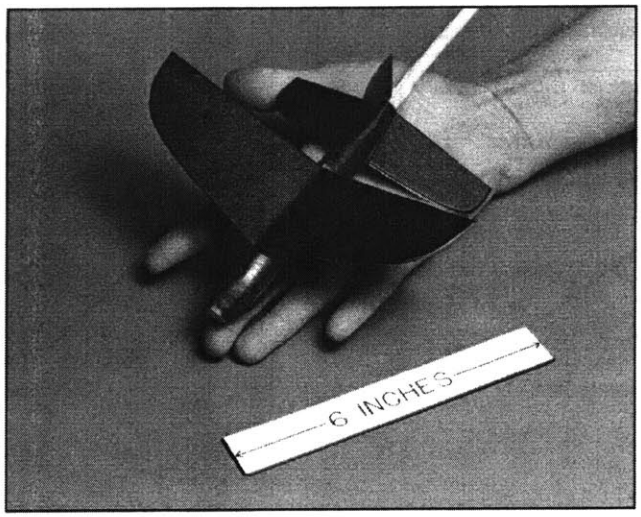

Image courtesy M Drela

Figure 1-6: Photograph of MIT jet-propelled micro air vehicle mock-up.

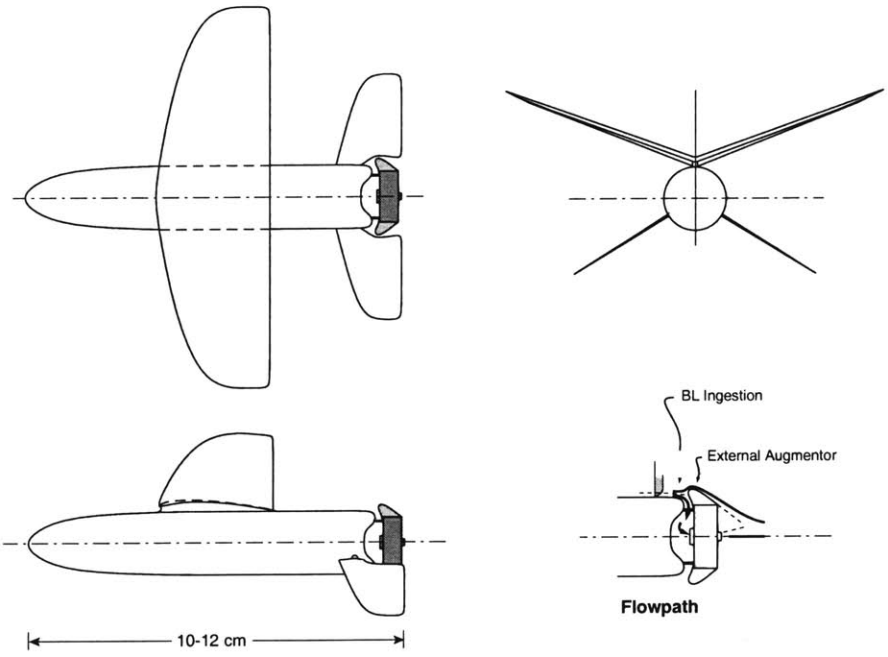

Image courtesy M Drela

Figure 1-7: Three-view drawing of MIT jet propelled micro air vehicle.

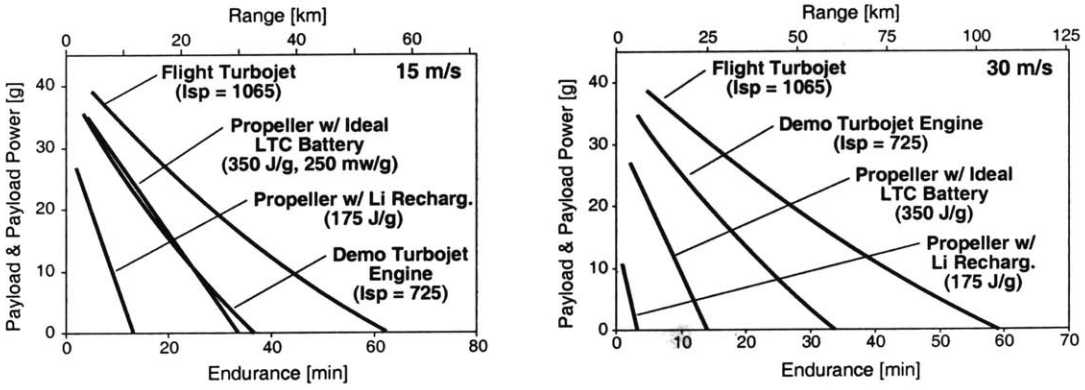

Figure 1-8: Comparison of electric and jet micro air vehicles.

CHAPTER 2

SYSTEM DESIGN

This chapter describes the overall system-level design of the demo micro engine, including definition of the functional requirements, cycle analysis, layout and preliminary design, and key trades. The primary goal of this chapter is to identify the fundamental engineering issues associated with the systems integration of a micro gas turbine engine by identifying and quantifying the critical tradeoffs encountered during design. The secondary goals of this chapter are to describe the global layout of the demo micro engine and to document the reasoning process behind the design.

This chapter presumes a fundamental knowledge of gas turbine engines and of MEMS technology. References [1,2,3] provide additional background on thermodynamics and gas turbine engine design. Reference [4] provides background on MEMS technology.

2.1 INTRODUCTION

As described in Chapter 1, Introduction, the demo engine is a 2.1cm x 2.1 cm x 3.77 mm turbojet engine manufactured from single-crystal silicon using MEMS microfabrication techniques. The engine is designed for an air flow of 0.36 grams/sec and a hydrogen fuel burn of 16 g/hr, giving a thrust of 10 grams. The predicted thermal efficiency is 2%. As illustrated in Figure 2-1, the engine consists of three primary subsystems: high speed rotating turbomachinery, a combustor, and a gas-bearing system.

The turbomachinery is on a single, shaft-less rotor at the core of the engine. It is surrounded by an annular combustor and static structure. Gas bearings separate the rotor from the static structure. The advantages of the shaft-less arrangement are ease of fabrication versus a shafted design and a reduced wafer count. The disadvantage is a larger overall engine diameter due to the 'flat' combustor shape. As described below, the shaft-less design also plays a key role in the demo engine's turbine cooling scheme.

The demo engine rotor has no shaft and the turbine and compressor disks are bonded directly to each other. The compressor diameter is 8 mm. The turbine radius is 6 mm. Design blade height for both the turbine and the compressor is 400 um. As described in Chapter 4, Fabrication, the fabricated devices had 225 um tall (span) blades. Tip clearances are 20 um for both turbine and compressor. The spool is designed to rotate at a speed of 1.2 million RPM giving a compressor tip speed of 500 m/sec and a turbine tip speed of 375 m/sec. At this design speed, the compressor should produce an adiabatic pressure ratio of approximately 3.0. Turbine cooling is accomplished by conducting heat from the turbine structure into the compressor flow through the spool. The heating reduces the compressor pressure ratio. The turbine is smaller than the compressor to minimize heat transfer into the turbine. The spool is designed for a structural temperature of 950 K, a heat transfer of 50W, and a consequent compressor pressure ratio of 1.80.

The rotor is supported by a hydrostatic gas bearing system. The baseline design calls for internal pressurization. However, as currently fabricated, the bearings are externally pressurized. A 15 um wide gap at the outer edge of the turbine disk serves as the journal bearing for the engine. This gap is pressurized from a plenum that sits between the turbine static structure and the portion of the compressor disk that extends beyond the turbine. The forward and aft thrust bearings are formed from gaps that sit above 2 mm diameter hubs at the center of the rotor. Each bearing consists of a 3.5 um tall gap pressurized by twenty 11 um diameter, 100 um deep restrictor nozzles located at a radius of 0.75 mm.

An annular combustor surrounds the turbine. The hot section of the combustor is thermally isolated from the rest of the static structure by a 'cooling jacket' that wraps around from the compressor discharge to the backside of the combustor. This reduces heat loss to the outside environment and reduces the exterior temperature of the engine. The flow enters the combustor from the bottom through an array of rectangular inlet ports that hold the flame. Fuel is injected

into the flow through a circular array of injectors just downstream of the compressor. The engine is started by an external air supply that injects flow directly into the combustor.

The demo engine is a MEMS device that is built by bonding together individually patterned silicon wafers to form a final multi-level stack. Figure 2-2 illustrates the wafer-stacking concept. Each wafer in the stack represents a 'level' of the engine structure. Each level has one or more major engine components. The individual components are formed by etching the silicon to extrude two-dimensional geometries into prismatic three-dimensional structures. The details of etching are covered in Chapter 4, Fabrication.

The remainder of this chapter describes the system design of the demo engine in more detail.

2.2 FUNCTIONAL REQUIREMENTS AND CONSTRAINTS

Like the design of any machine, the design of a microengine is an open-ended problem representing an intricate trade-off between many conflicting constraints. Any number of designs may result in an operational system that satisfies all of the constraints while still meeting the functional requirements. The demo engine design was driven by the functional requirements and by the constraints imposed by programmatic need, those imposed by the physics of the device, and those imposed by manufacturing capabilities. The following sections describe these requirements and constraints.

2.2.1 FUNCTIONAL REQUIREMENTS

At the time of design, there were no imposed external functional requirements for the MIT demo engine or its descendents. There were no specific applications and, hence, no specific requirements for thrust, power output, size, or weight. *The principle functional requirement of the demo engine is to demonstrate integration of the microengine component technologies into a complete system.*

Although integration is the only functional requirement of the demo engine, descendent engines should demonstrate a level of performance that plainly exceeds the performance of other compact

sources of power such as batteries and fuel cells. Toward these ends, the following set of general design goals were used for the demo engine:

(1) A design thrust of approximately 10g (equivalent to 10-20 watts of mechanical power).

(2) An engine life of tens of minutes or longer.

(3) A design with a minimum number of unproven process steps.

(4) Design for future growth potential:

- Addition of an electrical generator (electrical power output)
- Hydrocarbon combustion (liquid fuels)
- Recuperation (improved thermal efficiency)

Given the considerable uncertainty associated with individual component performance, the engine was designed to produce as much power as feasible. This led to an engine that was as large as possible while still being deemed to satisfy the constraints of microfabrication. A larger engine leads to a higher mass flow through the engine and more efficient turbomachinery (higher Reynold's number). Both factors lead to higher power output.

2.2.2 PROGRAMMATIC FACTORS

The design of the demo engine is driven in many ways by the needs and constraints of the overall MIT microengine program. Many of the concepts and technologies that were part of the overall program were developed with a demonstration engine in mind. An initial engine concept led to a number of simpler 'test bed' devices that were built to demonstrate critical technologies. Lessons from completed devices were incorporated into the demo engine design.

The demo engine development was strongly influenced by the fact that much of the fundamental microengine research occurred concurrently with the demo engine design. Scheduling constraints place a high premium on evolving the engine out of existing, proven technology as much as possible rather than relying on the development of new and untested ideas. Resource constraints limit the number of design ideas that can be analyzed and implemented. In many cases, the demo engine is designed around what is practically feasible or even proven rather than what is theoretically optimal. This is why, for example, the demo engine uses a "plain" circular journal

bearing and an integral combustor. At the time of design, both concepts had already been used for other microengine development devices [5, 6, 7]. The following concepts used in the demo engine design were chosen for programmatic reasons:

(1) Gas bearings. Gas bearings are an outgrowth of MIT's micro bearing rig.

(2) Integral Combustor. An integral combustor is an outgrowth of MIT's micro combustor.

(3) All-silicon construction. Currently, MIT can only fabricate with silicon.

(4) Single stage, single spool turbomachinery. This simplifies the device.

(5) Hydrogen fuel. Hydrogen has the broadest flammability margins.

(6) A simple Brayton thermodynamic cycle. This simplifies the device.

2.2.3 PHYSICAL CONSTRAINTS

The design is also constrained by the physics of the chemical, mechanical, and fluid-dynamic processes inherent in a gas turbine engine. The fundamental physical mechanisms that constrain the design are described here.

Combustor chemical reactions

The chemical processes within the combustor occur over a finite time period. If these reactions are to be constrained to occur within the combustion chamber, they must go to completion within the residence time of the flow in the combustor. This residence time is proportional to the combustor volume and inversely proportional to the engine volumetric flow rate. Thus, there is a minimum combustor volume that is set by the engine volumetric flow rate and the residence time required for the fuel-air reaction to complete. Increasing the pressure of the air increases the density and, therefore, increases the residence time for a fixed volume. Increasing the reaction temperature decreases the density but accelerates the reaction rate. Mehra demonstrated complete hydrogen and hydrocarbon combustion with residence times of 0.5 msec and 1.5 msec respectively [7].

Bearing stability

The engine's spool has a design speed of 1.2 million RPM. Unless the rotor can be accelerated quickly through unstable operating regions, the journal bearing must allow stable operation of the

bearing over the complete speed range from startup to design speed. The physics of the journal bearing design set a requirement on its geometry. This includes the length of the journal bearing, the width of the journal bearing gap, and the allowed taper and bow of the journal bearing. Because profile control is one of the most difficult aspects of microfabrication, the interaction of the journal bearing's physical constraints and its fabrication constraints has a significant impact on the overall engine design.

Turbomachinery performance

The compressor and turbine must have sufficient massflow, pressure ratio, and efficiency to close the engine's thermodynamic cycle and deliver the required thrust. The success of the combustor is also closely tied to the success of the compressor. For a fixed residence time, the required combustor volume is inversely proportional to the flow density. The overall efficiency of the cycle benefits from increases in efficiency. As shown in later chapters, a practical engine requires turbomachinery efficiencies in excess of 50%. This requirement has implications for the blade design, blade height, compressor dimensions, and spool rotating speed.

Structural integrity

The allowed component stresses and temperatures are limited by material properties. These requirements influence the rotor speed (hence pressure ratio), combustion temperature (hence specific thrust), and blade height (hence massflow). In order to get the maximum performance out of the engine, the structure is designed to operate near its stress and temperature limits (500-1000 MPa and 900-1000K for silicon). The high-temperature material properties of silicon make cooling necessary and place a substantial constraint on the design of the compressor and turbine [8]. Analyses by Chen, Ye, and Huang show that for the demo engine geometry, peak rotor stresses do not exceed 500 MPa. An all-silicon engine designed for these stresses must operate with a rotating structure temperature of less than 950 K [8]. The static structure is designed for a structural temperature of less than 1200 K and a peak stress below 100 MPa.

2.2.4 MANUFACTURING CONSTRAINTS

The design of the engine is also highly constrained by the capabilities of microfabrication. The currently available state-of-the-art in MEMS microfabrication imposes the following constraints on the design:

Two-dimensional features

MEMS microfabrication is essentially a 'planar' process: all three-dimensional features are formed by assembling two-dimensional shapes. In general, the two-dimensional shape of a feature is only constrained by the capabilities of the mask production company. However, these shapes can only be etched to create right-prismatic 3D shapes. It is possible to introduce limited three-dimensional geometry by using multiple nested etches to create steps. It is also possible to introduce limited fillets at the base of features. However, slanted cuts or compound three-dimensional shapes are generally not currently possible.

Minimum feature size

The minimum feature size on the engine is limited by the ability to fabricate that feature. Mask production and photolithography limit the minimum hole size of restrictors for thrust bearings, tabs for rotor retention, and blade trailing edge thickness, cooling holes, etc. Variations in etcher performance set the minimum allowable wall thickness, retention tab size, and journal bearing width. As a rule, the smallest achievable features were 10 um with aspect ratios between 30:1 and 50:1. For bonded features, 50 um is a practical minimum wall thickness. Details on feature size can be found in [9].

Maximum feature size

The maximum thickness of a single wafer in the engine is limited by the ability to process that wafer. In general, at MIT, the thickest wafers for practical use were 1 mm thick. The restriction on wafer thickness can limit the blade height, journal bearing depth, and combustor height. The maximum size of a die is limited by the desire to fit a reasonable number of die on a single wafer. A four inch wafer as used at MIT can hold a maximum of 10 die with a die size of 2.1 cm. Growing the die beyond 2.1 cm cuts the die count to 4 or less. The maximum size is also tied to

the minimum dimension through mask definition. The standard die size for large microchips is 2.0 cm.

Wafer Alignment

The demo engine is built from several layers, each having features on both sides. These layers are bonded together. The front-to-back alignment of features etched on each side of a wafer and the wafer-to-wafer alignment are both important for imbalance of the rotor. Alignment is also important for tolerancing the widths of features that must be bonded together. Alignment is considered in detail with bearing design in Chapter 3.

Packaging

The number of fluidic and electrical ports is limited by the ability to connect these ports to the outside world. Fluidic connections are made with o-rings (cold package) or glass-brazed tubes (hot package). The minimum connection size is set by the availability of tubes, o-rings, and glass beads used to make these connections. For both o-rings and glass braze connections, a practical connection spacing is 2 mm. Packaging also constrains the device outer wall temperature. The glass braze connections have a practical maximum temperature of 1000-1200 K.

Mask fabrication technology

Mask fabrication technology set the minimum feature size, the maximum die size, and the ratio of die size to feature size. Using conventional stepper mask generators, a mask that requires very precisely defined fine (~1 um) features cannot also have very large features. For example, the demo engine requires 4 um features and therefore cannot be much larger than 2 cm. More expensive e-beam masks can deliver sub-micron features with no limit on die size.

2.2.5 Testing Requirements

The demo engine design is also constrained by the need to instrument the device for testing. Testing requirements set the type and number of required fluidic and electrical interconnects, the type of packaging scheme, the allowable device operating temperature, and aspects of the device geometry. A production engine would only need a few connections to the outside world: start air, electrical input/output, and fuel connections. The demo engine must be instrumented to take

performance measurements that allow us to understand the engine behavior. It consequently requires a number of additional ports including: impeller discharge pressure, compressor discharge pressure or pressure ratio (OPR), turbine inter-row pressure, nozzle pressure or engine pressure ratio (EPR), side pressurization pressure, journal bearing pressure, thrust bearing pressure, etc. This instrumentation introduces an additional level of complexity to the device.

2.3 LAYOUT

A number of preliminary layout concepts were considered before drawing the complete demo engine mask set. These preliminary layouts set the basic cross-sectional geometry of the engine. Each layout met all of the functional requirements and general constraints listed above while having one or more particular advantages. Each preliminary layout also included an associated "strawman" fabrication process. As the design progressed, a number of new concepts were introduced that either simplified manufacturing or improved engine performance. Often these were conflicting goals.

Evolutionary modifications of these preliminary layouts led to the baseline demo engine design. This baseline demo engine layout formed the basis for all parametric studies of engine performance. It also was used for detailed component design. The baseline design could not be fabricated in the time available, so a number of design simplifications were introduced part way through the fabrication development effort. This led to a set of fabricated devices that differ from the baseline design. The fabricated devices are the 'hot static structure' described in [7], a turbocharger, and a fabricated demo engine (as opposed to the 'baseline' demo engine). Figure 2-3 illustrates the device evolution.

2.3.1 BASELINE DEMO ENGINE

Figure 2-1 illustrates the final layout chosen for the MIT baseline demo engine. The design grew out of the MIT experience with other microengine-related rigs and out of the general constraints listed above. The baseline demo engine is built from six wafers. One wafer is used for the compressor. A second is used for the turbine. Two wafers each were used for the forward and aft

thrust bearings. The combustor is made up of a combination of the rotor and aft thrust bearing wafers.

The demo engine design introduced a number of significant changes from MIT's originally proposed design [10]. It eliminated the electrical machinery (electrical power is not a functional requirement for the demo engine), replaced the baseline engine bearing system with the side-loaded plain circular journal bearing and hydrostatic thrust bearings used on the MIT micro-bearing rig [5], and incorporated a thrust balancing system to balance the pressure forces on the rotor.

The demo engine design is also larger than MIT's original microengine design. The demo engine was designed for a nominal core flow of 0.36 g/sec of air at a pressure ratio of 3:1 and a turbine inlet temperature of 1600K. Subsequent analysis showed that demo engine's cooling scheme would drive the compressor pressure ratio down to 1.8. The compressor impeller radius was doubled to 4 mm and the blade height doubled to 400 um. The tip speed was held at 500 m/sec giving a rotor speed of 1.2 million RPM.

The demo engine uses a two-wafer rotor spool formed by bonding the compressor disk directly to the turbine disk. This eliminates the wafers used for the shaft in earlier designs. The journal bearing is located on the turbine disk. The turbine and compressor disks are sized differently, reducing turbine stress for a given compressor speed and regulating the amount of heat transferred between the turbine and compressor. This also increases the bearing L/D and provides space for a thrust balancing piston and an optional journal bearing side-load scheme.

The demo engine first introduced the concept of a thermally insulated combustor to lower the device outer wall temperatures while still allowing high combustor exit temperatures. Preliminary analysis showed that this new combustor could operate with an exit temperature of 1600K, a combustor wall temperature of 1200K, and an outer wall temperature of 850K. As initially proposed, the insulated combustor was to use a layer of glass to isolate the combustor from the outer structure. The desired high-temperature glass was not readily available. Thermal analysis later showed the glass desirable but not necessary and the design was changed to use Si.

Rather than using an electrical motor for startup, the demo engine relies on externally supplied start air. To introduce this supply air, the design includes provisions for external fluidic connections borrowed from MIT's micro rocket program [11]. These fluidic connections are also used for pressure taps, fuel supply lines, and starter air lines.

Finally, the new design took advantage of a new turbine cooling scheme initially studied by Chen [8] to allow all-silicon construction. This scheme is described in more detail below, but it basically involves dumping excess heat from the turbine blades and disk into the compressor core flow by conducting the heat through the spool's shaft and into the compressor structure. The scheme works because silicon has a comparatively high thermal conductivity and the device has comparatively small dimensions, allowing a low thermal impedance between the two structures.

2.3.2 FABRICATED DEVICES

The baseline demo engine design incorporates a number of undeveloped technologies. To simplify development of these technologies, the demo engine was preceded by two simpler micro-rigs to be developed in parallel: (1) the hot rig and (2) the turbocharger rig. These rigs have two goals. The first is to demonstrate operation of key engine components without requiring operation of a complete engine. The second is to develop the fabrication technologies required for a complete demo engine. Both rigs are similar in layout to the baseline demo engine, but are somewhat easier to fabricate.

Hot Static Structure

The hot static structure, or "hot rig," has the same flow path geometry as the baseline demo engine, but does not have rotating turbomachinery. The purpose of the hot rig is to verify combustor performance (pressure drop, combustor efficiency, chemical efficiency, turbine inlet temperature), evaluate fuel injector performance, test alternate fuels, and validate structural integrity at operating temperatures. The hot rig was developed and tested by Mehra [7]. Continued tests of a hydrocarbon combustor are being carried out by Cadou and Spadaccini. Figure 2-4 illustrates a schematic drawing and SEM of the cross-section of the hot static structure.

Mehra's results show that the demo engine combustor geometry burning hydrogen can deliver a turbine exit temperature of 1600K and a peak combustor efficiency of 0.95. Due to geometric

complications unique to the hot rig, tests were not conducted at the specific baseline engine design conditions. However, it did demonstrate operation at the dynamically scaled equivalent of the on-design condition. For further details on the hot rig, consult the references listed in chapter 1, Introduction.

Turbocharger

The turbocharger has the same morphology as the baseline demo engine, but has separated compressor and turbine gas paths. The purpose of the turbocharger is to verify bearing and turbomachinery operation. In addition, the turbocharger should allow more accurate measurement of the component performance parameters than is possible with an operational combustor or a complete cycle.

The turbocharger morphology is identical to the demo engine morphology except for the removal of the "cooling jacket" that links the compressor exhaust to the combustor inlet. The compressor, turbine, and combustor are retained and are geometrically similar to the demo engine. In order to expedite fabrication, certain aspects of baseline demo engine design were modified for the turbocharger. As of this writing, the current "state-of-the-art" microfabrication techniques do not support a 500 um journal bearing etch or the 700-900 um wafers required for 400 um blades. The reasons are explained in detail in Chapter 4, Fabrication. As a result, the turbocharger was modified to have a 300 um journal bearing and 200 um blades. The side-pressurization scheme and the compressor "rim seal" were also eliminated to ease fabrication and to address a structural concern associated with compressor disk deflection at high speeds.

Fabricated Demo Engine Layout

Although all subsequent system and component analysis used it as the "baseline," the complete demo engine layout could not be fabricated. As mentioned above, at the time of turbocharger fabrication, MIT's fabrication techniques did not support 500 um journal bearings or 400 um blades. Initially, efforts were under way do develop these capabilities in parallel with the turbocharger and to then implement them in the demo engine. Neither capability was developed in time. As a result, the first demo engine was given the same 300 um journal bearing and 200 um blades used in the turbocharger.

Compared to the hot rig and the baseline demo engine designs, the geometry of the as-fabricated turbocharger and first build demo engine cuts the engine flow area and combustor volume in half. CFD calculations indicate reduced compressor efficiency associated with the shorter compressor blades. Elimination of the seals increases compressor leakage. Table 2-3 quantifies the cumulative impact of these changes on the predicted cycle performance. Although the CFD compressor efficiency predictions are uncertain (estimate +/- 10 points in comparison to scaled macro compressor rig experiments), the calculation suggests that the as-modified first build of the demo engine has an open cycle and will require air injection for sustained operation.

2.4 CYCLE ANALYSIS

This section describes the fundamental systems level trade studies conducted for the demo micro engine. These include parametric cycle analyses, consideration of alternative cycles, and mechanical design trade studies. The goals of this section are to identify the sensitivity of the engine performance to important parameters, to illustrate the considerations that drove the demo engine design, and to suggest improvements to future designs.

2.4.1 FUNDAMENTALS

Once the functional requirements of the demo engine were set, the design started with a cycle analysis. A cycle analysis is a general tool to model engine behavior without detailed knowledge of the mechanical geometry. For a comprehensive overview of gas turbine cycle analysis, consult references [1] and [3]. For a more general analysis of micro engine gas turbine cycles, consult [12].

Gas turbine engines are heat engines. Like all heat engines, they work by converting the thermal energy released from a burning fuel into useful mechanical energy. This mechanical energy can appear as work supplied to a spinning shaft (a turboshaft engine) or as velocity imparted to an exhaust jet (a turbojet engine). In either case, the energy conversion process can be modeled using a thermodynamic cycle that involves the compression, heating, and expansion of a working fluid. In the case of a jet engine, the working fluid is air. The overall performance of any jet engine can be predicted with reasonable accuracy using a thermodynamic analysis of this cycle.

The thermodynamic cycle for a simple gas turbine engine is known as the Brayton cycle. The ideal Brayton cycle, illustrated in Figure 2-6, involves the following steps:

(1) Isentropic (reversible, adiabatic) compression of the working fluid.

(2) Constant pressure heat addition.

(3) Isentropic expansion of the heated working fluid.

(4) Constant pressure heat rejection.

Jet engines are open-cycle machines. Consequently, the fourth step, constant-pressure heat rejection, occurs when the engine exhaust mixes with the surrounding atmosphere. As Figure 2-7 illustrates, the engine components that achieve each steps are (1) Compressor, (2) Combustor, (3) Turbine (drives compressor) and exhaust nozzle. When the engine is operated as a turboshaft, a fourth component, (4) the electrical generator, converts the mechanical power of the rotating turbine into electrical power.

2.4.2 IDEAL CYCLE ANALYSIS

The ideal Brayton cycle is an important starting point for understanding the role of two key cycle parameters: (1) Turbine Inlet Temperature, Tt4 and (2) Overall Pressure Ratio, π_c. Together, these two cycle parameters set the power output (or thrust) and efficiency of an ideal gas turbine engine [3].

The power output of a Brayton cycle is proportional to the area it encloses on a temperature-entropy (T-s) diagram[2]. This area is set by a combination of the pressure ratio and the peak cycle temperature, Tt4. For any given pressure ratio, increasing Tt4 will always increase the engine power output. This is illustrated in Figure 2-9. On the other hand, for any fixed Tt4 there will always be a specific pressure ratio that maximizes power output. For pressure ratios above or below this value, the area of the cycle shrinks and the power output is reduced.

---

[2] For an explanation of T-s diagrams, consult [2] or any fundamental thermodynamics textbook.

The thermal efficiency (η_{therm}) of a cycle is the ratio of the output mechanical energy to the input fuel energy. The thermal efficiency of the ideal Brayton cycle is determined directly from the overall pressure ratio as follows:

For an ideal cycle, a large pressure ratio means a high thermal efficiency. High pressure ratio is

$$\eta_{therm} = 1 - \frac{T_2}{T_3} = 1 - 1/\pi_c^{(\gamma-1)/\gamma}$$

the traditional way to achieve high efficiency in an aircraft engine. Modern commercial aircraft engines have pressure ratios as high as 45 [1].

For an ideal simple Brayton cycle, there is always a conflict between higher thermal efficiency (maximize pressure ratio) and higher thrust or power output (specific, finite pressure ratio). Figure 2-8 illustrates this. Of course, a larger Tt4 implies a higher pressure ratio for maximum power output. This, in turn, implies a higher thermal efficiency for the maximum output cycle. Therefore, increases in Tt4 are always beneficial. As shown below, these observations are generally true for non-ideal Brayton cycles as well.

2.4.3 NON-IDEAL CYCLE ANALYSIS

The power output of the Brayton cycle is given by the small difference between two large numbers (turbine work output and compressor work input). Consequently, gas turbines are exceedingly sensitive to component inefficiencies. An accurate prediction of engine performance requires that non-ideal component behavior be accounted for.

The ideal Brayton cycle can never be achieved in practice because there is always some non-reversible behavior associated with the components. The most important non-idealities are:

(1) Imperfect diffusion in the engine inlet

(2) Pressure loss mechanisms (e.g. friction, shocks, mixing) in the compressor and turbine.

(3) Heat loss, incomplete combustion, and pressure losses in the combustor

(4) Imperfect expansion in the exhaust nozzle

(5) Bleed from the compressor discharge air for bearings, cooling, and auxiliary uses

(6) Temperature-related variations in working fluid properties (c_p, c_v, etc.)

(7) Non-adiabatic compression and expansion

Figure 2-11 illustrates the impact each non-ideality has on the overall engine cycle. The first six non-ideal behaviors are noted in Kerrebrock [1] and are common to all gas turbines. The seventh behavior, non-adiabatic compression, is not usually a concern for conventional engines operating on-design. However, as discussed later, it is very important for the demo micro engine. Non-ideal cycle analysis accounts for non-ideal component behavior by including the following component efficiencies and performance parameters:

Turbomachinery Efficiencies

The isentropic efficiency of a non-ideal compressor (η_c) operating at a specific mass flow and total-total pressure ratio is defined as the inverse of the ratio of actual input shaft power to the power required for an ideal isentropic compression process of the same total-total pressure ratio:

$$\eta_c = \frac{IsentropicPower}{ActualPower} = \frac{T_{t2}(\pi_c^{(\gamma-1)/\gamma} - 1)}{w} = \frac{T_{t2}(\pi_c^{(\gamma-1)/\gamma} - 1)}{c_p \Delta T - q}$$

The isentropic efficiency of a non-ideal turbine (η_t) operating at a specific mass flow and total-total pressure ratio is defined as the ratio of actual delivered shaft power to the power delivered by an ideal isentropic expansion process of the same total-total pressure ratio. Symbolically,

$$\eta_t = \frac{ActualPower}{IsentropicPower} = \frac{w}{T_{t4}(1 - \pi_t^{(\gamma-1)/\gamma})} = \frac{c_p \Delta T - q}{T_{t4}(1 - \pi_t^{(\gamma-1)/\gamma})}$$

Combustor Performance

The overall combust*or* efficiency of a non-ideal combustor is defined as the ratio of the heat delivered to the combustor flow to the total stored energy of the fuel delivered to the combustor.

$$\eta_{combustor} = \frac{\dot{m} \cdot c_p (T_{t4} - T_{t3})}{\dot{m}_f \cdot h_f}$$

The combust*ion* efficiency of a non-ideal combustion process is defined as the fraction of the total fuel that is completely burned within the combustor. For the purposes of cycle analysis, the combustion efficiency can be grouped into the combustor efficiency.

The combustor also has a pressure drop due to viscous losses in the flow path and heat addition to a moving flow. The combustor pressure ratio, π_b, is the ratio of the total pressures at the inlet and exit of the combustor.

Bleed

Bleed air is air that leaves the engine core flow for some portion of the cycle. In a single spool gas turbine engine such as the demo engine, there are three principle types of bleed: (1) overboard bleed, (2) NGV discharge bleed, and (3) turbine discharge bleed. Because cycle performance is affected by ratios, all of these bleeds are measured as a fraction of the core mass flow.

Figure 2-10 illustrates the bleeds for a single-spool turbojet. Overboard bleed is air that is removed completely from the cycle. NGV-discharge bleed air rejoins the core flow after the turbine nozzle guide vanes (NGV), but before the turbine rotor. This fluid still does work for the cycle because it flows through the turbine. However, it does less effective work than the core because it does not go through the combustor and, therefore, has a lower enthalpy. Turbine-discharge bleed air rejoins the core flow in the turbine rotor, before the exhaust nozzle. This fluid does little work in the turbine because it is introduced partway through or completely downstream. However, it does contribute to the engine thrust because it increases the nozzle mass flow. Again, this air typically has a lower enthalpy than the core flow. Air that is used to cool the turbine structure is turbine-discharge bleed.

Non-Ideal Cycle Analysis Procedure

Once component performance and efficiencies are known, the overall performance and parameters of a non-ideal cycle can be calculated by balancing the power output of the turbine with the power input required by the compressor. Chapter 3 of reference [1] gives a detailed description of this procedure.

For the demo engine design, the non-ideal cycle analysis was calculated using two tools. The first tool is GASTURB ™, a commercial "cycle deck" for non-ideal gas turbine engine analysis. GASTURB accounts for all component inefficiencies. In addition, it uses temperature and chemistry-dependent look-up tables for fluid properties. GASTURB allows parametric cycle studies and cycle optimizations and was used for all parametric cycle studies described here. Groshenry modified GASTURB for hydrogen combustion and verified it against NPAS, a NASA cycle deck [12]. For additional details on GASTURB, consult references [12] and [13].

Non-ideal cycle analysis was also performed using a custom Microsoft Excel spreadsheet detailed in the appendices. For simplicity, the spreadsheet uses fixed fluid properties for compressor and turbine calculations. All calculations assumed a $\gamma = 1.4$ and $c_p = 1004.5$ J/kg-K in the compressor and $\gamma = 1.28$ and $c_p = 1320$ J/kg-K in the turbine. The former are values for air at standard temperature and pressure [1]. The latter are values from CEA, a chemical equilibrium analysis program, for a hydrogen/air mixture with complete combustion at a temperature of 1600K. Hydrogen calculations assumed a fuel heating value of 120 MJ/kg-K. Hydrocarbon calculations assumed a fuel heating value of 43.3 MJ/kg-K. The spreadsheet calculation also includes the ability to account for heat transfer from the turbine to the compressor. The calculations were benchmarked against the variable parameter calculations of GASTURB.

Table 2-1 compares the spreadsheet calculations to GASTURB for the baseline demo engine cycle and a higher-performance microengine cycle. The table shows less than 5% error for turbojet thrust, less than 5% error for hydrogen fuel consumption, and less than 10% error for thrust-specific fuel consumption (TSFC). The table also shows that modeling heat transfer changes the results by less than 10%. The spreadsheet cycle was used for all system trade studies because of its flexibility in comparison to GASTURB.

2.4.4 BASELINE CYCLE

A reference cycle for the demo engine was calculated using initial estimates for component performance and the non-ideal cycle analysis described above. The initial estimates were iterated until a cycle was found that met the functional requirements while remaining consistent with best estimates on achievable component performance levels. This reference cycle varied throughout the demo engine preliminary design phase as the engine layout changed and new information became available to predict turbomachinery, bearing, and combustor performance. During the summer of 1998, a final "baseline" cycle was chosen as the target cycle for the detailed design phase. This baseline cycle led to specified performance levels for each component.

Table 2-3 summarizes the baseline cycle calculated using the spreadsheet formulation. The analysis predicts an engine with a closed cycle operating with a turbine inlet temperature (Tt4) of 1600K, an overall compressor pressure ratio (OPR) of 1.8, and a core mass flow of 0.36 grams/sec. Isentropic compressor efficiency is 0.50, turbine isentropic efficiency is 0.70. Combustor pressure ratio is 0.98 and combustor efficiency is 0.99. Bearing power offtake (drag) is 13 W. The cycle assumes an overboard bleed of 5% to supply the gas bearings. The analysis predicts an engine thrust of 9 grams at a fuel burn of 16 g/hr of hydrogen. This gives a thrust-specific fuel consumption (TSFC) of 1.8 g/g-hr and a specific impulse of (Isp) of 2050 sec. If operated with a hydrocarbon fuel such as butane, propane, or kerosene, this engine would have a fuel burn of 43 g/hr and a TSFC of 4.9 g/g-hr (Isp of 740 sec). The overall thermal efficiency of the engine is 2%.

The baseline cycle assumes turbojet operation. If the engine is instead operated as a turboshaft engine for electrical power generation, it would have a shaft output power of 7.6 W and a power-specific fuel consumption (PSFC) of 2.0 g/W-hr. If a hydrocarbon fuel is used, the fuel burn will be 43 g/hr giving a PSFC of 5.6 g/W-hr. These numbers represent the mechanical efficiency of the turboshaft engine. If the engine produces electrical power, the mechanical power and efficiency must be multiplied by the generator efficiency (30%-50%).

2.4.5 CYCLE ANALYSIS TRADE STUDIES

The baseline cycle described in Chapter 2 is based on the best available estimates for individual engine component performance. Actual component performance may vary substantially, leading to variations in the overall cycle performance. In addition, because the design was evolutionary, some of the new lessons learned during development could not be incorporated into the baseline.

The GASTURB cycle analysis program was used to study the influence of component performance on the baseline demo engine cycle. Several parameters were considered including turbomachinery efficiency and pressure ratio, combustor performance, bearing drag, bleed, recuperation, etc. These parametric studies are described below. Throughout the remainder of this section, unless specified otherwise, the cycle parameters used are those of the pressure ratio 1.8 cycle given in Table 2-3.

Turbomachinery Performance

As shown in the preceding section, the Brayton cycle is very sensitive to pressure ratio. Turbomachinery performance is therefore very important. The following studies analyze the role of compressor performance and turbine performance.

The thermal efficiency of an ideal Brayton cycle (all components 100% efficient) increases continuously with increasing pressure ratio, while the power is maximized at a specific pressure ratio. For an ideal Brayton cycle in the demo engine Tt4 design range (1400-1800K), the maximum power pressure ratio is between 15 and 20. For a non-ideal cycle, this pressure is lower. The computational and experimental studies of micro turbomachines conducted to date show efficiencies in the range of 0.30 to 0.65 [14]. For this range of efficiencies, power is maximized at pressure ratios between 3 and 5.

Both the compressor and the turbine play an important role in the overall cycle efficiency. For a given pressure ratio, turbines are typically more efficient than compressors. This is due to the fact that turbines operate with a favorable pressure gradient while compressors operate with an adverse pressure gradient.[3] A favorable gradient encourages attached boundary layers, reducing

[3] In a favorable gradient, pressure decreases with the flow. In an adverse gradient, pressure increases with the flow.

viscous losses and blockage. Depending on the specifics of the cycle, one point of compressor efficiency may be more valuable or less valuable than one point of turbine efficiency. When the turbine is very efficient (e.g. 0.95) and the compressor is inefficient (e.g. 0.50), the compressor efficiency will be more important. The converse is also true.

Figure 2-12 illustrates cycle performance for the baseline demo engine running with moderate pressure ratios (2.0-6.0). The figure illustrates the impact of variations in both turbine and compressor performance. The cycle study shows that for efficiencies above 0.50, there is a +/- 50% variation in thrust as pressure ratio is varies from 2.0 to 5.0. By contrast, thrust nearly doubles as compressor efficiency moves from 0.50 to 0.65.

The results show that increasing compressor efficiency is the most effective tool for increasing engine performance. A 15-point gain in compressor efficiency can double thrust and cut TSFC by more than a factor of two. Achieving the same effect with the turbine would require a 20-point gain in turbine efficiency to 0.90.

The turbine and the compressor show similar changes in thrust with changes in efficiency. Note, however, that over the full range of pressure and efficiencies the fuel flow rate varies by only +/- 20%. By contrast, thrust varies by a factor of four. In the case of turbomachinery performance, changes in TSFC primarily reflect changes in thrust.

Low OPR Brayton Cycles

An engine can run with low compressor efficiency if it also has a low pressure ratio. Such an engine will have a very low thrust because nearly all of the power goes into driving the compressor. In such a situation, the compression process contributes little to the Tt4 so that fuel burn is comparatively independent (+/- 5%) of compressor performance. Thrust, meanwhile, is close to zero and can double or even triple with single-point changes in compressor efficiency or OPR. TSFC is the ratio of these two and is therefore extremely sensitive.

Figure 2-13 illustrates cycle performance for the baseline demo engine running with low pressure ratios (1.5-2.0) and compressor efficiencies between 0.40 and 0.65. Fuel burn is constant to within +/- 5% of the nominal design value. The thrust varies between 2 gf and 16 gf giving a TSFC range of 8.0-1.0 g/hr/g (Isp 450-3600 sec). For compressor efficiencies below 0.50, every

point of efficiency is worth approximately 1 gf of thrust. For efficiencies above 0.50, every point of efficiency is worth 0.2-0.3 gf of thrust. One point of pressure ratio is worth between 1 and 2 gf of thrust, depending on efficiency. Increasing pressure ratio is always beneficial *in this performance range.*

Hydrogen Combustor

The combustor can affect engine performance through two performance variables. A drop in combustor efficiency translates directly into an additional fuel burn with no increase in thrust. A drop in combustor pressure ratio shows up as a reduction in thrust with no change in fuel burn.

Figure 2-14 illustrates the effect of combustor pressure ratio and efficiency on the baseline demo engine cycle. The analysis shows a 3.6 gram drop in thrust and an increase of 1.0 g/g/hr TSFC for every half-point of combustor pressure ratio. Actual fuel burn remains unaffected. Fuel burn is proportional to combustor efficiency, showing an increase of 2.5 g/hr for every 10 point drop in efficiency. This corresponds to a 0.25 g/g-hr increase in TSFC. The thrust is insensitive to combustor efficiency, showing a loss of 1.5 g thrust over a 30 point drop in efficiency.

Hydrocarbon Combustion

The preceding parametric studies were for a hydrogen-fueled turbojet. Hydrogen was chosen as the initial fuel because it is the easiest fuel to burn in a small device. However, hydrogen is not a readily storable fuel. Hydrocarbon fuel such as butane, propane, acetylene, or kerosene can be stored as liquids and are preferable for portable power applications.

Switching to a hydrocarbon fuel impacts the cycle in two ways. First, hydrocarbons have a lower fuel heating value than hydrogen (approximately 43 MJ/kg versus 120 MJ/kg). This leads to approximately triple the fuel burn and a correspondingly lower TSFC. Secondly, the chemical products of the combustion reaction are different. This leads to a change in the fluid properties of the turbine core flow and a corresponding change to the overall cycle. Figure 2-15 compares GASTURB computations for hydrogen and kerosene burning turbojet engines. The calculation shows that the chemical kinetics have only a negligible effect (less than 1%) on the quantitative performance estimates and no effect on the qualitative results. Hydrocarbon-burning engine

performance estimates can be accurately extrapolated from hydrogen-based calculations by simply multiplying fuel burn, PSFC, TSFC, or 1/Isp by the inverse ratio of heating values (~3).

Compressor Bleed and Secondary Flows

All gas turbine engines involve some type of secondary flow system. In a conventional engine, the secondary flow system bleeds air from the compressor discharge to provide auxiliary high-pressure air for customer use and to use as a coolant for bearings, turbine blades, and turbine disks. In the demo microengine, bleed air from the compressor discharge is used to pressurize the gas bearing system. Alternately, this air can be supplied externally, creating a 'negative' bleed. Air also leaks through rotating seals that separate high-pressure and low-pressure portions of the engine. Finally, bleed air can be used as a coolant. Whatever the application, bleeding compressor air removes it from the cycle and, consequently, has an impact on the overall cycle performance.

As mentioned previously, there are three types of bleed: (1) overboard bleed, (2) NGV discharge bleed, and (3) turbine discharge bleed. In the demo engine, the forward thrust bearing supply air is overboard bleed. So are any leaks through the side-pressurization ports and the instrumentation ports. The journal bearing supply air is NGV-discharge bleed. The demo engine aft thrust bearing supply air is turbine-discharge bleed. If the demo engine had turbine film cooling, this air would also be turbine-discharge bleed.

Figure 2-17 illustrates the impact of bleed on the baseline demo engine cycle for a range of compressor pressure ratios. The figure shows the effects of both overboard bleed and NGV bleed. Depending on the re-injection point within the turbine, the performance with turbine-discharge bleed will be somewhere in between. For all bleeds, thrust and fuel consumption decrease as bleed increases. Thrust decreases because enthalpy and mass flow are lost. Fuel consumption decreases because with more bleed, less fuel is required to maintain the same fuel/air ratio and Tt4 in the combustion chamber. NGV bleed gives much better performance than overboard bleed, allowing double the bleed for a given level of thrust.

Based on the results described above, the demo engine shows approximately 3 grams of lost thrust for every 5 percentage points of overboard bleed and 1.5 grams of lost thrust for every 5 percentage points of NGV-discharge bleed. A 15% overboard bleed used to achieve a pressure

ratio of 4.0 leads to a thrust of 12.5 and a H2 fuel burn of 12.5 g/hr. This gives a TSFC of 1.0 g/hr/g (Isp 3600 sec), a 60% reduction from the baseline value of 1.6 g/hr/g.

Bearing Drag

The rotating turbomachinery in a gas turbine engine is supported by a set of bearings. Conventional engines use a variety of bearings including ball bearings, roller bearings, oil-film bearings. The demo engine uses gas bearings. Typically, the drag of these bearings scales with rotor speed squared. At the same time, pressure rise (hence, pressure ratio) also scales with speed squared. There is a trade-off between increased pressure ratio and increased bearing drag. Depending on the on-design drag of the bearings, increasing rotor speed may increase or decrease thrust.

Figure 2-16 illustrates the tradeoff between pressure ratio and bearing drag for the baseline demo engine cycle assuming a *fixed engine mass flow*. The cycle shows that there is a direct tradeoff between bearing drag and thrust. Every 5 Watts of bearing drag costs 2 grams of thrust. The compressor pressure ratio has little influence on the sensitivity of thrust to bearing drag.

The figure also shows the impact of increased rotor speed. Given a fixed spool geometry, increasing the spool speed 40% doubles the bearing drag. At the same time, the pressure rise doubles. If the engine initially has a pressure ratio of 2.0 and a bearing drag of 10 Watts, the pressure ratio will go to 3.0 and the drag will go to 20 Watts. Figure 2-16 shows that this leads to a 12% reduction in specific thrust and a 6% increase in TSFC. If, the initial drag were 5W doubling to 10W, there would be a 4% increase in specific thrust and a 6% decrease in TSFC.

We presumed fixed engine mass flow above. A more representative assumption is that compressor mass flow is proportional to rotor speed, so that a 40% increase in speed leads to a 40% increase in engine mass flow. Figure 2-18 illustrates the impact of rotor speed on baseline demo engine performance when *mass flow is proportional to rotor speed.* The figure shows that with the current geometry, performance is maximized at approximately 140% rotor speed, increasing thrust from 10 grams to 15 grams and thermal efficiency from 2% to 3%. Figure 2-19 compares rotor speed and efficiency for several different bearing drags. The figure shows that reductions in bearing drag can lead to a significant increase in thermal efficiency, delivering roughly 2 points of efficiency for every 12.5-point change in bearing/compressor power ratio.

Peak efficiency occurs at rotor speeds between 140% and 160% of design. If bearing drag is reduced by two-thirds to 4W and speed is increased to 140%, the engine will deliver thermal efficiencies in excess of 6%.

Turboshaft cycles

Because the initially envisioned application for the demo engine is as a propulsion system for a micro air vehicle, the preceding parametric studies focused on turbojet engines. However, portable electrical power applications will require a turboshaft engine with an integrated electrical generator. GASTURB and the Excel spreadsheet were used to assess the performance of the demo engine as a turboshaft engine. The calculations show that the baseline design would give approximately 7.5 Watts of shaft power if operated as a turboshaft engine.

In comparison to conventional engines, the demo engine offers low performance (poor TSFC or thermal efficiency). The baseline cycle has low performance because it assumes a low pressure ratio and efficiency. The pressure ratio and efficiency are low because the compressor operates with substantial heating, leading to heavy losses within the blade passages. Chapter 4 describes the mechanisms behind this phenomenon in detail. However, the essential message is that compressor performance can be substantially improved if the compressor heating is removed. An improved compressor could conceptually operate with a pressure ratio of 3.0 and an efficiency of 65%. As Table 2-3 shows, such an engine would deliver a five-fold improvement in shaft power output from 8 W to 40 W and a corresponding improvement in gas turbine thermal efficiency from 2.1% to 11%[4].

[4] The gas turbine thermal efficiency does not include shaft-to-electrical power conversion. A 10% efficient gas turbine with a 60% efficient electrical generator would have an overall power conversion efficiency of 6%.

Breakeven Analysis

Because the turbine must produce enough power to drive the compressor, gas turbine engines have a minimum break-even point. If any single component is below its break-even efficiency, the cycle will not close. The break-even efficiency is easily calculated by setting the turbine work equal to the sum of the compressor and bearing work:

This relation gives break-even efficiency as a function of engine pressure ratio (OPR) and turbine inlet temperature (Tt4). Figure 2-20 plots the relation for the demo engine baseline cycle. The

$$\dot{m}_c c_p T_{t3} (\pi_c^{(\gamma-1)/\gamma} - 1)\eta_c \eta_{brng} = \dot{m}_c (1 - \beta_{bleed}) c_p T_{t4} (1 - \pi_t^{(\gamma-1)/\gamma})\eta_t$$

$$\eta_c \eta_t \eta_{brng} = \frac{c_p T_{t3} (\pi_c^{(\gamma-1)/\gamma} - 1)}{(1 - \beta_{bleed}) c_p T_{t4} (1 - \pi_c^{-(\gamma-1)/\gamma})}$$

results show that the break-even compressor efficiency for the baseline cycle is 44% and that near the baseline every 200K increase in Tt4 drops the break-even compressor efficiency by approximately 7 percentage points.

Cycle Analysis Summary

Table 2-4 summarizes the quantitative results of the parametric cycle study. These quantitative results are only representative as the specific sensitivities vary with the exact parameters of the cycle. Nevertheless, they are useful to generate estimates of the impact of various potential design changes.

The parametric analysis leads us to the following qualitative conclusion: The *most effective* ways to improve the performance of the engine are to increase the compressor efficiency and the compressor overall pressure ratio (OPR). Efficiencies in the range of 0.50-0.65 and pressure ratios in the range 3.0-5.0 are desirable. Practical ways to accomplish this goal are described in later sections. Speed-related bearing drag is also important and the thermal efficiency of the existing geometry can be improved by a factor of 50% by increasing the rotor speed to 140% of design.

2.5 MECHANICAL DESIGN TRADES

The selection of a final design for the engine involved a number of tradeoffs between conflicting constraints. Most of these trades are component-specific and are described in more detail in Chapter 4, Component Design. However, some trades are purely the result of system-level interactions between components. These trades have a critical impact on the overall system-level design of the engine.

2.5.1 TURBINE COOLING

Turbine cooling a primary driver of the demonstration microengine design. Like most large-scale engines, the microengine turbine is designed to operate at gas temperatures well above the temperature limits of its structural material. Consequently, the turbine structure requires cooling. Otherwise, the structural temperature will reach the gas temperature and the turbine will fail.

The particular restrictions imposed on the cooling scheme design by microfabrication constraints make the demo engine cooling problem even more challenging than it is for conventional engines. First, the demo engine must handle a comparatively larger heat load. This is because the ratio of wetted area to cross-sectional flow area is large but the heat transfer coefficients and temperatures are comparable. The extra wetted area is the result of low aspect-ratio blades and a turbine disk that is directly exposed to the hot, high-heat-flux flow in the turbine.

Second, compared to conventional engines, there are fewer mechanically feasible cooling schemes for the demo engine. Finally, the demo engine has low component efficiencies and, therefore, is very sensitive to the power lost to the cooling scheme.

The following discussions describe the systems-level issues associated with turbine cooling. However, turbine cooling also affects structural design and turbomachinery design at a component level. Component-specific issues are covered in Chapter 4.

Turbine Operating Environment

Table 2-5 compares the turbine operating environments of the demo engine and a conventional engine. Like a conventional engine, the microengine is designed to operate with turbine inlet total

temperatures in the range of 1400K-1800K. Unfortunately, because the baseline microengine design is all-silicon, it has a much lower limiting structural temperature than a conventional engine. Although silicon has a melting temperature of 1685K, it has little strength at temperatures above 950K. The blades of a conventional engine can accept structural temperatures that are 300-400K hotter. The disks of a conventional engine are limited to comparable temperatures, but they are not directly exposed to the core flow as in the demo engine.

Turbine-to-Compressor Heat Transfer Cooling

In large-scale engines, the heat load into the turbine is handled using a combination of convection cooling, film-cooling, and thermal barrier coatings. Figure 2-21, illustrates a conventional cooled turbine blade. The convective-cooling and film-cooling schemes involve the circulation of cooling air bled from the compressor and passed through cooling passages in the blades. These schemes are not easily implemented in the demo engine because they increase the complexity of manufacturing. However, they do show substantial potential for improving the overall performance of the engine. See the accompanying section for more detail on convection cooling and film cooling.

Because conventional cooling schemes are difficult to include in the demo engine fabrication process, an alternative cooling scheme is required. Fortunately, the microengine has some unique properties that allow turbine-to-compressor heat transfer to be used as a mechanically simple alternate convection cooling approach.

Figure 2-23 illustrates the demo engine's cooling mechanism. Because the microengine structure is very small and because the thermal conductivity of silicon is very high, heat is easily conducted through the spool structure. The high conductivity means that substantial quantities of excess heat can be transferred easily from the turbine side of the spool to the compressor side of the spool with only a small temperature difference between the two sides. Because the spool is hotter than the compressor fluid, heat will be dumped into the compressor core flow. The result is a form of convection cooling.

Modeling and Performance Impact

Turbine-compressor heat transfer cooling scheme couples tightly the demo engine's fluidic and thermal/structural behaviors. The compressor performance in particular is sensitive to heat transfer and, consequently, the spool temperature. The compressor and turbine structural temperatures are sensitive to the turbine inlet temperature and to the heat transfer into the compressor.

The interaction between these two engine subsystems can be modeled by a simple one-dimensional lumped-parameter model. The demo engine spool structure is modeled as an isothermal compressor and an isothermal turbine, each at a different temperature, connected by a shaft with a uniform thermal resistance and a linear temperature gradient. As Figure 2-22 illustrates, the shaft conductance is controlled by varying the bonded area of the turbine disk. This structural model is described in detail in Appendix B. This structural system is coupled to the fluidic systems through fixed heat transfer coefficients on the turbine and compressor. The compressor pressure ratio and efficiency are proportional to compressor heat flux. The details of the compressor performance model are given in Chapter 4, Component Design. Changes to turbine performance are neglected. The performance of the overall cycle are calculated from the compressor performance and the baseline cycle parameters.

Based on the model described above, Figure 2-24 shows the impact of turbine-compressor heat transfer on the engine structure and compressor performance. The results show that the current design has a turbine temperature of 920 K and a compressor temperature of 850 K for a combustor inlet temperature of 1600K. This gives a turbine-to-compressor heat transfer of 52 W and drops the compressor efficiency to 0.35 from its predicted 3D adiabatic level of 0.60. The details behind these calculations are presented in Chapter 3.

The results show that the design requires substantial thermal isolation of the compressor and turbine to achieve a significant drop in compressor heat transfer and a corresponding improvement in compressor efficiency. Dropping the conductance to 10% of its baseline value drops the compressor heat transfer by 20% from 52 W to 42 W. This gives only a 4 point improvement in efficiency. Cutting the shaft conductance to 1% of its baseline value cuts heat transfer by 2/3 to 15 W, raises the efficiency to the baseline cycle value of 0.50. However this will drive the turbine wall temperature to 1350 K, requiring advanced materials or a 'barrier'

cooling scheme such as film cooling. This analysis motivated Miller to study the use of silicon carbide in a thermally isolated rotor [16]. Miller showed that a hybrid carbide and silicon structure allows an increased turbine operating temperature, thereby reducing heat transfer via the spool.

In comparison to the 1D model presented here, the 3D results of Chen show a spool temperature between 690 K on the compressor side and 815 K on the turbine side. This gives a heat transfer of 35W and a compressor efficiency of 0.40 [8]. The discrepancy is the result of two factors. First, 3D effects increase the thermal resistance of the spool, cutting heat transfer. Secondly, the 3D model predicts lower overall temperatures because its fluid model does not include the drop in efficiency (increase in compressor fluid temperatures) associated with compressor heat addition. Further modeling is underway at MIT to improve the match between 1D and 3D results [15]. Despite the discrepancy, the 1D results capture the qualitative impact of heat addition and point to the need to reduce heat transfer to the compressor by a substantial amount. Even at the 35W predicted by Chen, the compressor does not meet the 0.44 breakeven level calculated for the cycle.

2.5.2 Turbine Inlet Temperature

The requirements for turbine cooling substantially degrade compressor performance. One approach is to vary both the geometry and the inlet temperature of the turbine. If the inlet temperature to the turbine is reduced, the turbine temperature heat transfer to the spool will be reduced. The turbine structural temperature will also drop. If the thermal isolation between the compressor and turbine is then increased, the turbine temperature can be again driven up to the material limit, further reducing the heat transfer. The net result is a trade-off between improved compressor performance due to lower heat transfer and reduced turbine power due to lower turbine inlet temperature.

Figure 2-25 illustrates the impact of this thermal control concept on the performance of the demo engine. The heat transfer and consequent compressor performance are calculated from turbine inlet temperature, structural temperature, and turbine heat transfer coefficient. The baseline cycle is then recalculated with the new compressor performance and turbine inlet temperature. The plot assumes that the turbine structural temperature is kept fixed at 950 K and that the baseline turbine

heat transfer coefficient of 2580 W/m2-K is unaffected by turbine gas temperature. The cycle was calculated for several values of Tt4. The calculation shows that demo engine performance increases monotonically with turbine inlet temperature. The benefits of reduced compressor heat transfer are not overcome by the drop in turbine power associated with a lower Tt4. The demo engine turbine inlet temperature should be maintained at 1600K or higher.

2.6 CHAPTER SUMMARY

This chapter described the overall system design of the demonstration micro engine. The discussion included identification of functional requirements and constraints, cycle analysis, layout, and systems-level trades. The design effort shows that a closed-cycle, all-silicon, turbojet engine is feasible.

The proposed design assumes a low pressure ratio (1.8), low-efficiency (0.50) compressor and low thermal efficiency (less than 2%). The performance can be improved to an efficiency of 6% by increasing the pressure ratio to 3.0 and the compressor efficiency to 0.50-0.65. If structural limitations allow it, higher performance can also be achieved by increasing the rotor speed by 40%.

The design exercise shows that turbine structural temperature is the major performance-limiting requirement. The proposed turbine cooling scheme transfers heat into the compressor, leading to the low pressure ratio and efficiency. Future work should focus on reducing this heat transfer through the use of film cooling and/or advanced materials and structures. If heat transfer is dropped by 60%, a closed-cycle engine should be possible.

2.7 REFERENCES

[1] J. L. Kerrebrock, *Aircraft Engines and Gas Turbines,* 2nd Edition. Cambridge, Massachusetts: The MIT Press, 1992.

[2] G. J. Van Wylen and R. E. Sonntag, *Fundamentals of Classical Thermodynamics*, 3rd Edition. New York: John Wiley and Sons, 1985.

[3] M. J. Zucrow, *Aircraft and Missile Propulsion: Volume II, The Gas Turbine Power Plant, the Turboprop, Turbojet, Ramjet, and Rocket Engines.* New York: John Wiley and Sons, 1958.

[4] N. Maluf, An Introduction to Microelectromechanical Systems Engineering, Boston, Massachusetts: Artech House, 2000.

[5] C. C. Lin, *Development of a Microfabricated Turbine-Driven Air Bearing Rig.* PhD thesis, MIT, Department of Mechanical Engineering, 1999.

[6] L. Frechette, *Development of a Silicon Microfabricated Motor-Driven Compressor*, PhD Thesis, MIT, Department of Aeronautics and Astronautics, 2000.

[7] A. Mehra, *Development of a High Power Density Combustion System for a Silicon Micro Gas Turbine Engine*, PhD thesis, MIT, Department of Aeronautics and Astronautics, 2000.

[8] K. S. Chen, *Materials Characterization and Structural Design of Ceramic Micro Turbomachinery*, PhD Thesis, MIT, Department of Aeronautics and Astronautics, 1999.

[9] A. A. Ayon, R. Braff, C. C. Lin, H. H. Sawin, and M. A. Schmidt, "Characterization of a Time Multiplexed Inductively Coupled Plasma Etcher," *Journal of the Electrochemical Society*, Vol. 146, No. 1, Jan. 1999.

[10] A. H. Epstein et. al. "Power MEMS and Microengines," presented at IEEE Conference on solid State Sensors and Actuators, Chicago, IL, Jun. 1997.

[11] A. P. London, *Development and Test of a Microfabricated Bi-Propellant Rocket Engine*, PhD Thesis, MIT, Department of Aeronautics and Astronautics, 2000.

[12] C. Groshenry, Preliminary Design Study of a Micro-Gas Turbine Engine. MS Thesis, MIT, Department of Aeronautics and Astronautics, 1995.

[13] GASTURB Users Manual.

[14] A. Mehra, Computational Investigation and Design of Low Reynolds Number Micro-Turbomachinery, MS Thesis, MIT, Department of Aeronautics and Astronautics, 1997.

[15] H-S Moon, Personal communication. To be published in MIT GTL PhD thesis.

[16] B. Miller, "Hybrid Silicon/Silicon Carbide Microstructures and Silicon Bond Strength Tests for the MIT Microengine," MS Thesis, MIT, Department of Aeronautics and Astronautics, 2000.

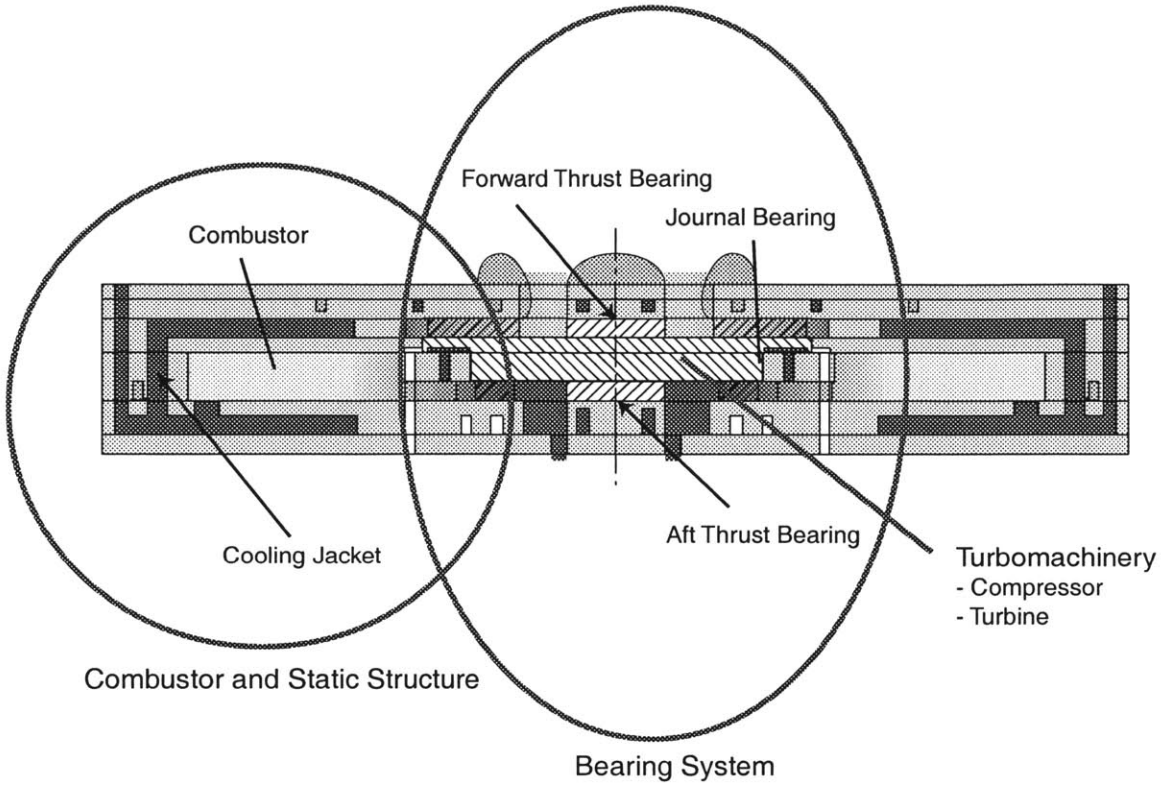

Figure 2-1: Demo engine sub-systems.

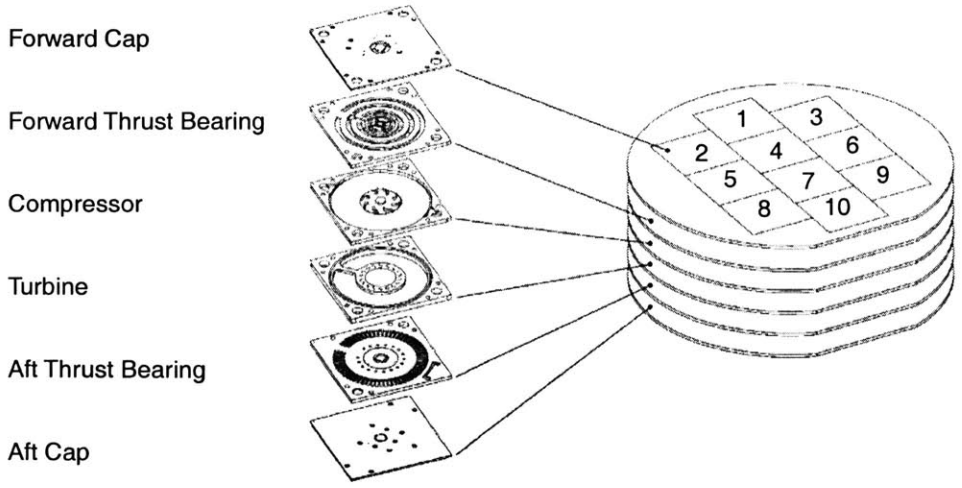

Figure 2-2: Wafer stacking concept.

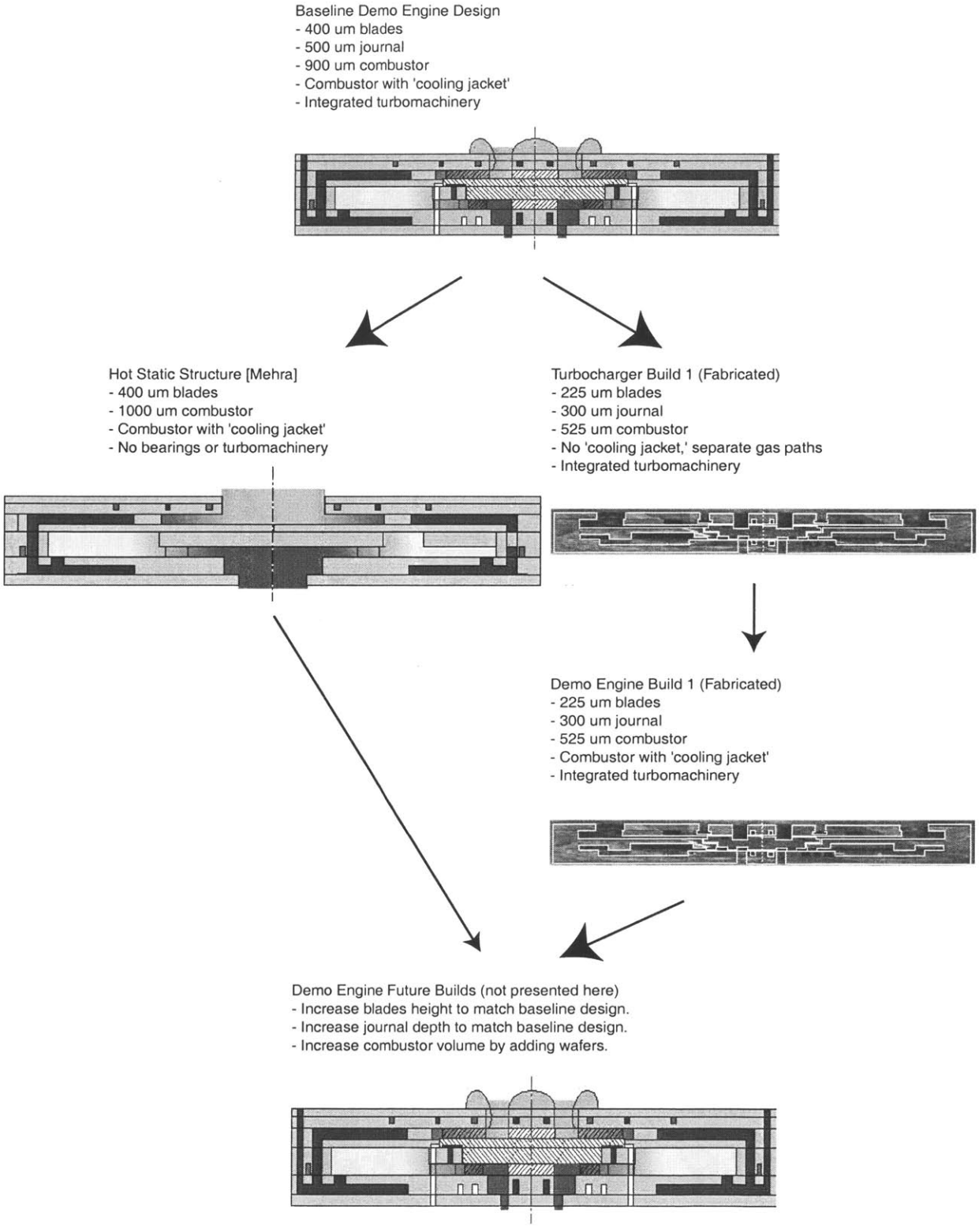

Figure 2-3: Demo engine development sequence.

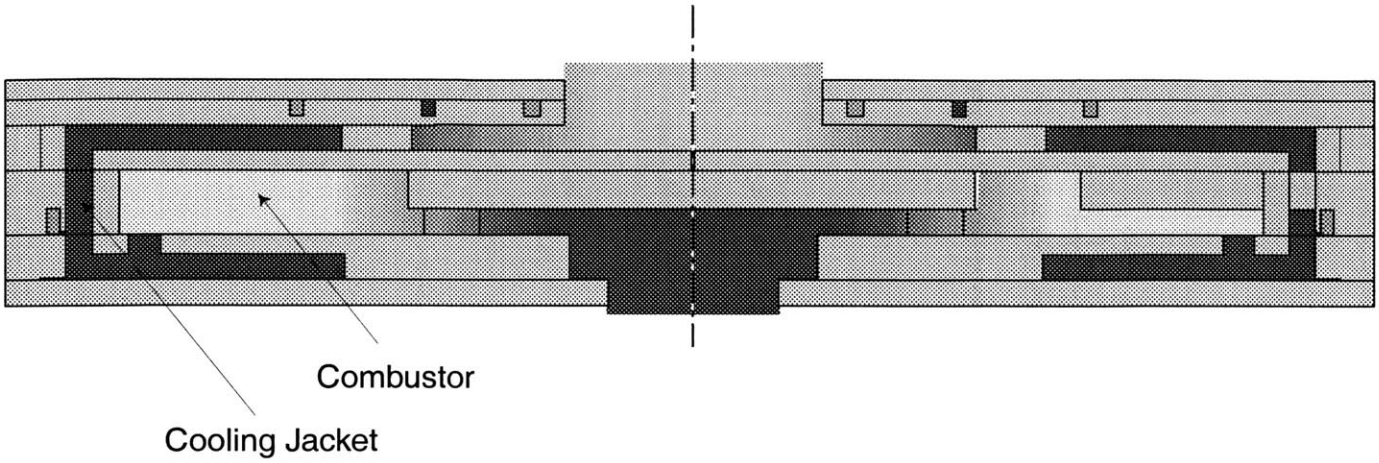

Figure 2-4: Illustration of hot static structure.

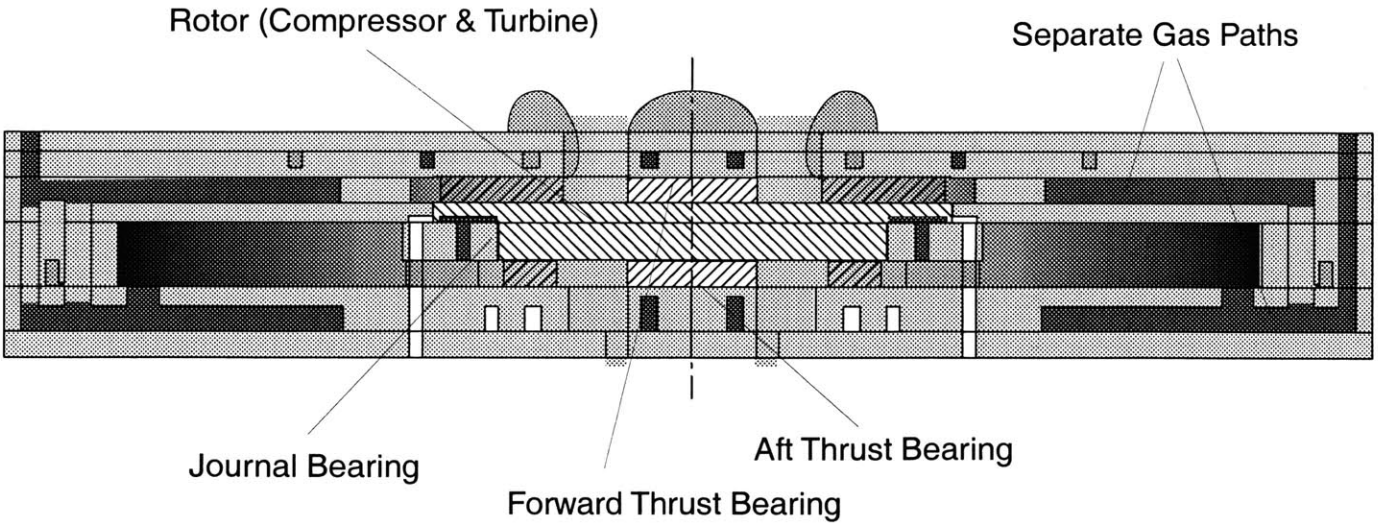

Figure 2-5: Illustration of turbocharger showing separate gas paths.

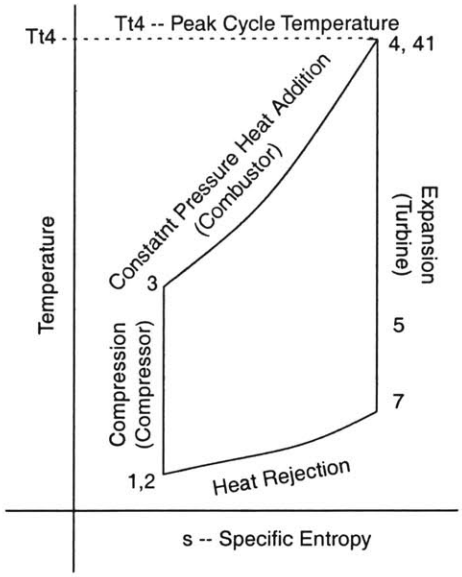

Figure 2-6: Temperature-entropy diagram of the ideal Brayton cycle.

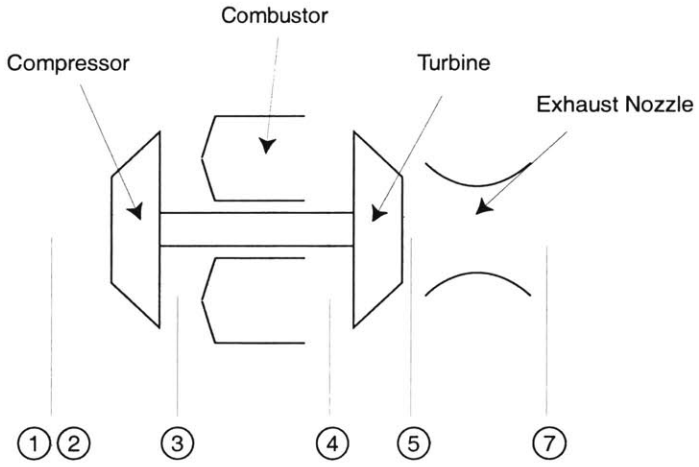

Figure 2-7: Schematic of a turbojet engine showing station numbers and components.

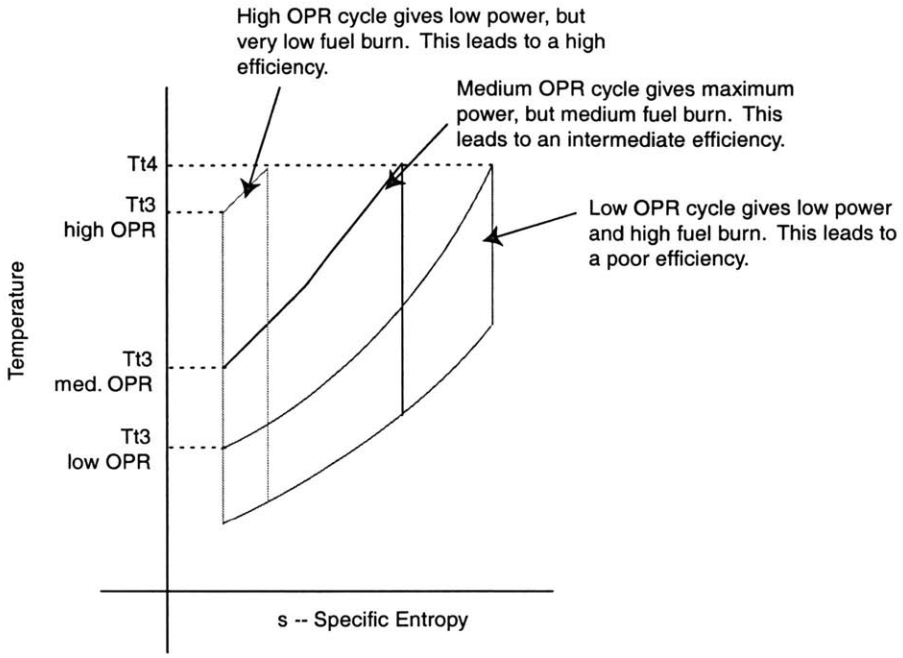

Figure 2-9: Increasing pressure ratio increases efficiency.

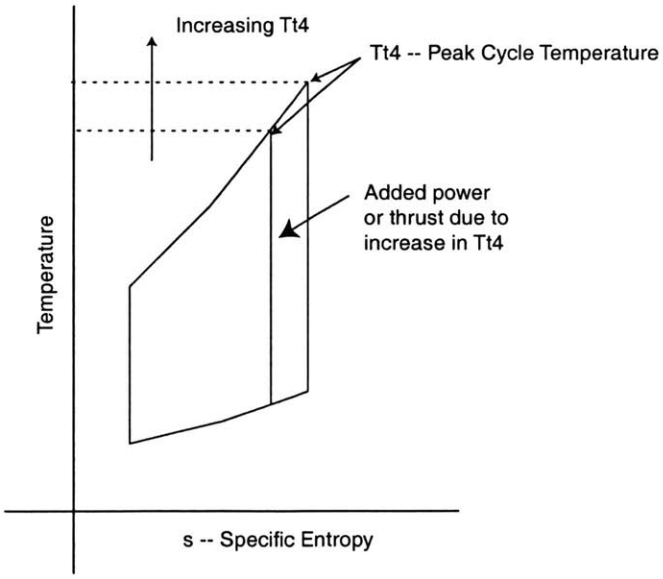

Figure 2-8: Increasing peak cycle temperature (Tt4) increases power output.

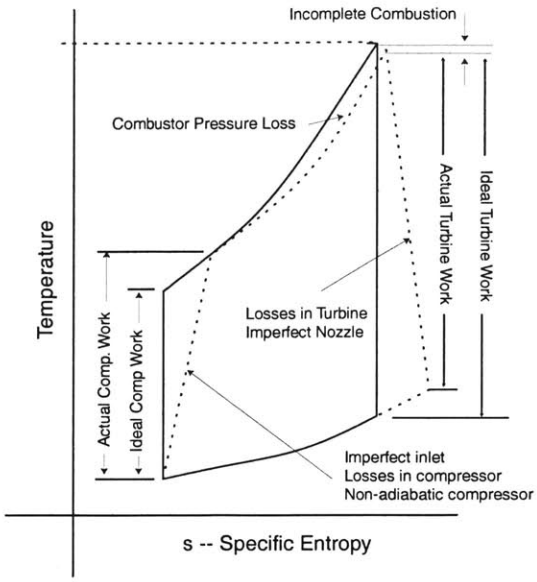

Figure 2-10: Impact of nonideal component behavior on the Brayton cycle.

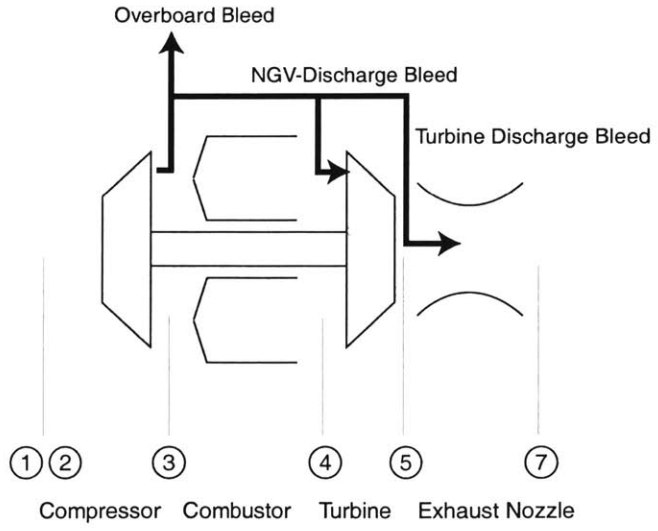

Figure 2-11: Principle types of compressor bleed in a single-stage turbojet.

Table 2-2: Comparison of GASTURB and Excel baseline cycle calculations.

		Low Performance			High Performance	
		GASTURB	Excel w/o Heat Txfr	Excel w/ Heat Txfr	GASTURB	Excel w/o Heat Txfr
Tt2	[K]	288	288	288	288	288
Tt3	[K]	393	368	473	450	412
Tt4	[K]	1600	1600	1600	1600	1600
Tt5	[K]	1464	1487	1376	1438	1458
Tt7	[K]	1464	1487	1376	1438	1458
Compressor PR	[-]	1.80	1.80	1.80	3.00	3.00
Combustor PR	[-]	0.98	0.98	0.98	0.98	0.98
Turbine PR	[-]	1.62	1.63	1.63	1.86	1.86
Nozzle PR (EPR)	[-]	1.10	1.08	1.08	1.45	1.58
Comp Isen Eff	[-]	0.50	0.50	0.50	0.65	0.65
Turb Isen Eff	[-]	0.70	0.70	0.70	0.70	0.70
Combustor Eff	[-]	0.99	0.99	0.99	0.90	0.90
Bearing Drag	[W]	13.00	13.00	13.00	5.00	5.00
Heat Transfer	[W]	-	-	50.00	-	-
Thrust	[g]	9.49	9.14	8.79	21.28	21.16
Fuel Burn	[g/hr]	16.20	16.85	15.41	17.07	17.87
TSFC	[g/g-hr]	1.71	1.84	1.75	0.80	0.84
Isp	[sec]	2105	1953	2054	4500	4262
Thrust Error	[%]	-	3.7%	7.3%	-	0.6%
Fuel Burn Error	[%]	-	-4.0%	4.9%	-	-4.7%
TSFC Error	[%]	-	-7.8%	-2.5%	-	-5.6%

Table 2-3: Baseline demo engine cycle and performance.

		Baseline		Fabricated
		Low OPR	Mid OPR	(Predicted)
Tt2	[K]	288	288	288
Tt3	[K]	473	518	603
Tt4	[K]	1600	1600	1600
Tt5	[K]	1376	1347	1360
Tt7	[K]	1376	1347	1360
Compressor mdot	[g/sec]	0.36	0.36	0.18
Compressor PR	[-]	1.80	3.00	1.60
Combustor PR	[-]	0.98	0.98	0.98
Turbine PR	[-]	1.63	1.86	1.57
Nozzle PR (EPR)	[-]	1.08	1.58	1.00
Comp Isen Eff	[-]	0.50	0.65	0.30
Turb Isen Eff	[-]	0.70	0.70	0.60
Combustor Eff	[-]	0.99	0.90	0.99
Bearing Drag	[W]	13.00	5.00	0.98
Heat Transfer	[W]	50.00	-	50.00
Compressor Bleed	[%]	5%	5%	-
Turbine Injection	[%]	-	-	40%***
Thrust	[g]	8.79	20.34	-
Shaft Power*	[W]	7.60	40.66	0.00
H2 Fuel Burn	[g/hr]	15.41	16.29	10.05
H2 TSFC	[g/g-hr]	1.75	0.80	-
H2 Isp	[sec]	2054	4495	-
H2 PSFC	[g/W-hr]	2.03	0.40	-
Butane Fuel Burn	[g/hr]	42.71	45.14	27.86
Butane TSFC	[g/g-hr]	4.86	2.22	-
Butane Isp	[sec]	741	1622	-
Butane PSFC	[g/W-hr]	5.62	1.11	-
Thermal Efficiency**	[%]	2.1%	11.9%	0.0%

* Shaft power assumes expansion through a 70% efficient turbine

** Thermal efficiency is for turboshaft power output vs fuel energy input.

*** The predicted fabricated cycle does not close and requires turbine injection (shown as a percentage of compressor flow) to reach design speed.

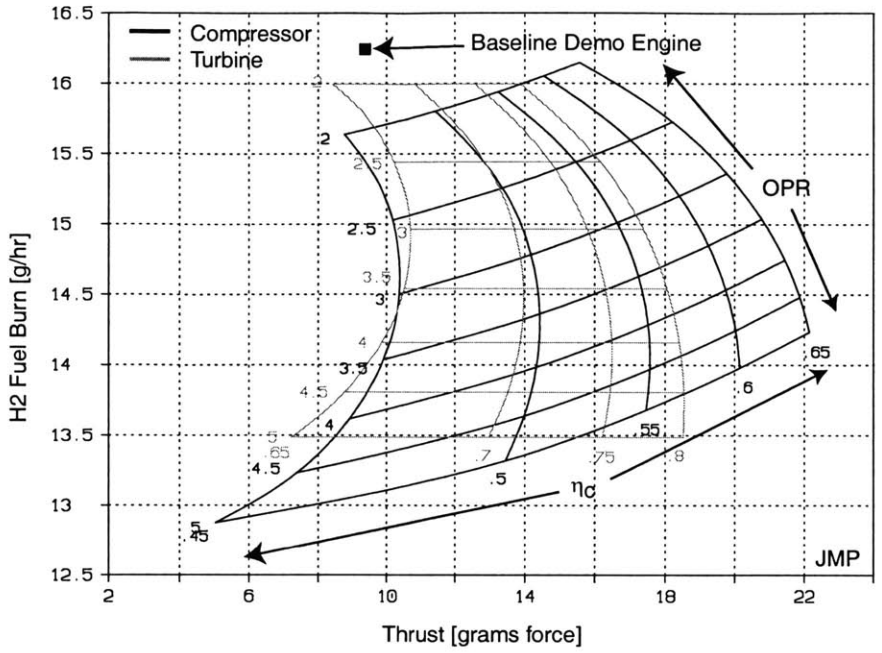

Figure 2-12: Impact of turbomachinery performance on demo engine cycle.

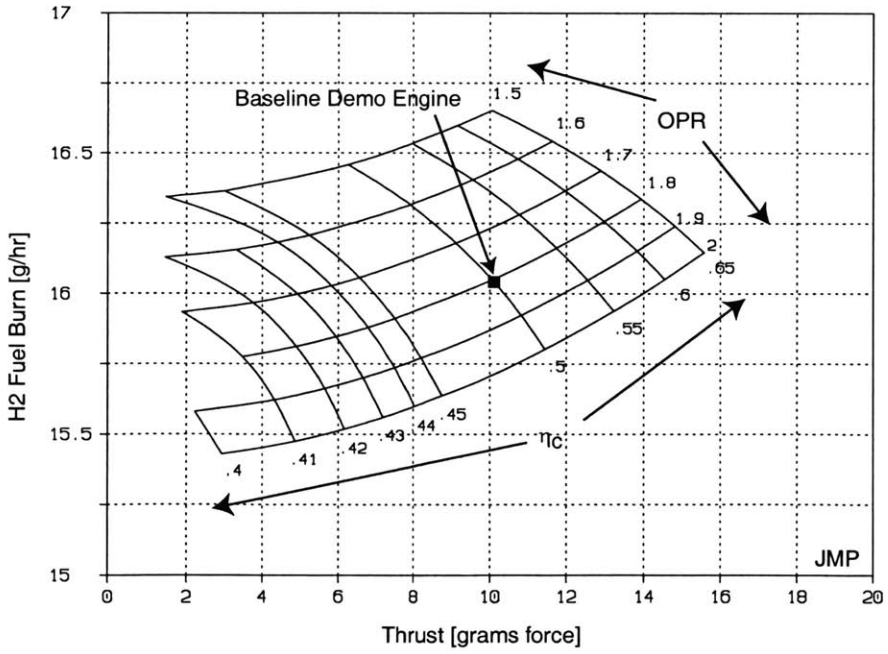

Figure 2-13: Low-pressure-ratio demo engine cycles.

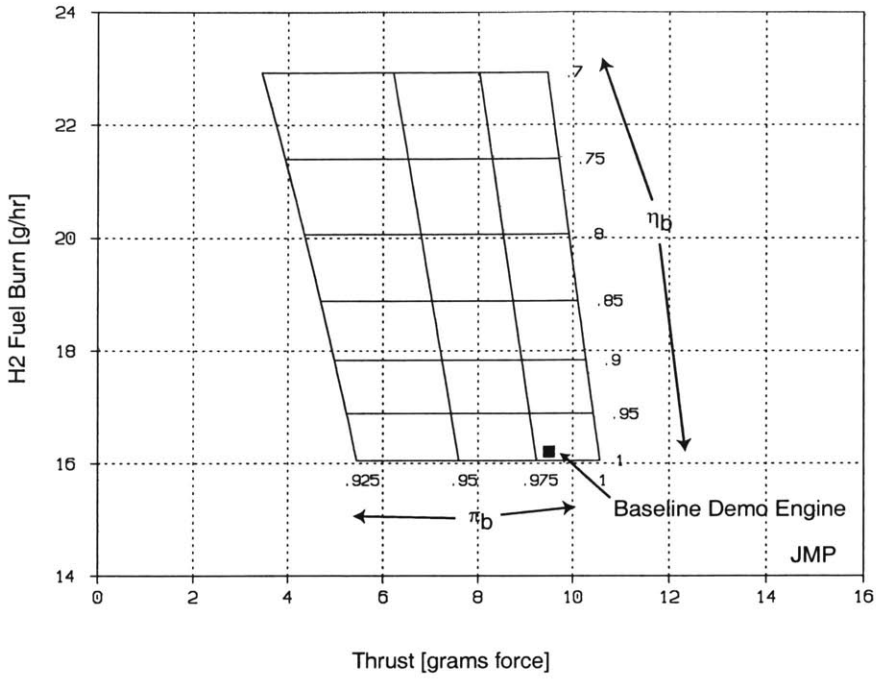

Figure 2-14: Impact of non-ideal combustor behavior on demo engine cycle.

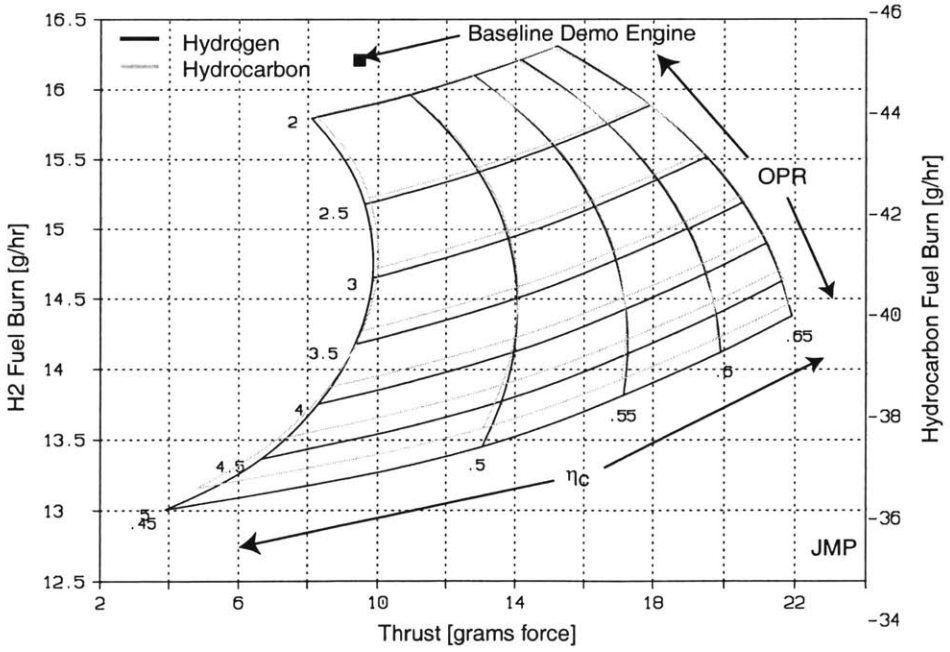

Figure 2-15: Comparison of hydrogen and hydrocarbon (kerosene) combustion results.

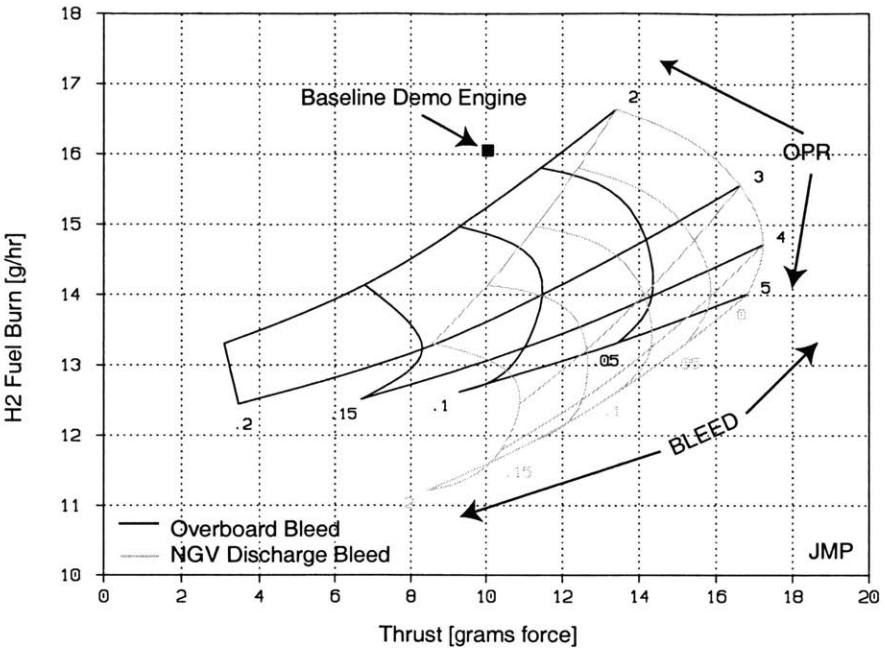

Figure 2-16: Impact of bleed on demo engine cycle.

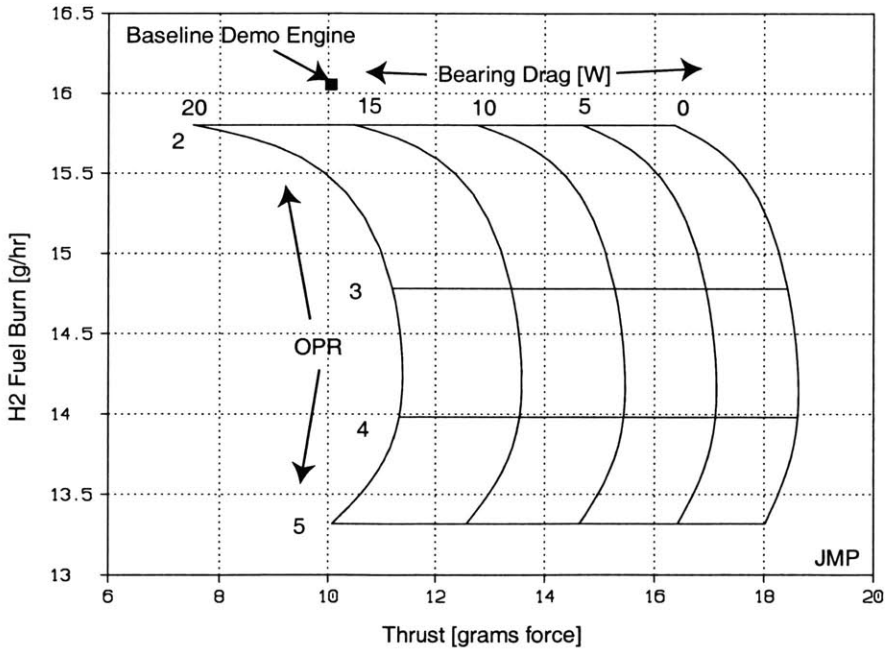

Figure 2-17: Impact of bearing drag on *fixed mass flow* demo engine cycle.

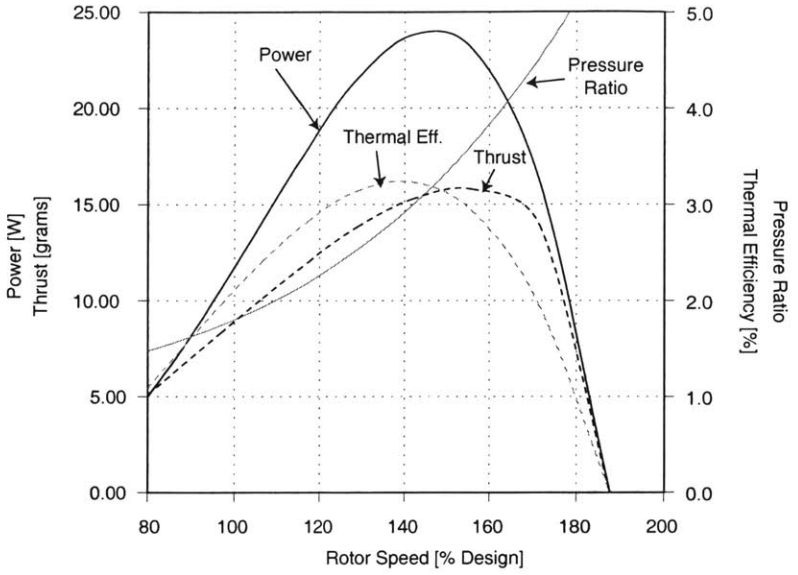

Figure 2-18: Demo engine performance as a function of speed.

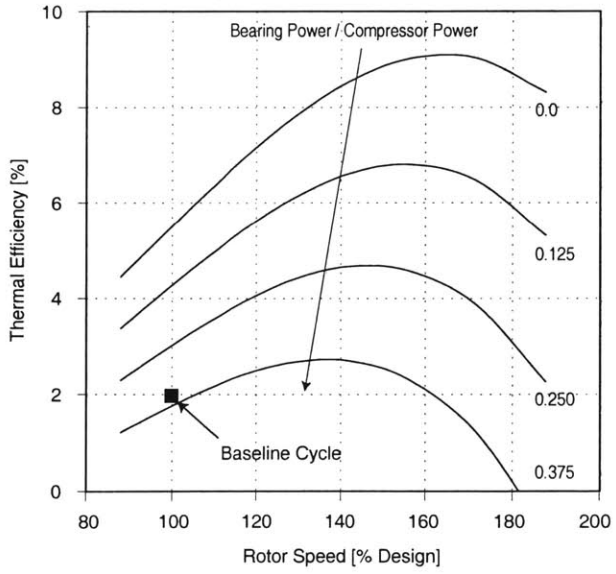

Figure 2-19: Comparison of speed and cycle efficiency for various bearing drags.

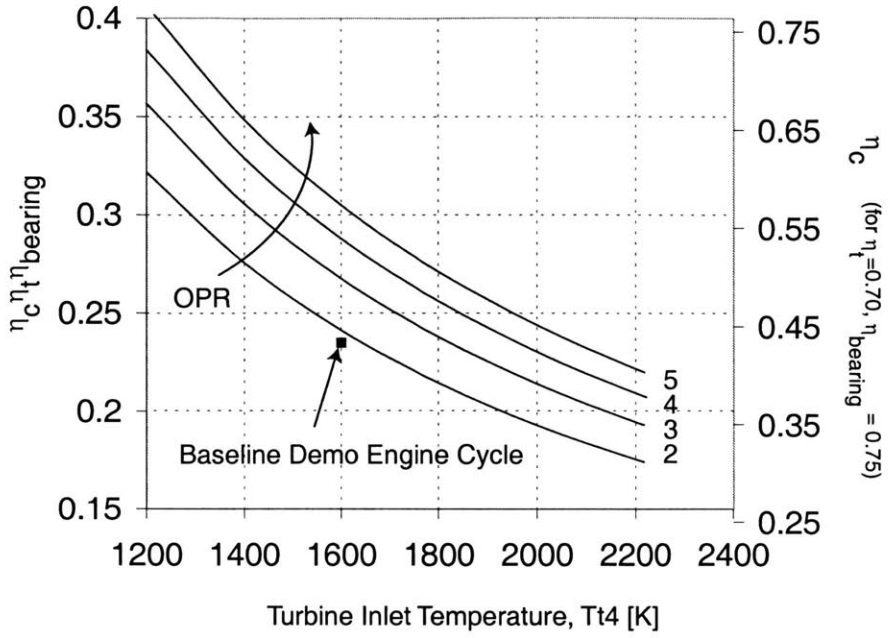

Figure 2-20: Break-even efficiency for the demo engine cycle.

Table 2-4: Summary of cycle analysis results.

Baseline	Thrust = 9-10 grams, Fuel burn = 16 grams hydrogen / hr
Turbomachinery	Thrust -50% to 50% as OPR varies from 2.0 to 5.0 Thrust +100% as compressor efficiency varies from 0.50 to 0.65 TSFC -50% as compressor efficiency varies from 0.50 to 0.65
Low OPR (OPR 1.5-2.0)	Fuel burn independent (+/-5%) of compressor performance Thrust 2 grams to 16 grams as efficiency from 0.40 to 0.65 TSFC varies 8.0 g/g-hr to 1.0 g/g-hr as efficiency varies from 0.40 to 0.65 One point of efficiency is worth between 0.2 ands 1.0 grams of thrust.
Hydrogen Combustor	Fuel burn proportional to combustor efficiency: 2.5 g/hr of fuel per 10 points of efficiency Thrust insensitive to combustor efficiency. Fuel burn insensitive to pressure ratio. TSFC +0.25 g/g-hr for every 10 points of combustor efficiency. 3.6 gram drop in thrust for every 1/2 point of compressor efficiency.
Hydrocarbon Combustior	Performance insensitive (1%) to combustion chemistry. Hydrocarbon fuel burn and TSFC ~3x hydrogen results.
Bleed	3 grams of lost thrust for every 5 points of overboard bleed. 1.5 grams of lost thrust for every 5 points of NGV discharge bleed.
Bearing drag	Max engine perfromance at 140% rotor speed 2 points of engine thermal efficiency for every 12.5 point change in bearing/compressor power ratio.
Breakeven analysis	Breakeven compressor efficiency is approximately 44%. Every 200K increase in Tt4 drop breakeven efficiency 7 points.

Table 2-5: Comparison of turbine operating environment in demo engine and conventional engines.

	MicroEngine	Conventional Engine
Tt4	1600K	1500-1800K
Max Tstruct	950K	1300K
Heat Txfr Coeff	~2000 W/m2K	~2000 W/m2K
Core Mass Flow	0.36 g/sec	20 kg/sec

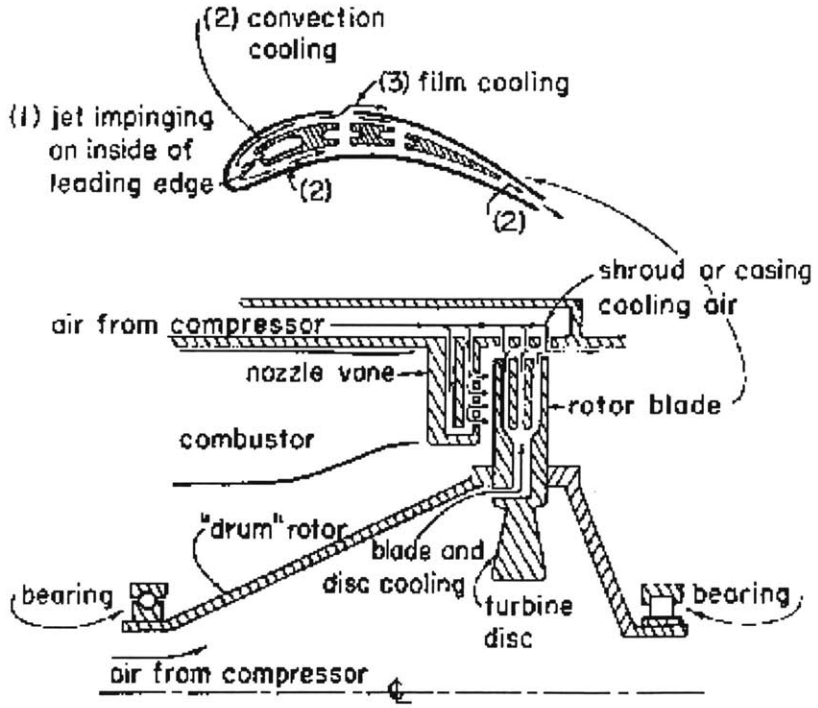

Image courtesy J. Kerrebrock

Figure 2-21: Illustration of conventional turbine cooling approaches.

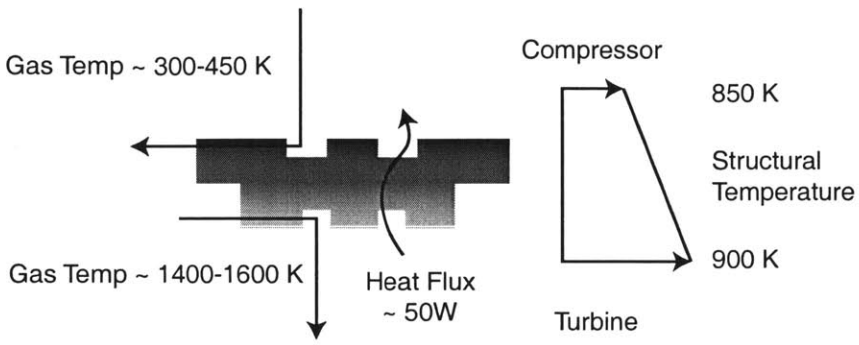

Figure 2-22: Illustration of demo engine cooling mechanism.

Figure 2-23: Varying thermal isolation by changing shaft area.

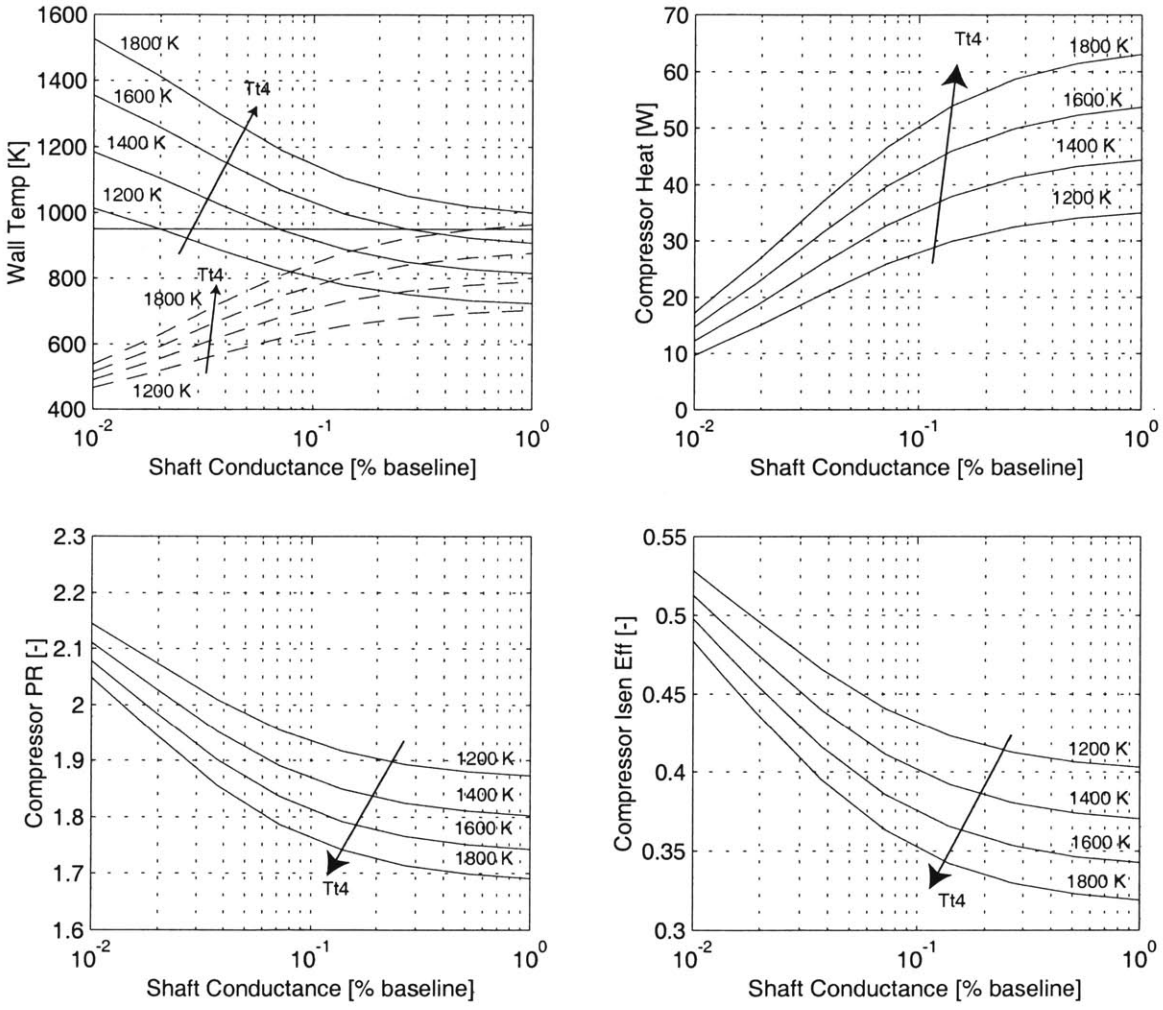

Figure 2-24: Spool thermal behavior.

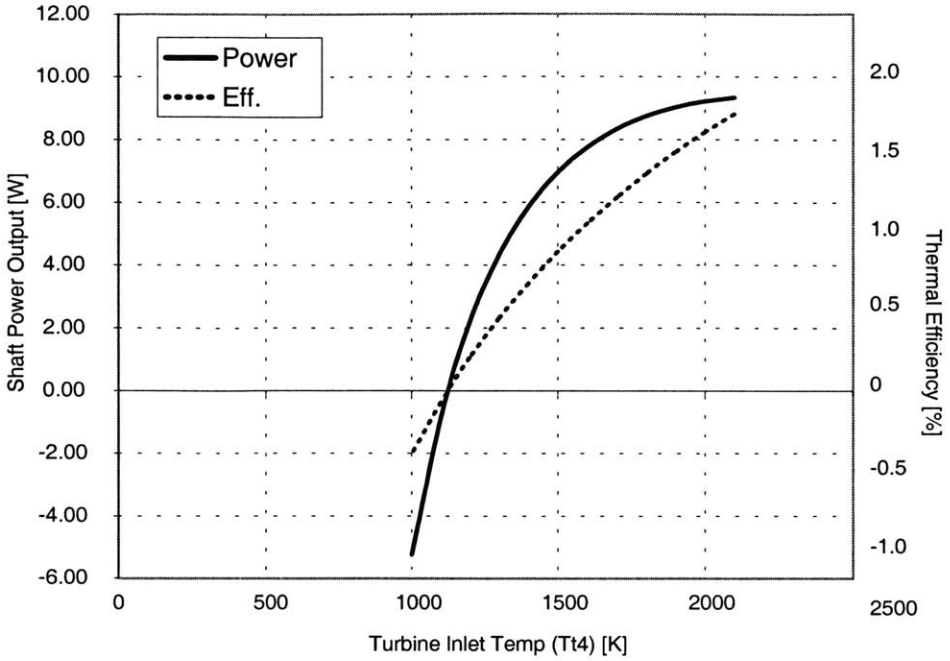
Power
Eff.
12.00
10.00
8.00
6.00
4.00
2.00
0.00
-2.00
-4.00
-6.00
Shaft Power Output [W]
2.0
1.5
1.0
0.5
0
-0.5
-1.0
Thermal Efficiency [%]
0
500
1000
1500
2000
2500
Turbine Inlet Temp (Tt4) [K]

CHAPTER 3

COMPONENT DESIGN

This chapter describes the details of component design for the demo micro engine. The goals of the chapter are to document the reasoning behind each component design, identify the critical component-level design issues and tradeoffs, and propose areas of focus for future component designs. The demo engine component design represents the cumulative effort of over 30 students, faculty, and staff on the MIT program. The discussions in this chapter focus only on issues that directly impact the overall system design of the engine. For an in-depth description of the science behind each component or subsystem, the reader should consult the references noted in Chapter 1, Introduction.

As mentioned in Chapter 2, System Design, the demonstration engine is composed of three major subsystems: (1) Turbomachinery, (2) Combustor, and (3) Bearings. The turbomachinery includes the compressor, turbine, and associated rotating structure. The combustor includes the combustor proper, the fuel injectors, and the associated static structure. The bearings include the thrust bearings, journal bearing, and the associated secondary flow system.

All of the engine subsystems were designed as part of a design-review based engineering process. First, the basic morphology was determined during the layout and systems studies. Then, the specifications and functional requirements were defined as part of the system design process. Given the morphology, specifications, and knowledge of the available fabrication capabilities, preliminary component designs and dimensions were developed. The preliminary designs were presented at a preliminary design review and modified based on outside input. These designs were then refined in detail by the other researchers in the component design groups. This final design was reviewed at a critical design review. Device drawings and masks were made from

this design for fabrication implementation. The device was fabricated with a best attempt effort to match the design intent. At the same time, the design was further analyzed using refined analysis techniques.

The remainder of this chapter describes the individual component designs, including the functional requirements, design issues, and analysis results. The fabrication results are described in Chapter 4, Fabrication.

3.1 COMPRESSOR, TURBINE, AND ROTATING STRUCTURE

This section describes the design of the engine rotating structure. The rotating structure includes the compressor, the turbine, and the associated structure.

3.1.1 COMPRESSOR

This section describes the fluid dynamic design of the demo engine compressor.

Functional Requirements and Constraints

The system studies presented in Chapter 2 show that for feasible demo engine cycles, overall cycle efficiency and power output are both improved as compressor efficiency increases and as pressure ratio increases for levels up to 5.0. The analysis also showed that an engine with a pressure ratio of 1.8 and an efficiency of 0.50 could close a cycle. The break-even efficiency is 0.40. Thus, the functional requirements for the demo engine became a pressure ratio of 1.8 and an efficiency in excess of 0.40. To achieve the ultimate target thrust of 10 grams, the compressor was sized for a mass flow of 0.36 grams.

The compressor design is constrained in the following ways: (1) The material properties of silicon constrain the maximum allowable stress to 500-1000 MPa; (2) Microfabrication capabilities constrain the geometry to two-dimensional extruded shapes.

Compressor Design

Given the functional requirements and constraints, the demo engine was designed for a tip speed of 500 m/sec, an adiabatic pressure ratio of 3.0, and an adiabatic efficiency of 50%. The geometry is illustrated in Figure 3-1. Jacobson initially designed this compressor for a 2 mm radius and a pressure ratio of 4.0 [1,2]. Jacobson analyzed the design using 2D MISES, an integral boundary layer CFD code. Youngren re-scaled and re-optimized the design to match the 4 mm radius an 0.36 g/sec mass flow of the preliminary engine design. Youngren also modified the 2D calculation to account for heat addition [4]. Gong analyzed Youngren's redesigned compressor with heat addition in 3D using FLUENT, a commercial CFD code [3]. All of the CFD codes were validated against a set of dynamically scaled experiments performed on MIT's macro-compressor rig by Shirley, Cadou, and Khan [5, 6, 7].

Compressor Performance

Figure 3-2 plots the compressor map for the demo engine as predicted by the 3D CFD calculations of Gong [3]. The map shows a predicted peak pressure ratio of 2.7 at an efficiency of 0.53 and a peak efficiency of 0.59 at a pressure ratio of 2.3 when the compressor is operated adiabatically. As discussed in Chapter 2, System Design, the demo engine operates with a 'hot' compressor for turbine cooling. At a compressor wall temperature of 800K, the compressor has a predicted peak pressure ratio of 1.8 at an efficiency of 0.33 and a predicted peak efficiency of 0.36 at a pressure ratio of 1.7. The cooling scheme causes a more than 30% drop in the predicted performance of the compressor, pushing it below the 44% cycle break-even efficiency predicted in Chapter 2.

Modeling Heat Transfer

2D and 3D CFD are powerful tools for design and analysis, however they remain too complicated to implement in systems studies. However, the CFD calculations of Gong and Youngren both show that heat transfer substantially influences the performance of the demo engine compressor, and therefore, the overall cycle. A simplified model of this behavior is required for incorporation into system performance studies.

Three factors must be accounted for to accurately model compressor behavior in the presence of heat addition: (1) changes in efficiency, (2) changes in pressure ratio, (3) changes in mass flow.

All three factors can be accounted for with a simple 'pre-heating' model of compressor behavior. This model breaks the non-adiabatic compression process into a constant-pressure heating at the inlet pressure followed by an adiabatic compression process to the final pressure. The concept is illustrated in Figure 3-3. Gong initially validated this model against 3D CFD for efficiency predictions [3]. As shown here, the model is also valid (+/- approximately 10%) for pressure ratio and mass flow prediction as well.

Given a specified heat flux calculated from predicted heat transfer coefficients, the inlet gas temperature, and the structural temperature, the efficiency of a compressor with heat addition can be predicted by the following equation:

This equation simply debits the efficiency of the compressor by the ratio of the work required to

$$\eta = \eta_{adiab} \frac{T_{t2}}{T_{t2} + \Delta T_{heat}} \qquad \text{where} \qquad \Delta T_{heat} = \dot{Q} / (\dot{m} c_p)$$

compress the flow to a given pressure ratio after heating versus before heating. The ΔT_{heat} term is simply the increase in flow temperature associated with heating so that $T + \Delta T_{heat}$ is the new effective inlet temperature. Figure 3-4, taken from Gong, compares this model and CFD calculations for a variety of compressor operating points, designs, and inlet conditions. The model matches the CFD results to within 10%.

The same argument can be extended to model changes in pressure ratio. If flow in the demo engine compressor is modeled as an incompressible, the pressure rise across the compressor will be proportional to the centrifugal force on a fluid element, $\rho(\omega R)^2$. If all heating occurs prior to compression, the heat flux will affect fluid density, and hence pressure rise, through the ideal gas law, $P=\rho RT$. The pressure rise with heat addition is then:

And the pressure ratio is:

$$\Delta P = \Delta P_{adiab} \frac{T_{t2}}{T_{t2} + \Delta T_{heat}}$$

$$\pi_c = 1 + (\pi_{c\,adiab} - 1) \frac{T_{t2}}{T_{t2} + \Delta T_{heat}}$$

Figure 3-5 compares this model of pressure ratio to Gong's 2D and 3D CFD calculations. The figure shows that the model matched the calculations to within 10% for adiabatic pressure ratios below 2.0. As the pressure ratio increases, the incompressible flow assumption breaks down and the error increases rapidly. In all cases, the model over-predicts the pressure ratio.

The argument can also be extended to model changes in compressor mass flow. The peak efficiency of the compressor will occur when the velocity triangles of the flow are matched to the blade angles. If rotor speed is held fixed, this will correspond to a specific value of flow velocity. At this condition, the mass flow in the blade passages will depend to first order only on the inlet gas properties. Assuming a specified velocity, the mass flow through the demo engine

$$\dot{m} = \dot{m}_{adiab} \frac{T_{t2}}{T_{t2} + \Delta T_{heat}}$$

compressor will be proportional to the inlet density. Thus, engine mass flow can be modeled:

Figure 3-6 compares this model of pressure ratio to Gong's 2D and 3D CFD calculations. The figure shows that the model matched all calculations to within 5% for adiabatic pressure ratios below 2.0 and to within 15% for all cases.

Modified Geometry

Several modifications to the baseline geometry may improve performance. Reduced blade sweep increases pressure ratio and engine mass flow without sacrificing efficiency. Hollow blades can reduce tip drag and blockage. A tip shroud may also improve performance if adequate seals can be developed. The fluid dynamic consequences of these modifications are being studied in detail by Gong and Kahn [3, 6].

Summary

The demo engine compressor design is dominated by microfabrication factors. Performance is limited by three primary factors: (1) heat transfer due to turbine cooling, (2) Reynold's number

effects, and (3) blade geometry. Of these factors, heat transfer is the most significant, dropping the compressor pressure rise and efficiency by 60% from their adiabatic values.

3.1.2 TURBINE

Figure 3-1 illustrates the microengine turbine design. The turbine is designed for a pressure ratio of 1.2, a mass flow of 0.345 g/sec, and a structural temperature of 950K at an inlet gas temperature of 1600K. Like the compressor, the turbine was designed in 2D using MISES. Jacobson developed an initial cold turbine design used in Lin's micro bearing rig [15]. This design was analyzed in an adiabatic, 300K inlet 3D CFD calculation by Mehra who found that the 3D turbine had well-behaved flow with attached boundary layers and no significant three-dimensional flow geometry. Mehra found a 3D adiabatic turbine efficiency of 0.85 versus a 2D efficiency of 0.95 [2][5]. Youngren designed a new turbine for the demo engine. This design accounted for heat transfer effects into the 950K structure [4]. The new turbine was also redesigned to deliver a higher specific power output. Youngren's 2D calculations show a turbine total-to-total isentropic efficiency of 0.91. Using Mehra's ratio of 2D to 3D efficiency, this corresponds to the 'baseline' 3D efficiency of 0.70. Phillippon is analyzing the demo engine turbine in 3D using the Fluent commercial CFD code [8]. The results of these calculations were not available at the time of writing.

Like the compressor, the turbine is sensitive to heat transfer. Cooling the turbine boundary layers, increases their density, causing an increased tendency for the layer to centrifuge outward. This effect is less prominent in the turbine due to the beneficial pressure gradient. Like the compressor, the turbine efficiency is sensitive to heat transfer. However, the impact is the turbine is much smaller due to the high inlet temperature. Assuming the same pre-cooling / pre-heating model used for the compressor, the turbine efficiency is:

---

[5] 2D and 3D refer to the CFD calculations used to derive the efficiency estimates.

$$\eta = \eta_{adiab} \frac{T_{t4} - \Delta T_{heat}}{T_{t4}}$$

For a turbine inlet temperature of 1600K and 50W of heat transfer, this gives an efficiency ratio of 0.90.

The current turbine design is based on the initial 2D compressor and turbine designs of Youngren. A detailed analysis of the turbine design is currently ongoing. Preliminary indications suggest that the current turbine design is mismatched to the compressor due to three-dimensional effects.

3.1.3 Spool Structure

This section briefly describes the major issues associated with the structural design of the demo engine rotating structure. For details, consult references [10, 11, 12]. The four principal issues that must be addressed for spool structural design are (1) material properties, (2) rotor stresses, (3) disk deflection, and (4) creep.

Functional Requirements and Constraints

The functional requirement of the rotating structure is to maintain structural integrity at a compressor tip speed of 500 m/sec and a turbine gas temperature of 1600K. In addition, the spool structure must implement the turbine cooling scheme. The constraints on the spool structural design are imposed by microfabrication and include the use of silicon as a material and the use of extruded 2D microfabrication techniques.

Material Properties

The demo engine is fabricated from single crystal silicon. Silicon is used because tools currently exists to fabricate micro structures with the precision necessary for a microengine. Single crystal silicon has excellent mechanical properties at low temperatures. However its mechanical properties degrade rapidly with increasing temperature. This necessitates cooling of the microengine structure. If tools existed to manufacture micro structures from high-temperature refractory ceramics such as silicon carbide or silicon nitride, these materials would be preferred to

silicon. Lohner gives a comprehensive discussion of the merits and various materials including silicon and silicon carbide for microengine applications [9].

The mechanical properties of Silicon are summarized in Table 3-1. From the perspective of spool structural design, the most important material characteristics are failure strength (σ_{max}), centrifugal strength ($\sigma_{max}^{1/2}/\rho$), maximum operating temperature, and thermal conductivity. The failure strength, particularly in the form of centrifugal strength, determines the maximum operating speed of a given rotor design (rotor stress scales with the square of rotor speed). The maximum operating temperature determines the level of turbine cooling required for a given gas temperature. The thermal conductivity determines the level of heat transfer from the hot sections to the cold sections of a given engine geometry.

High temperature yield behavior is a particularly important material property of single crystal silicon. Although silicon melts at 1688 K, it loses mechanical strength at much lower temperature. At temperatures above approximately 900K, the yield strength of silicon decreases rapidly. Figure 3-7 illustrates the yield strength versus temperature [9]. Furthermore, once the stresses in the structure exceed this strength and the material begins to yield, the strength drops even further leading to a continuous strain. The practical consequence of this behavior is that the hotter components must operate at lower stresses and critical stresses in components such as the rotor cannot be allowed to exceed the yield strength even in transients. Based on the data presented in Figure 3-7, 950 K is a practical temperature limit for highly stressed (100s of MPa) rotating structures.

Stress

Stress is the primary factor limiting the operational speed, and, hence, pressure-ratio, of the demo engine rotor. The demo engine is built entirely from silicon and, therefore, has a maximum operating stress of approximately 500 MPa at the design temperature of 950K. There are three important stresses in the rotor structure: (1) disk stress, (2) compressor blade root stress, and (3) turbine blade root stress. The stresses in the compressor and turbine disks are the result from centrifugal forces as the rotor speed increases. The disks must hold themselves together. They must also retain the blades. Chen calculated the disk stress for a 'generalized' micro engine and

found that it was below 600 MPa. [10]. Ye verified the results for the demo engine geometry [11].

Compressor and turbine blade root stresses are the result of a combination of fluid pressure forces and centrifugal forces that attempt to 'fold' the blade over. Chen showed that centrifugal forces are the primary factor setting the blade root stress of the demo engine, fluid pressures playing a minor (less than 10%) role. Chen also showed that the root stress in the compressor blades is not critical due to their low aspect ratio (blade height/chord) [10]. For the demo engine geometry with solid blades, the maximum stress in the blades is approximately 160 MPa at the design speed of 1.2 million RPM. Blade root stress can be reduced by hollowing the blades. Miller showed that this stress can be reduced to 100 MPa by hollowing the blades [12]. Stress at the blade root is also a function of the fillet radius at the root of a blade. According to Chen's calculations, the stress at the blade root can vary by 50% as the fillet radius moves from 26 um to 38 um. The demo engine baseline design calls for 40 um fillets on 400 um tall blades.

Deflection

The demo engine is designed with precision gaps for thrust bearing, journal bearings, and tip clearances. As a result, the speed-dependent deformation of the rotating structure is also important. Deflection calculations must account for centrifugal effects, differential thermal-expansion effects, and temperature-dependent changes in material properties. Chen initially studied the deflection of a general microengine rotor design. Ye studied the deflection of the demo engine structure, accounting for all factors. The most important result of the study is the extensive deflection of the compressor tip at design speed. Because the compressor overhangs the turbine and because the compressor blades are large, the spool has a strong 'umbrella' mode that curls the compressor over the turbine. This mode opens the compressor tip clearance and pinches the compressor 'rim seal.' To avoid contact between the rim seal and the static structure, the seal was not implemented in the fabricated demo engine and turbocharger devices described

here.[6] The results also show minor changes in journal bearing and thrust bearing operating clearances.

Creep

Creep is the final major structural concern for the demo engine design. In conventional engines, turbine disks are 'creep limited,' meaning that their lifespan is set by the time it takes for the disk to grow a specified amount under continuous high-temperature loading. Chen showed that plastic-yield behavior of single-crystal Silicon, creep is less of a concern for the demo engine. If the spool is operating at stresses below the temperature-dependent yield limit, the structure will have elastic behavior with little or no creep effects. If the structure operates beyond this stress, the silicon will 'flow,' causing instantaneous failure. For additional details on the demo engine's predicted creep behavior consult Chen [10].

3.1.4 Spool Thermal Design

The thermal design of the spool controls the turbine temperature and consequently the maximum allowable stress. In the demo engine, the spool structure is cooled by conducting heat from the turbine structure into the compressor flow. This scheme has a number of systems consequences. It is therefore described in Chapter 2, System Design.

3.2 Combustor and Static Structure

Fuel is burned in the combustor to raise the temperature of the compressor discharge flow, energizing it to drive the turbine. Because the combustor controls the peak temperature of the cycle, it is the primary determinant of the engine's power output. The combustor requires flow geometry to direct the core flow out of the compressor into the combustor and out of the combustor into the turbine. This flow path also insulates the combustor, preserving thermal efficiency. Together the combustor and the associated flow path constitute the engine 'static structure.' The static structure design is considerably less difficult than the rotating structure

---

[6] Given the predicted deflection, the rim seal is not required at design speed because the compressor disk deflects enough to effectively seal the compressor backside (journal pressurization) plenum. However, experimental dies have not reached design speed and the rim seal will be re-instituted in future builds for sealing at lower speeds.

design. Nevertheless, the static structure design has a significant impact on engine sizing and fabrication.

The combustion process involves two fundamental steps: fuel mixing and combustion. Fuel mixing includes injection of the fuel and diffusion of the fuel into the compressor discharge air to create a fuel/air mixture. Combustion involves ignition and chemical reaction of the fuel/air mixture. Together both steps must be accomplished in the time it takes the main air flow to move from the compressor discharge to the turbine inlet. The mixing time is controlled by the relative scale of the mixing jet and the core flow. Faster mixing can be achieved by using a larger number of smaller fuel injectors. The chemical reaction time is independent of geometry. It is instead governed by the associated chemical kinematics of the combustion reaction. Increasing temperature increases reaction rate, decreasing reaction time. Increasing the pressure also leads to an increase in reaction rate, although this dependence is weaker than the temperature dependence.

3.3 Bearings and Secondary Flow

The demo engine rotor is supported by a set of gas bearings that suspend the rotor radially and axially. A pair of opposed thrust bearings supports the rotor axially. A circular journal bearing on the rim of the turbine supports the rotor radially. Both bearings are hydrostatic and are supplied with external air.

The primary functional requirement of the bearing system is to prevent the rotor from striking wall surfaces at speeds of up to 1.2 million RPM. This requires stable operation of the bearings over the full range of speeds. The primary design constraints are fabrication capabilities and flow usage. Ultimately, a self-supporting engine would require internally tapped bearings, and the bearing system would have to work without using an excessive fraction of the compressor mass flow. In this case, hydrodynamic bearings, are preferred because they do not require bleed flows. To simplify testing, the current demo design uses externally pressurized hydrostatic bearings.

Thrust Bearings

The demo engine thrust bearings are of the capillary/inherent restrictor design described by Lin in [13]. These bearings operate by injecting pressurized air through a series of long capillaries into a narrow gap. The specific demo engine has twenty 11 um diameter, 100 um long restrictors evenly spaced around a circle at a radius of 0.75 mm. The bearing gap totals 7 um (3.5 on either side of the rotor) and has a radius of 1 mm. Microfabrication and programmatic constraints are the primary drivers of the thrust bearing design. This led to a design with the maximum similarity to the existing and demonstrated thrust bearings of [13]. The specific demo engine design was analyzed for stiffness by Jacobson [15]. Unlike the devices of [14], the demo engine thrust bearings are a new design. Their success, documented in Chapter 6, Experimental Results, further confirms the validity of the current design methodologies.

Journal Bearing

The demo engine journal bearing retains the rotor in the radial direction. The bearing is simply a narrow (15 um) gap between the turbine disk and the engine static structure. As illustrated in Figure 3-8, the bearing has provisions for an external tap that leads to the back of the compressor disk. This tap can be used to measure the pressure on this side of the journal bearing or to set that pressure. As originally designed, the journal bearings was to be operated hydrodynamically. Hydrodynamic operation requires a side load for stability. Experimental results with the micro bearing rig show that externally-supplied hydrostatic operation of the bearing should allow operation at the designed rotor speed of 1.2 million RPM. As a result, the fabricated devices were modified for hydrostatic operation.

Secondary Flow System

As discussed above, both bearing systems require external pressurization. At the same time, the engine was designed to use only front-side fluidic interconnects to make it compatible with installation in a micro air vehicle. This led to a secondary flow system that is somewhat more complicated that the systems seen in the devices of [13] and [14]. In particular, the demo engine secondary flow system must travel from the device front surface to the center of the die via the outer edge and the back surface. This is done to supply the journal and aft thrust bearing with air while preserving the thermal isolation of the combustor. As discussed later in Chapter 6, Experimental Results, the secondary flow system contributed to the limits on device operation.

3.4 REFERENCES

[1] S. A. Jacobson, "Aerothermal Challenges in the Design of a Microfabricated Gas Turbine Engine", AIAA 98-2545, 29th AIAA Fluid Dynamics Conference, Albuquerque, NM, June 1998.

[2] A. Mehra, "Computational Investigation and Design of Low Reynolds Number Micro-Turbomachinery," MS Thesis, MIT, Department of Aeronautics and Astronautics, 1997.

[3] Y-F Gong, Personal Communication, MIT GTL, 2000.

[4] H. Youngren, Personal Communication, MIT GTL, 2000.

[5] G. Shirley, MS Thesis, MIT, Department of Aeronautics and Astronautics, 1998.

[6] K. Khan, Personal Communication, MIT GTL, 2000. To be published in MIT PhD thesis

[7] C. Cadou, Personal Communication, MIT GTL, 2000.

[8] Baudoin Phillippon, Personal Communication, MIT GTL, 2000, To be published in MIT MS thesis.

[9] K. A. Lohner, "Microfabricated Refractory Ceramic Structured for Micro Turbomachinery," MS Thesis, MIT, Department of Aeronautics and Astronautics, 1999.

[10] K. S. Chen, *Materials Characterization and Structural Design of Ceramic Micro Turbomachinery*, PhD Thesis, MIT, Department of Aeronautics and Astronautics, 1999.

[11] W-J Ye, Personal Communication, MIT GTL, 1999.

[12] B. Miller, "Hybrid Silicon/Silicon Carbide Microstructures and Silicon Bond Strength Tests for the MIT Micorengine," MS Thesis, MIT, Department of Aeronautics and Astronautics, 2000.

[13] C. C. Lin, *Development of a Microfabricated Turbine-Driven Air Bearing Rig.* PhD thesis, MIT, Department of Mechanical Engineering, 1999.

[14] L. Frechette, *Development of a Silicon Microfabricated Motor-Driven Compressor*, PhD Thesis, MIT, Department of Aeronautics and Astronautics, 2000

[15] S. A. Jacobson, Personal Communication, MIT GTL, 2000.

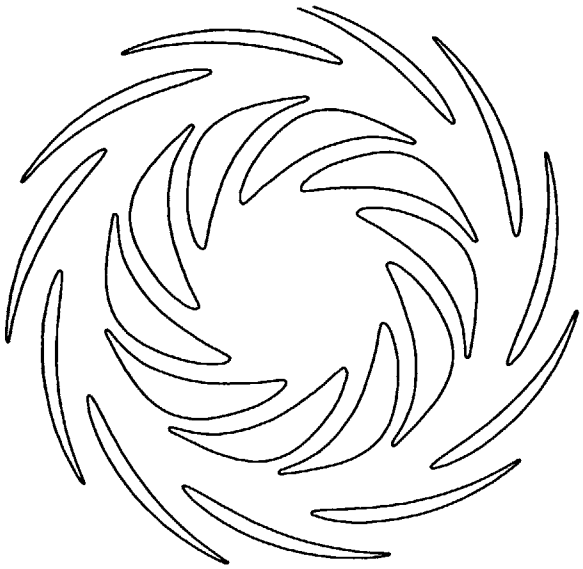

8 mm

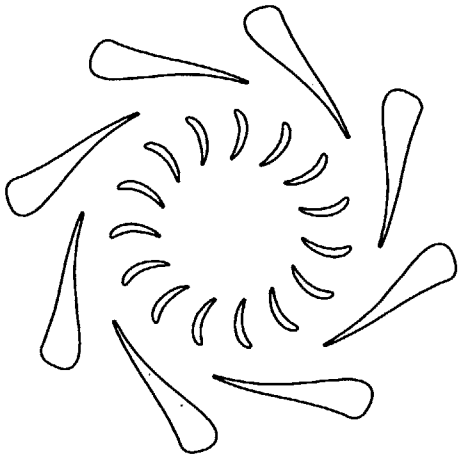

6 mm

Compressor Design Parameters:

Mass Flow:	0.36 g/sec
Pressure Ratio (Adiabiatic):	3
Pressure Ratio (Hot):	1.8
Adiabatic Efficiency:	0.50
Wall Temperature:	850 K
Gas Temperature (Inlet):	300 K
Blade Height (Span):	400 um

Turbine Design Parameters:

Mass Flow:	0.345 g/sec
Pressure Ratio (Adiabiatic):	1.6
Pressure Ratio (Hot):	1.6
Adiabatic Efficiency:	0.70
Wall Temperature:	850 K
Gas Temperature (Inlet):	1600 K
Blade Height (Span):	400+ um

Figure 3-1: Compressor and turbine blade geometry.

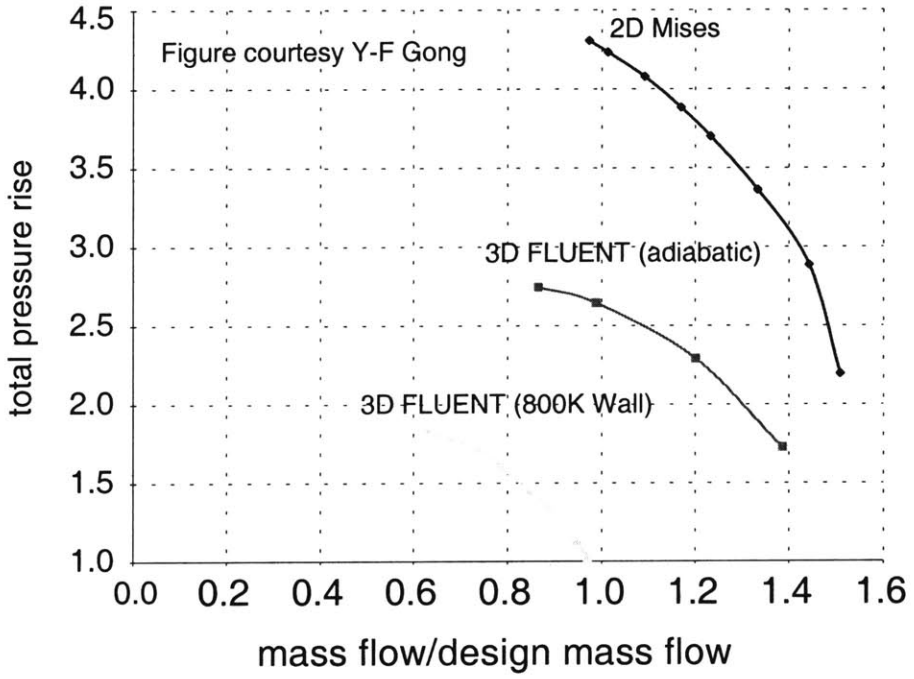

Figure 3-2: Compressor speedlines (100%) predicted by CFD.

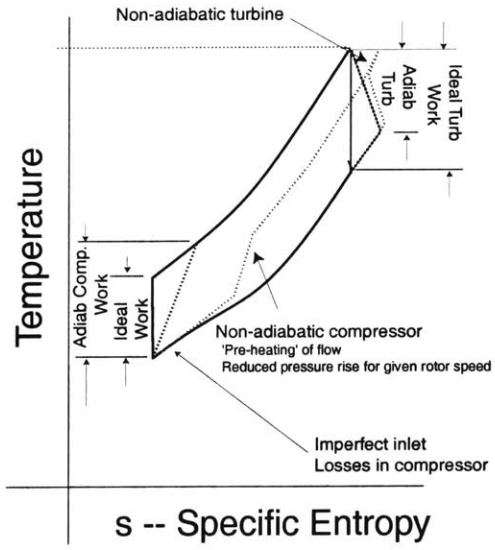

Figure 3-3: Hot compressor behaves as 'pre heated' cycle.

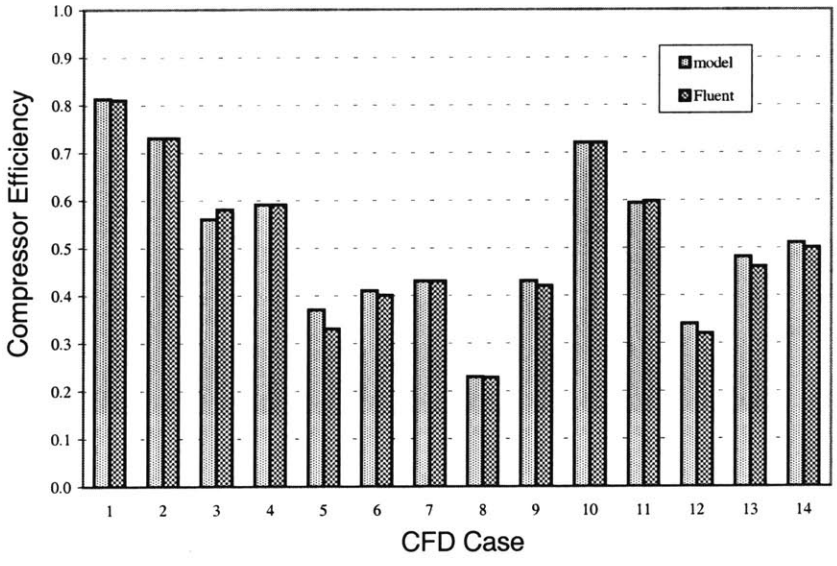

Figure 3-4: Comparison of efficiency model to CFD results.

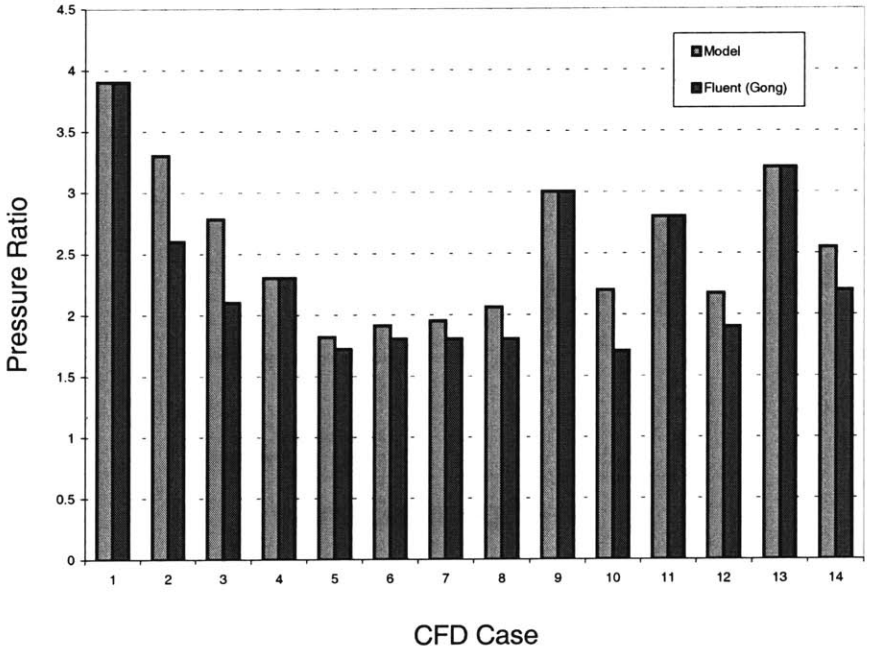

Figure 3-5:Comparison of pressure ratio model to CFD results.

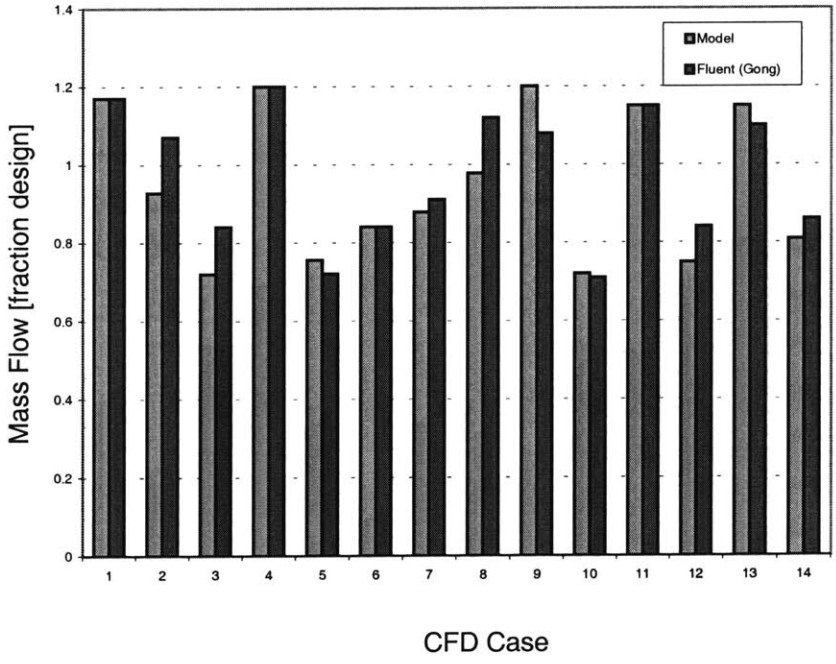

Figure 3-6: Comparison of mass flow model to CFD results.

Table 3-1: Material properties of silicon.

Density	[g/cm3]	2.33
Elastic Modulus	[GPa]	130-190
Failure Strength	[Mpa @ 25C]	1000-4000
Centrifigual Strength	[m/s]	1000
Hardness	[GPa]	10-11
Thermal Expansion	[10-6/K]	2.6-4.0
Thermal Conductivity	[W/m-K]	125-150
Specific Heat	[J/kg-K]	750
Poisson Ratio	[-]	0.28
Max Op Temp	[K]	900-950 (creep)

** All data from Lohner, MIT MS Thesis, 1999

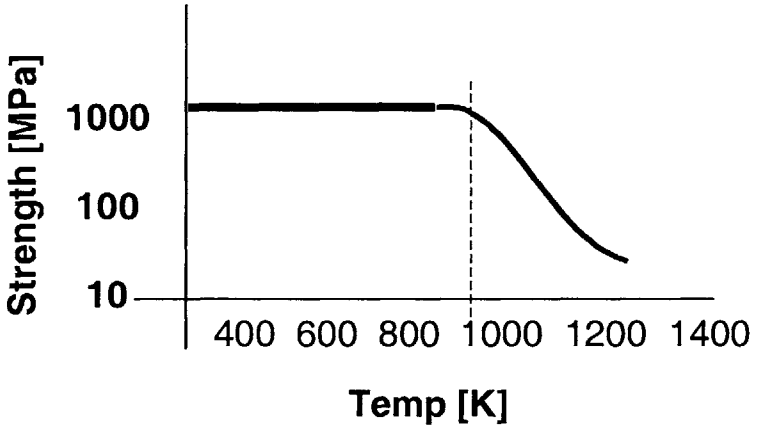

** Courtesy K. Lohner, MIT MS, 1999

Figure 3-7: Silicon strength versus temperature.

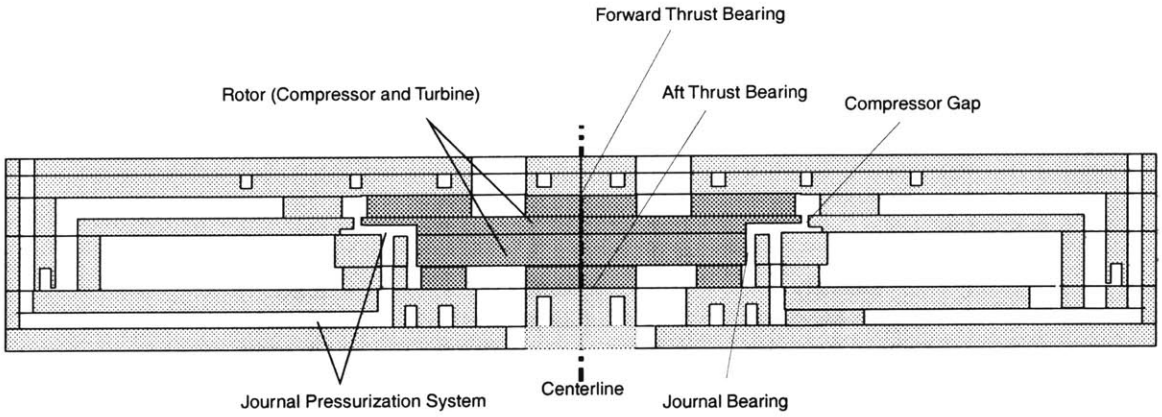

Figure 3-8: Device cross section showing journal pressurization path.

CHAPTER 4

FABRICATION

This chapter discusses the development of the fabrication processes for the initial demo engine test devices. The first portion of this chapter introduces the base of microfabrication capabilities currently available for micro engine development and describes the tight coupling between fabrication capability and design. The second portion of this chapter describes the overall fabrication process used to build the initial test devices. The final portions of this chapter discuss the specific fabrication capabilities that were developed to realize the initial test devices and the new capabilities that must be developed to fully realize the complete design.

This chapter assumes that the reader is familiar with the demo engine geometry described in preceding chapters. It also assumes that the reader is conversant with MEMS microfabrication. Much of the discussion relates to standard processes at MIT. The chapter takes a high-level approach. For specific details on the processes, consult references [51,11]. For general details on MEMS microfabrication, consult [7,22].

The fabrication of the initial demo engine devices represents the cumulative effort of a number of researchers and MIT staff. The process flow described here is original. The process implementation and the development of new process techniques are the work of Arturo Ayon, Ravi Khanna, Xin Zhang, Tom Takacs, and Dennis Ward.

4.1 FABRICATION AND DESIGN

As mentioned in Chapter 2, System Design, the capabilities and constraints of available microfabrication techniques play a fundamental role in determining how a micro engine should be designed.

4.1.1 MICROFABRICATION TECHNOLOGY

Like conventionally scaled gas turbine engines, micro engines are fundamentally limited by the available materials and manufacturing techniques. Gas turbines demand high-strength, low-weight materials that are capable of surviving high temperatures. These demands have driven conventional engine manufacturers to use advanced single-crystal nickel-based superalloys in turbines and lightweight high-strength materials such as titanium alloys in compressors. Yet, although conventional gas turbines use some of the most advanced materials available, their designs are ultimately constrained by manufacturing capabilities. For example, the use of refractory ceramics such as single crystal silicon carbide or single crystal silicon nitride for turbine manufacture could dramatically improve the performance of conventional engines and this has been an area of research for several years. However, in addition to questions of durability, impact resistance, etc., engine manufacturers do not have access to convenient and affordable manufacturing techniques for these materials, preventing their widespread use. Advanced composites have a similar history. Ultimately, like all mechanical systems, engine designs are as constrained as much by manufacturing as by theory or design capability.

The technology base for the manufacture of micro engines is built on the existing technologies of the microelectronics and MEMS fabrication communities. Specifically, single-crystal silicon is the most widely available and convenient material for microfabrication. The semiconductor community requires thin (hundreds of microns) wafers of extremely pure single crystal silicon for the manufacture of high-speed integrated circuits. Tools are available to manufacture wafers, etch wafers, and deposit thin-film coatings of various materials. The MEMS community has built on this technology base, adding the capability to perform deep etches and to bond individual wafers together. For a complete description of MEMS fabrication techniques, consult [7].

The demanding requirements of semiconductor manufacturers make the available silicon wafers a good material for micro engine manufacture. The high strength-to-weight ratio of single crystal silicon makes it well suited to high-speed turbomachinery. In addition, the associated manufacturing base offers a number of benefits including: (1) batch manufacturing, (2) micron tolerances, (3) minimal parts count, and (4) a ready supplier base. The limitation of this base is its strong association with silicon. As with conventional engines, silicon carbide and silicon nitride are preferred materials for micro engine fabrication. However, just as conventional engines are tied to metals, the demo micro engine is tied to silicon by the availability of microfabrication technologies.

4.1.2 Systems Implications of Microfabrication

Chapter 2, System Design, covered the many constraints microfabrication places on the demo engine system design. Etching methods limit the geometry to extruded 2D prismatic shapes. The blade height and journal bearing depths were limited to 225 μm and 300 μm for practical throughput. Mask manufacture and available wafer area limits dies sizes to 2.1 cm square. All of these restraints can change with additional fabrication development effort, but they are of only secondary importance. The two most critical implications of microfabrication on the overall demo engine system are die-level etch uniformity and wafer alignment. These two factors directly control the balance of the spinning rotor and, therefore, the achievable rotational speeds.

4.2 Turbocharger and Demo Engine Fabrication

Chapters 1 and 2 introduced the overall layout of the demo engine. This section describes the final fabrication process developed for the demo engine. Two device types were fabricated: (1) turbochargers and (2) demo engines. As noted in Chapter 2, System Design, both devices are identical except for the fact that the turbine and compressor gas paths are separated in the turbocharger, allowing a separate turbine air supply. The description here presents the turbocharger fabrication process.

The fabrication process is an all-silicon wafer-level MEMS microfabrication process involving six silicon wafers, 19 masks, 17 deep etching steps, 12 oxide film depositions, and three separate

bond/anneal steps. The process uses four 450 μm double-side polished wafers and two 525 μm double-side polished wafers. The bonding surfaces of all wafers are protected at all times with a sacrificial oxide film that is removed only prior to bonding. Total fabrication time from start to finish is approximately six weeks. For a detailed description of MIT's standard microengine-related processing techniques used here, consult the references by Ayon, Khanna, Zhang, Ghodssi, and Schmidt highlighted in Chapter 1, Introduction.

4.2.1 INHERITED FABRICATION TECHNIQUES

The demo engine process relies heavily on fabrication techniques inherited from other MIT devices.

Aligned Double-Side Through-Wafer DRIE Process

The turbocharger and demo engine processes are based on a variation of the aligned double-side through-wafer deep reactive ion etching process described by Lin [51] and also used by Frechette [11]. The basic process flow is:

(1) Photolithography on the front side of the wafer and grow protective oxide film on back side.

(2) First deep silicon etch part-way through wafer.

(3) Photolithography on back side of wafer and protective film on front side.

(4) Attach etched wafer to a handle wafer.

(5) Second deep silicon etch, reaching base of first etch and 'breaking through' wafer.

(6) Removal of handling wafer and surface protection films.

This process can create wafers with plenums and flow channels that are then capped when a second wafer is bonded to the plenum-side of the etched wafer. The process can also create released rotor structures.

Fabrication Rules

The experience gained from the fabrication development efforts of previous microengine-related devices led to a set of inherited rules to follow when designing the demo engine fabrication process. For details on these rules, consult references [29, 51, 11, 13, 15]. The inherited rules are:

(1) Avoid sealed cavities. They cause plastic deformation of the wafer during bond anneal.

(2) Relieve or remove stressed films to avoid wafer bow. Wafer bow impedes bonding.

(3) Apply low pressure during bonding to avoid wafer cracking.

(4) Avoid sharp features. They cause accelerated local etching due to non-uniform elec. fields.

(5) During through etches, protect backside bonding surfaces with a sacrificial oxide layer.

(6) Avoid mixing large and small through etched features. The large features will etch up to three times faster than the small features.

(7) Protect ALL bonding surfaces from start to finish with a sacrificial protective oxide layer. This layer protects the bond surfaces from being etched and also protects against films left after chemical steps.

(8) Measure initial wafer bow for ALL wafers. Wafers with bow cause bonding problems.

(9) Always use a handling wafer on levels with large exposed areas, thin membranes, or fragile features. If the membranes cover a very large area, use thick handling wafers or double-up handle wafers. The handle wafers prevent wafer flex during handling.

4.2.2 Process Challenges

The demo engine is a complex MEMS device. It is similar in many respects to the six-wafer hot static structure described in [11] and the five-wafer micro bearing and micro motor compressor devices described in [51, 11]. However, the demo engine has the following primary characteristics that make it more complicated than these other devices.

(1) A two-wafer rotor. The demo engine is the first MEMS device to include a multiple-wafer rotor designed for high-speed rotation. The rotor is formed by bonding together separate turbine and compressor wafers. The bonded rotor introduces challenges for rotor retention and wafer-to-wafer bond alignment.

(2) Large precision features. The demo engine has larger features than the micro bearing rig and the micro motor compressor. The overall die size is larger (2.1 cm vs. 1.5 cm) to accommodate the combustor. The rotor diameter is larger (8 mm vs. 4 mm) for increased overall mass flow. The blade tip clearances are also larger (20 μm vs. 8 μm). At the same time, the demo engine features require much greater precision than the combustor hot rig of [29] (+/- 0.5-5.0 μm vs. +/- 10-100 μm). The combination of large dimensions and precision features impacts mask design and manufacture, etching methods, wafer handling techniques, and die sawing.

(3) Thermally isolated structures. Like the combustor hot rig of [29], the demo engine has provisions for a thermally isolated combustor. However, unlike the combustor hot rig, the demo engine also has precision structures that are formed during the same etches as the thermal isolation. The presence of the thermal isolation affects the approach to precision etches.

(4) Multiple end-point etches. Like the micro rocket reported in [13] and unlike the devices reported in [51, 11], the demo engine process has several etches with multiple end points. A multiple end point etch defines multiple features, all of which must be complete prior to termination of the etch. Aspect ratio dependent etching and nested masks (described below) compound this problem. The multiple end-points impact recipe selection and etching technique.

4.2.3 GEOMETRY

Figure 4-1 illustrates again the basic demo engine fabrication concept. As the figure shows, the engines are built by bonding a stack of six individually etched silicon wafers. Ten engine 'dies' can fit on one stack of four inch wafers. Each wafer in the stack corresponds to a 'level' of the engine structure. The first and sixth wafers are capping levels that seal the engine flow paths. The third and fourth wafers are rotor levels corresponding to the compressor and turbine respectively. The second and fifth wafers are thrust bearing levels corresponding to the forward and aft thrust bearings respectively. The process steps for the complete wafer stack are essentially symmetric about the center bond line.

From the perspective of fabrication, the demo engine has six important geometric features. They are identified in Figure 4-2. The first important feature is a two-wafer rotor consisting of a

compressor and a turbine, each made up of blades and a disk and separated from the non-rotating (static) structure by the second important geometric feature, a 6 mm diameter, 10 μm wide, 300 μm deep journal bearing. The third important feature is an empty combustor volume cut out of the static structure of the turbine wafer. The fourth is an empty 'cooling jacket' channel that separates the combustor structure from the outer structure of the die. The cooling jacket is crossed by 100 μm 'bridges' that connect the combustor structure to the rest of the die. The fifth and sixth important features are the forward and aft thrust bearings, 'micron-sized' gaps that separate rotor from the static structure above and below it. These features are described in functional detail in Chapter 4, Component Design.

4.2.4 ETCHES

The mechanical features of the demo engine are 'bulk micromachined' by etching blank silicon wafers. The fabrication process involves two etch types. Deep etches are 10-1000 μm deep and define 'vertical' features such as journal bearings and blades. Shallow etches, are 1-20 μm deep and define 'horizontal' features such as thrust bearing running gaps and tip clearances. In contrast to the devices of [51] and [11] all etches for the demo engine and turbocharger, including the shallow etches, were performed in MIT's two Surface Technology Systems time-multiplexed deep reactive ion etching (DRIE) plasma etching tools. The etches were developed by Ayon, Khanna, Zhang *et al.* For additional details consult references [2,15,16].

4.2.5 PROCESS FLOW

Figure 4-10 illustrates the fabrication process flow. The process starts with the forward thrust bearing wafer. This wafer is etched with a front side deep etch that defines pressure taps and fuel plenums, a back side deep etch that defines the thrust bearing restrictors, and a back side shallow etch that defines the blade tip clearance. The tip clearance etch is implemented with a nested mask.

The compressor wafer is the second wafer in the process. This wafer is coated on the front with a bondable 1.5 μm thermal oxide that is used for rotor retention. The wafer is etched on the back side to define the compressor running gap and on the front side to define the blades. The

compressor running gap etch is left partially incomplete, leaving a thin (50 μm) membrane of silicon that retains the rotor. Then, the forward thrust bearing wafer is bonded to compressor wafer through the bondable thermal oxide. After the compressor and forward thrust bearing wafers are bonded, the compressor back side etch is continued with a nested mask, freeing the rotor. This second etch also recesses the compressor disk to prevent unintended bonding in the future. The final result of this stage of processing is a bonded pair of wafers with a fully defined compressor rotor retained by a sacrificial oxide film sandwiched between the compressor and forward thrust bearing.

The turbine wafer is the third wafer in the demo engine process. The process starts with a shallow etch on the back side that defines part of the thrust bearing gap. Then, like the compressor wafer, this wafer is etched with a journal bearing etch and then a blade etch. The combustor is also defined by these two etches. The blade etch is only partially completed, retaining the turbine with a thin film. The turbine is then bonded to the compressor/forward thrust bearing wafer pair. The blade etch is completed, and the final result is a three wafer bonded stack with an open combustor and a fully defined rotating spool (compressor plus turbine) retained to the forward thrust bearing through a sacrificial oxide film. This three-wafer stack contains all of the principal components of the engine.

The three core wafers (compressor, turbine, and forward thrust bearing) of the demo engine wafer stack required sequential processing and bonding steps to create a retained rotor. The remaining three wafers are only bonded together during the final bond step. They are processed independently. The forward and aft 'capping' wafers each require only one deep etch. The aft cap has the features for the engine exhaust nozzle. The forward cap has the geometry for the inlet and fluidic interconnect ports. These wafers are etched through from the inside (bonding surface) out. This protects the geometry at the bond interface from reentrant etch effects. The aft cap is also patterned on the back side with a shallow etch for die saw alignment. This is necessary because the dies are closely spaced and may be cut open without precision alignment. The aft thrust bearing wafer is nearly identical to the forward thrust bearing wafer except for the addition of a shallow etch that defines the thrust bearing gap.

Once all six wafers are complete and the three-wafer stack (compressor, turbine, forward thrust bearing) is bonded, all remaining protective oxides are stripped, and the complete set of wafers is

bonded and annealed to form a six-wafer demo engine stack. The completed stack is then cut into individual engines (dies). At this stage, there are 10 individual engines, each complete with a combustor and a retained compressor/turbine rotor spool. The rotors are released by etching the sacrificial retention oxide at the die level with hydroflouric acid. After release, the dies are ready for cold packaging with o-rings or hot packaging with Kovar/glass interconnects.

4.3 Process Issues and Development

Like the other microengine-related devices built thus far, the demo engine required the use special processing techniques not described in common MEMS references such as [7]. Some of these techniques were inherited from previous microengine devices [29,13,11,51]. Others were developed specifically for the demo engine process. This section details important processing issues and special techniques developed for the demo engine.

4.3.1 Wafer Alignment and Bonding

The demo engine requires precision front-to-back etch mask alignment and precision bond alignment. Misalignment in the compressor or turbine wafers leads to rotor imbalance. Misalignment between the blade etch and the journal bearing etch offsets the blades relative to the geometric center of the rotor. Misalignment of the compressor and turbine during bonding offsets the rotor's center of gravity from the journal bearing geometric center. The imbalance percentage of a rotor is the ratio of this offset to the journal bearing gap.

Calculations by Jacobson show that sequential random misalignments as small as +/- 2 μm introduces a cumulative 50% imbalance level in demo engine rotor. Experimental results from MIT's micro bearing rig suggest that the demo engine will require an imbalance level of less than 5% to achieve full operating speed of 1.2 million RPM [20]. Assuming a root-mean-square addition of misalignments, this requires an alignment accuracy of +/- 0.5 μm for all alignment steps.

The achievable level of mask alignment accuracy depends on the quality of the mask alignment tool. Steppers can achieve front-to-front mask alignments of +/- 0.25 μm. The Electronic

Visions (EV) 'contact aligner' used for the demo engine mask alignment is capable of front-to-front alignment within +/- 0.5 μm and front-to-back alignment within +/- 1 μm. The Electronic Visions 'aligner bonder' tool used for wafer bonding has an alignment accuracy of +/- 2 μm. For the demo engine devices described in this thesis, global mask alignment was measured to be within +/- 2.0 μm using an EV TBM-8 alignment measuring tool with +/- 0.5 μm measurement accuracy. Bond alignment was measured to be within +/- 5 μm using the same tool.

As shown in Chapter 6, experimental results, the mask and wafer alignment levels achieved in the build presented here are insufficient to fabricate a balanced demo engine rotor that can reach full design speed. MIT is continuing efforts to improve alignment. The target alignment accuracy for both front-to-front and front-to-back mask alignment is +/- 0.5 μm. The target alignment accuracy for wafer bonding is also +/- 0.5 μm. This would lead to a rotor imbalance of 5%.

4.3.2 Uniformity[7]

Turbocharger wafers etched in the plasma of the STS etcher show a non-uniformity of etch depth across the wafer. This is the consequence of a non-uniform etch rate across the wafer. The etch non-uniformity is recipe and mask dependent, but a typical etch varies in depth by +/- 10% across the wafer and can vary by up to 15 μm across the rotor of a single die. The hypothesized cause of this non-uniformity is localized accumulation of reaction products. When the dies are densely packed (e.g. ten demo engine dies per wafer), the large exposed etch area limits diffusion of the products, increasing non-uniformity. With low die density (e.g. four demo engine dies per wafer), the uniformity is improved. MIT is continuing efforts to develop more uniform etches.

4.3.3 Rotor Retention[8]

The demo engine contains a freely rotating rotor for the turbomachinery. Fabrication of free-moving parts is a traditional MEMS problem. In a bulk micromachined device like the demo

---

[7] Research into etch non-uniformity is the work of A. Ayon, X. Zhang, R. Khanna, T. Tacaks, and D. Ward.

[8] The processes and geometry for the rotor retention schemes were initially designed by the author. R. Khanna and X. Zhang conducted the experimental development of the 'tab' rotor retention process. R. Khanna and T. Takacs conducted the experimental development of the 'oxide release' rotor retention process.

engine, the free parts will fall out of the wafer upon completion of etching if they are not retained. Once the parts have fallen out, it is extremely difficult to handle the pieces and to clean them sufficiently prior to wafer bonding. Furthermore, in the case of the demo engine, the rotor is made from two pieces. If these pieces fall out prior to wafer bonding, they cannot be accurately aligned for bonding.

A number of techniques have been used to address the issue of rotor retention. These techniques are illustrated in Figure 4-11. MIT's original microengine design called for a sacrificial release film [6]. C. C. Lin used laser-release (LAE) tabs to retain his micro bearing rig rotors [51]. L. Frechette used mechanical break-off tabs [11]. Both tab schemes involve bonding the free part (rotor) to the static structure of another wafer through a sacrificial mechanical structure. The primary benefit of the tab approach is the lack of any chemical steps that could damage thin-film electrical components in the device. The disadvantage of the tab approach is that it is a serial process. Release, in particular, must be performed on a die-by-die basis.

The demo engine process was originally envisioned as a parallel wafer process. In a purely parallel process, each wafer is processed entirely independently of the other wafers in the stack. All six wafers are then bonded simultaneously to create a device stack. An attempt was made to apply the tab concept to a parallel wafer demo engine process by using intra-wafer "cross-journal" tabs. This development is described in the appendixes. The 'cross-journal' tab approach was abandoned due to processing difficulties. This approach should not be confused with the cross-bond approach successfully used by Frechette [11].

The tab approach was replaced with the sacrificial oxide process described in preceding sections. With this approach, the rotor is retained by bonding it to the forward thrust bearing. The bond is made through a thin (0.5 μm) layer of thermal oxide that is patterned to locally accelerate etching. After the demo engine is completely fabricated, the oxide layer is dissolved in 1:1 HF etchant. Figure 4-13 shows a compressor wafer with sacrificial oxide prior to bonding. Figure 4-12 shows the oxide film of a bonded and cross-sectioned wafer pair. The oxide-to-silicon bond is very strong. The only rotors lost during fabrication were due to failure of the supporting silicon structures.

Like the tab retention schemes of MIT's micro bearing rig [51] and micro motor compressor [11], the sacrificial oxide process is a serial process. The forward thrust bearing and compressor are bonded before the compressor gap etch is completed. The primary benefit of the sacrificial oxide approach is the ease of release. Dies can be released one-by-one or in batches. In addition, the sacrificial oxide approach leaves no residual cracks that might lead imbalance or structural failure at speed. The disadvantage of the oxide release scheme is that it is not necessarily compatible with the electrical devices currently used by other MIT micro-engine related devices [11, 55]. During release, the 1:1 HF also attacks the insulating oxide used in the motor. This problem may be addressed by protecting the rotor films with a layer of nitride or by using an alternative sacrificial film.

4.3.4 NESTED MASK ETCHES[9]

As mentioned above, some of the clearances in the demo engine are too deep to allow re-coating of resist for multiple etches. The photoresist does not uniformly coat the edges of the deep etches, leading to undesired masking that causes irregular etch features.

In such a situation, a nested mask must be used. Nested masks allow multiple deep etches on the same side of a wafer by using two dissimilar masking materials nested on each other. The demo engine used the two-level oxide/photoresist nested mask process illustrated in Figure 4-14. Simultaneous with this effort, London developed a similar nested mask process for the microrocket [13]. Ayon also developed a teflon/oxide/photoresist triple nested mask process described in [10].

Nested masks require optimization of the oxide thickness. The oxide mask must be thick enough to survive the second etch without failing. At the same time, thicker oxides require longer depositions times, cause wafer bow, and require longer BOE oxide etch times for stripping. If a BOE oxide etch is used to define the oxide, the mask features will grow in size by the thickness of the oxide because the oxide etches isotropically.

---

[9] The demo engine nested mask process was designed by the author and initially implemented by A. A. Ayon, R. Khanna, and T. Takacs.

4.3.5 MULTIPLE END POINT ETCHES AND ASPECT-RATIO DEPENDENT ETCHING

A multiple end-point etch defines multiple features, all of which must be complete prior to termination of the etch. The demo engine has two multiple end-point etches. The first is the turbine blade etch. This etch has a large-area (~1-10 mm diameter) feature for the blades and combustor and small area features (~300 μm diameter) for through-wafer fluidic interconnects. The first endpoint occurs when the open blade area reaches the journal bearing. The second endpoint occurs when the through-wafer fluid interconnects reach corresponding features on the back. All of the halos are at the same depth. However, etch rate during the blade etch depends on feature size, a phenomenon known as aspect-ratio dependent etching. Larger features etch faster. Depending on etch recipe, the second endpoint can lag the first by as much as 50 μm on a 200 μm deep etch. Figure 4-15 illustrates the etch rate versus feature size for several different etch formulations in MIT's STS etcher [2]. The demo engine process solved the multiple end-point etch problem by using 'MIT-37', a limited aspect-ratio dependent etch illustrated in Figure 4-15. Unfortunately, this formulation sacrifices side wall quality and gives poor fillets at blade roots. It is suggested that future devices incorporate mask changes to address the multiple end-point problem. For additional details on aspect ratio dependent etching, consult Ayon's reference [2].

The second multiple end-point etch is a nested-mask etch, the compressor backside clearance etch. This etch simultaneously defines an oxide-mask large-area plenum and continues the photoresist-mask compressor gap. The two endpoints are (1) compressor clearance gap break-through and (2) a compressor backside clearance of 50 μm. If the first endpoint is not achieved simultaneously with or before the second endpoint, the compressor disk will be thinned. In the worst case, the disk may be etched away completely. Aspect ratio dependent etching causes the second, large-area etch to "catch up" with the initial narrow trench etch. Consequently, the second endpoint is difficult to achieve simultaneously with the first and the clearance ends up in the range of 50-120 μm. The solution again is to use an etch such as MIT-37 that has little aspect ratio dependence.

4.3.6 THERMALLY ISOLATED STRUCTURES[10]

Like the microcombustor device reported in [29], the demo engine process has thermally isolated features. Thermal isolation occurs when a feature is separated from the bulk of the wafer by small structures. In the case of the demo engine, the combustor is thermally isolated from the wafer by a 'cooling jacket' with small bridges. If thermally isolated features become hot during an etch, the chemical etching properties will change locally. Symptoms include resist drying, accelerated etching, and loss of anisotropy.

The etcher keeps wafers cool by flowing Helium across the back surface of the wafer. When the wafer has through features, it must be mounted to a handle wafer to prevent the Helium from leaking into the etch chamber. The cooling flow keeps the handle wafer cool and, by extension, any portions of the etch wafer that are in intimate thermal contact with the handle wafer. Provided the etch has not cleared through the wafer, a thermal path exists between the handle wafer and every portion of the etch wafer. However, problems arise once the etch clears through the wafer. Suspended features no longer have a direct thermal path to the wafer. Instead, they are separated from the bulk of the wafer by the thermally resistant small structures.

The chemical steps of the deep etching process are thermally activated processes governed by an Arhennius rate equation. It is hypothesized that when thermally isolated structures become hot, the chemical etching accelerates. Side-wall etching, in particular, is an almost purely chemical etch process (it is not influenced by ion bombardment). Figure 4-16 shows accelerated etching of combustor cooling jacket side walls. The etch also becomes more isotropic, causing feature blow out and loss of side-wall control.

There are two solutions to the thermal isolation problem. The first is to stop the etch exactly when the thermal isolation becomes defined by etch break-through. The combustor hot rigs of [29] were processed this way. The demo engine cannot use this approach because the cooling jacket etches also have other end points (e.g. journal breakthrough). This led to a second approach: ensure that all features contact the handle wafer. The previous standard MIT process

---

[10] The thermal isolation mechanism explaining loss of etch quality was initially hypothesized by the author. Experimental evidence of the mechanism was initially observed by R. Khanna.

for mounting handle wafers, photoresist 'ring mount,' only contacts the wafer edges. Consequently, the isolated features of individual die do not have a thermal path to the handle wafer. As part of the demo engine process, R. Khanna developed a new "target mount" approach. The target mount uses concentric rings of resist. The concentric rings ensure that all features have a direct connection to the handle wafer through the resist. Figure 4-17 illustrates the two approaches.

4.3.7 Etch Uniformity Control with Through Etches[11]

The uniformity of an etch plays an important role when wafers are etched on both sides, as they are for the demo engine. During a non-uniform through-etch, the through features on each die will break through at a different time. In the case of the demo engine process, etching is faster near the edges of the wafer, so the outer dies break first. The inner dies etch slowly and may break as much as 30 min later. High aspect ratio etches tend to be much more uniform than large-area etches. The non-uniform break through allows the plasma to etch the features on the obverse side of the outer dies. Non-uniformity is especially a problem for etches with multiple end-points or sensitivity to over-etching (e.g. thrust bearing nozzle etches, tab etches, nested mask etches).

Non-uniformity during through etches is a coarse wafer-level problem and can be addressed using a coarse, wafer-level solution. The demo engine process uses die patching, a procedure developed by Khanna and Tackas. As a select target feature on each die reaches its target depth, that die is patched with photoresist to prevent continued etching. Etching continues until all dies are at target depth, allowing the slower etching regions to "catch up" with the faster regions. The result is a wafer with dies that may have local non-uniformity, but that all have the same average depth. This approach does not address the die-level non-uniformity responsible for rotor imbalance. Die-level non-uniformity depends on wafer layout and on the specific chemical formulation of the etch.

---

[11] The 'bulk' methods for controlling etch uniformity were developed by A. Ayon, R. Khanna, and T. Takacs. Custom recipes to reduce etch non-uniformity were developed by X. Zhang and A. Ayon.

4.3.8 ADVANCED GEOMETRIES

The 'baseline demo engine' was originally designed with a more advanced geometry than the 'fabricated demo engine' described in this chapter. The baseline demo engine design called for 400 μm (versus 225 μm) tall blades for a higher engine mass flow and a 500 μm deep journal bearing (versus 300 μm) for better bearing stability. This led to a 700 μm (versus 525 μm) thick compressor wafer and a 900 μm (versus 525 μm) thick turbine wafer. The baseline design also called for 20-50 μm fillets at the base of the turbine and compressor blades to guarantee structural integrity at the 1.2 million RPM design speed. Although not implemented in the demo engine builds presented here, processes were partially developed for these advanced geometries.

500 μm Deep Journal Bearings[12]

Like the micro bearing rig of [51], the demo engine journal bearing is a simple circular gap that may operate as a hydrostatic or hydrodynamic gas bearing. Improved journal bearing processes are an ongoing goal of the demo engine development program. In particular, longer journal bearings (deeper etches) offer better bearing performance. As described in Chapter 3, Component Design, the stability of a hydrodynamic bearing increases with length. In addition, the deeper the journal, the thicker the rotor disk. Because the rotor disk is the 'balanced' mass, a rotor with a deeper journal has a lower level of imbalance.

The demo engine was initially designed for a 500 μm deep journal bearing. Previous micro-engine related devices have only used 300 μm journal bearings [51,11]. At 300 μm deep and 12 μm wide with only +/- 0.5 μm width variation, these bearings are near the current limits for a photoresist-based deep trench etching process. Deeper journal bearings require a new hard-mask process. As part of demo engine development, Ayon, Zhang, and Khanna developed a new hard-mask, 500 μm deep, journal bearing etch. By tailoring the etching parameters, they were able to etch a 16 μm wide, 500 μm deep journal with a width variation of +/- 4 μm. Figure 4-18 compares the current state-of-the-art 500 μm journal etch to the state-of-the-art 300 μm etch.

---

[12] A. Ayon and R. Khanna developed the 500 um journal bearing etch. A. Ayon and X. Zhang developed the 300 um journal bearing etch.

To date, development time for the 500 μm journal etch has totaled 6 months. While clearly superior to previous 500 μm etches, the current state-of-the-art 500 μm etch does not deliver the +/- 1 μm width tolerance of the 300 μm etch. Computations show that for stable hydrodynamic operation, the journal bearing requires a tolerance of +/- 1 [20]. The 500 μm etch has two additional drawbacks. First, at 8 hrs total etch time, it takes more than twice as long as a 300 μm journal etch. Second, the oxide mask is difficult to remove. To survive the 8 hour etch, the oxide mask must be at least 8 μm thick. By the end of the etch, the exposed regions of the mask will be less than 1 μm thick. After etching, these regions can be stripped with BOE in as little as 30 minutes. However, due to the geometry of the STS etcher, portions of the wafer are covered during etching. These portions remain 8 μm thick and require as much as 3 hrs of BOE etching. The result is a long BOE over-etch of the silicon bonding surface. Such a long BOE etch can make the wafer unbondable, causing poor yield.

400 μm Tall Blades[13]

The demo engine was initially designed for an engine mass flow of 0.36 g/sec. To achieve this mass flow, blade height was doubled to 400 μm from the 200 μm used on previous microengine-related devices. Figure 4-19 illustrates a 400 μm compressor blade etch. The blade heights for the initial demo engine builds were switched to 225 μm because the 225 μm process is well established. The transition to 400 μm blades proved straightforward in MIT's STS-1 etcher. 400 μm blades could not be etched in on a 4-inch wafer in MIT's STS-2 deep etcher due to resist failure. The problem appears to be associated with mounting 4-inch wafers to a 6-inch handle wafer.

Blade Fillet Radius[14]

As detailed in Chapter 4, Component Design, the demo engine requires fillets at the blade roots for structural survivability during full-speed operation. Calculations by Chen showed that fillets in the range of 20-40 μm were needed [17]. Etch parameters were studied to determine a suitable recipe to generate the fillets [11]. The study showed that fillet radius increases with etching

---

[13] A. Ayon first demonstrated 400 um blades.

[14] A. Ayon and T. Takacs developed the demo engine blade etches with fillet radii.

chamber pressure. However, surface quality decreases with etching chamber pressure. The strength of the resulting fillet is a trade-off between global geometry (fillet radius) and local geometry (surface quality). Unfortunately, the fillet could not be included in the initial demo engine builds because the fillet etch has poor aspect-ratio dependence. Future builds will include a modified mask geometry to accommodate the aspect-ratio dependence. As mentioned above, multiple end-points forced the turbine etch to use a special non-aspect ratio dependent etch formulation (MIT-37).

4.4 Lessons Learned and Conclusion

Although resembling previous rotating and non-rotating microengine-related devices, the demo engine has more stringent fabrication requirements and required considerable additional process development. The two-wafer rotor complicates rotor retention/release and makes alignment a critical issue. Rotor imbalance and the mixture of large and small features make etch uniformity an issue. The simultaneous presence of a combustor and a precision rotor combines the problems of thermal isolation and multiple-end-point etches. Deeper etches required the use of nested masks for the first time in a MEMS turbomachine. Thus, the conceptually simple process of marrying the combustor to a rotating spool proved to be a formidable microfabrication challenge. Advanced features such as 400 μm blades and 500 μm journals, as desirable as they may be from a design perspective, greatly aggravate this already difficult development task. Ultimately, the demo engine fabrication process had to be driven as close as possible to the already developed micro bearing process of [51] simply to get a device to test.

4.5 References

[1] C. C. Lin, *Development of a Microfabricated Turbine-Driven Air Bearing Rig.* PhD thesis, MIT, Department of Mechanical Engineering, 1999.

[2] A. A. Ayon, R. Braff, C. C. Lin, H. H. Sawin, and M. A. Schmidt, "Characterization of a Time Multiplexed Inductively Coupled Plasma Etcher," *Journal of the Electrochemical Society*, Vol. 146, No. 1, Jan. 1999.

[3] A. Mehra, Development of a High Power Density Combustion System for a Silicon Micro Gas Turbine Engine, PhD thesis, MIT, Department of Aeronautics and Astronautics, 2000.

[4] A. P. London, *Development and Test of a Microfabricated Bi-Propellant Rocket Engine*, PhD Thesis, MIT, Department of Aeronautics and Astronautics, 2000.

[5] B. Miller, Personal communication, 1998.

[6] G. K. Ananthasuresh, Personal communication, 1997.

[7] N. Maluf, *An Introduction to Microelectromechanical Systems Engineering*, Boston, Massachusetts: Artech House, 2000.

[8] R. L. Bayt, *Analysis, Fabrication, and Testing of a MEMS-Based Micropropulsion System*, PhD Thesis, MIT, Department of Aeronautics and Astronautics, 1999.

[9] L. Frechette, *Development of a Silicon Microfabricated Motor-Driven Compressor*, PhD Thesis, MIT, Department of Aeronautics and Astronautics, 2000.

[10] A. A. Ayon, D. Z. Chen, R. A. Braff, R. Khanna, H. H. Sawin and M. A. Schmidt, "A Novel Integrated Process Using Flourocarbon Films Deposited with a Deep Reactive Ion Etcher," presented at the Fall Meeting of the Materials Research Society, Boston, MA, Nov. 29 – Dec. 3, 1999.

[11] K. S. Chen, A. A. Ayon, K. A. Lohner, M. A. Kepets, T. K. Melconian, S. M. Spearing, "Dependence of Silicon Fracture Strength and Surface Morphology on Deep Reactive Ion Etching Parameters," presented at the MRS Fall Meeting, Boston, MA, Dec. 1998.

[12] A. H. Epstein et. al. "Power MEMS and Microengines," presented at IEEE Conference on solid State Sensors and Actuators, chicago, IL, Jun. 1997.

[13] A. A. Ayon, S. Nagle, L. Frechette, R. Ghoddsi, A. H. Epstein, M. A. Schmidt, "Tailoring Etch Directionality in a Deep Reactive ion Etching Tool," presented at Transducers '99, Sendai, Japan, Jun. 1999.

[14] A. Mehra, A. A. Ayon, I. A. Waitz, M. A. Schmidt, "Microfabrication of High Temperature Silicon Devices Using Wafer Bonding and Deep Reactive Ion Etching," IEEE/ASME Journal of Microelectromechanical Systems, Jun. 1999.

[15] A. A. Ayon, R. Bayt, R. Braff, C. C. Lin, H. H. Sawin, M. A. Schmidt, "Etching Characteristics and Profile Control in a Time Multiplexed Inductively Coupled Plasma Etcher," Technical Digest, Solid-State Sensor and Actuator Workshop, Hilton Head, SC, Jun. 8-11, 1998, pp. 41-44.

[16] A. A. Ayón, X. Zhang and R. Khanna. "Ultra Deep Anisotropic Silicon Trenches Using Deep Reactive Ion Etching (DRIE)," to be presented at the Hilton Head need details.

[17] K. S. Chen, *Materials Characterization and Structural Design of Ceramic Micro Turbomachinery*, PhD Thesis, MIT, Department of Aeronautics and Astronautics, 1999.

[18] T. Harrison, MS Thesis, MIT, Department of Aeronautics and Astronautics, 2000.

[19] E. S. Piekos, *Numerical Simulation of Gas-Lubricated Journal Bearings for Microfabricated Machines.* PhD thesis, MIT, Department of Aeronautics and Astronautics, 1999.

[20] S. A. Jacobson, Personal communication, 2000.

[21] S. Nagle, *Analysis, Design, and Fabrication of an Electric Induction Micromotor for a Micro Gas-Turbine Generator*, PhD Thesis, MIT, Department of Electrical Engineering and Computer Science, 2000.

[22] M. Madou, *Microfabrication*

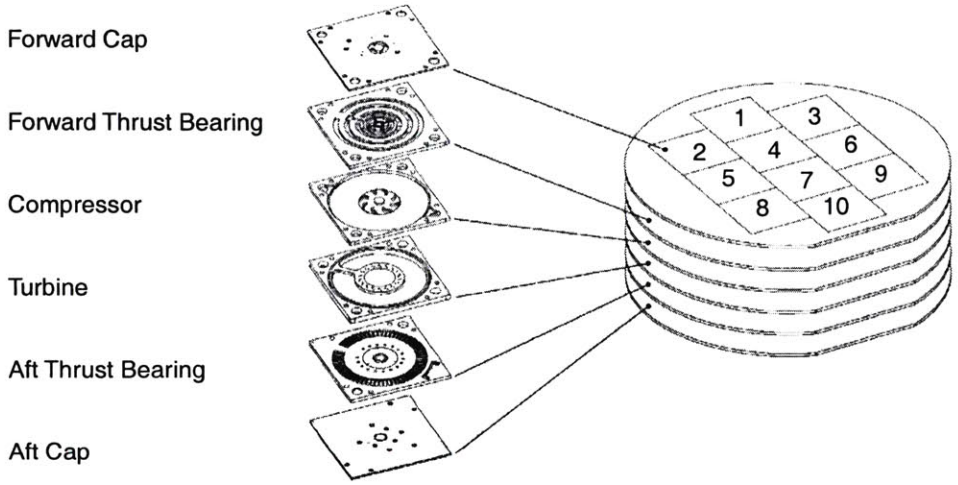

Figure 4-1: Illustration of demo engine processing concept.

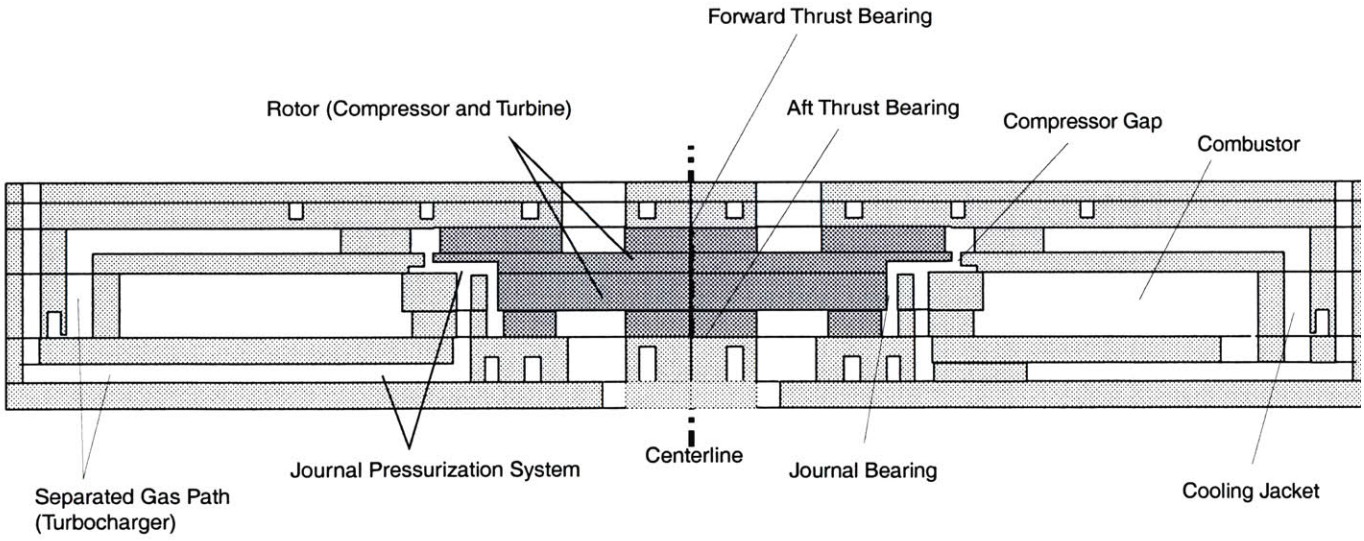

Figure 4-2: Important geometric features of the demo engine.

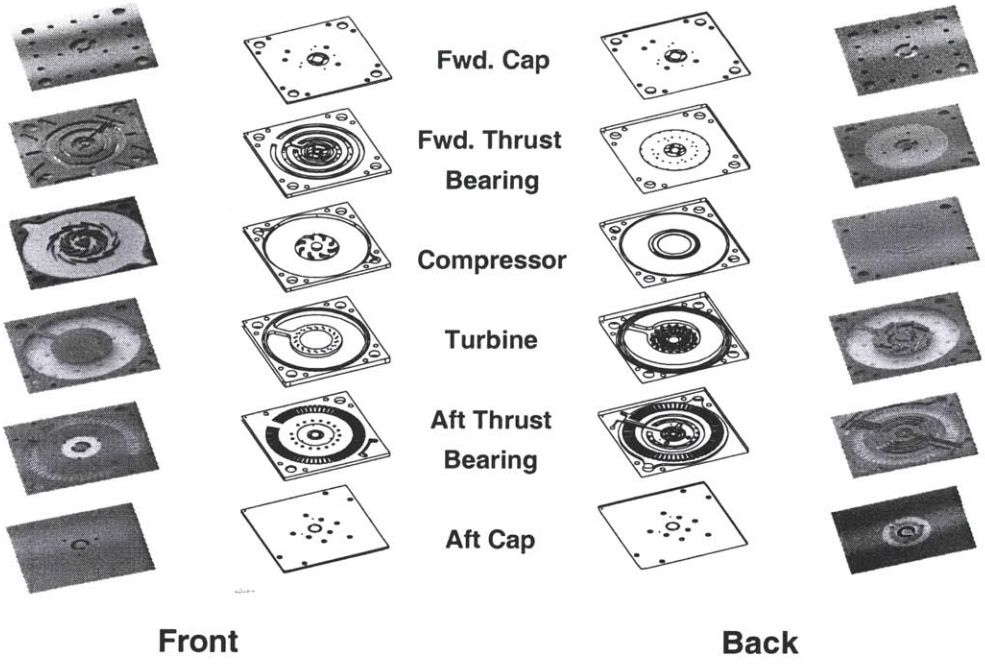

Figure 4-3: Exploded view of six-wafer demo engine/turbocharger die.

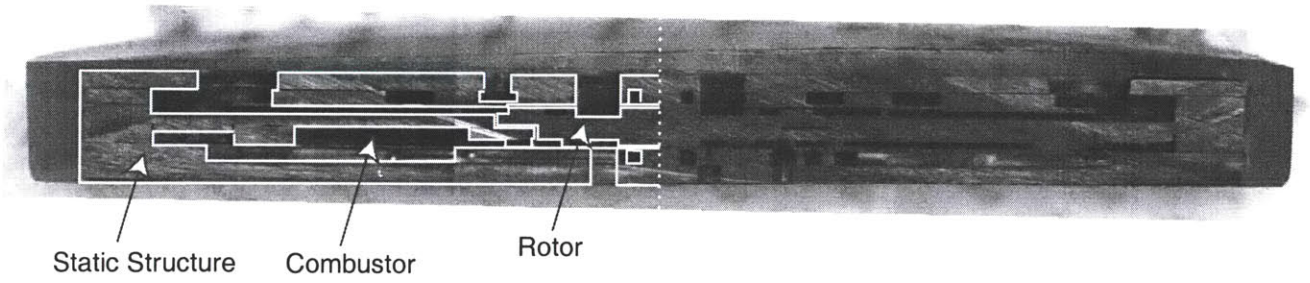

Optical micrograph of a complete cross-sectioned turbocharger die. The die is potted in epoxy.

Figure 4-4: Cross-sectioned die.

Figure 4-5:Wafer-level image of turbocharger compressor wafer.

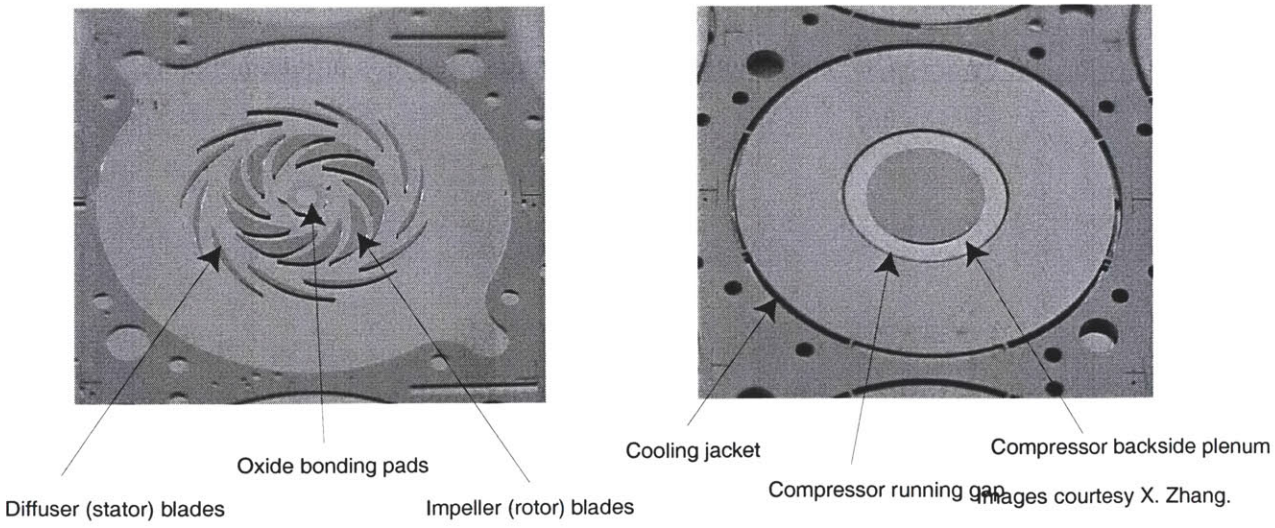

Figure 4-6:Die-level images of demo engine compressor wafers.

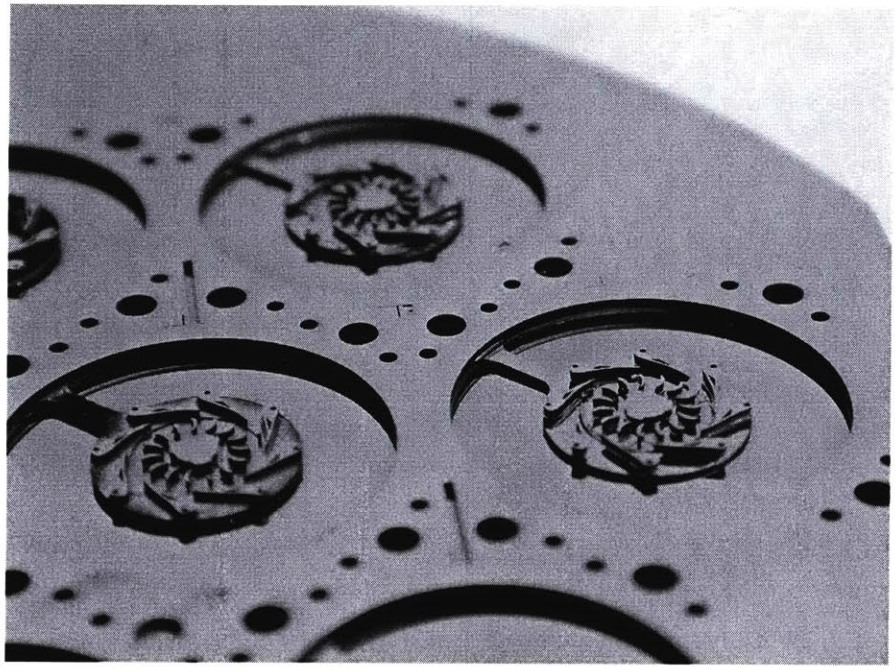

Figure 4-7: Wafer-level image of turbocharger turbines and combustors.

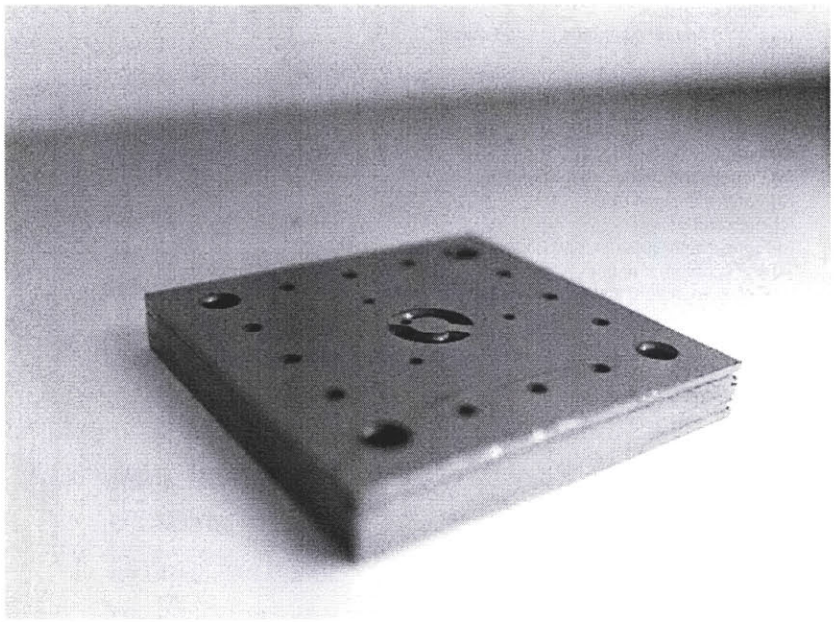

Figure 4-8: Bonded and die-sawed turbocharger die.

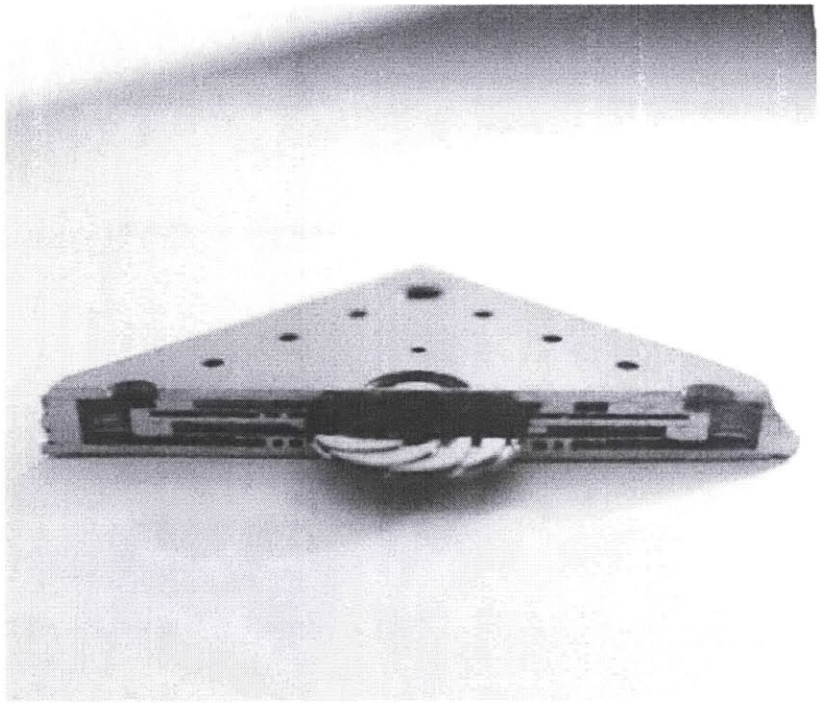

Figure 4-9: Cross-sectioned die showing rotor and static structure.

Forward thrust bearing wafer
(a) Etch plenum.
(b) Etch restrictors
(c) Etch blade tip clearance [nested mask]

Compressor wafer
(a) Deposit thermal oxide for bonding.
(b) Pattern thermal oxide.
(c) Etch blades
(d) Bond compressor to forward thrust bearing.
(e) Etch compressor gap.
(f) Etch compressor disk clearance [nested mask].

Turbine wafer.
(a) Etch journal bearing.
(b) Etch thrust bearing clearance.
(b) Bond turbine to compressor.
(c) Etch blades.

Aft thrust bearing wafer
(a) Etch plenum
(b) Etch restrictors
(c) Etch blade tip clearance [nested mask]

Forward capping wafer
(a) Etch inlet and fluidic interconnects.

Aft capping wafer
(a) Etch die saw marks
(b) Etch exhaust nozzle and fluidic interconnects

Assembly
(a) Bond 2/3/4 to 1, 5, and 6
(b) Release rotor with 1:1 HF etch

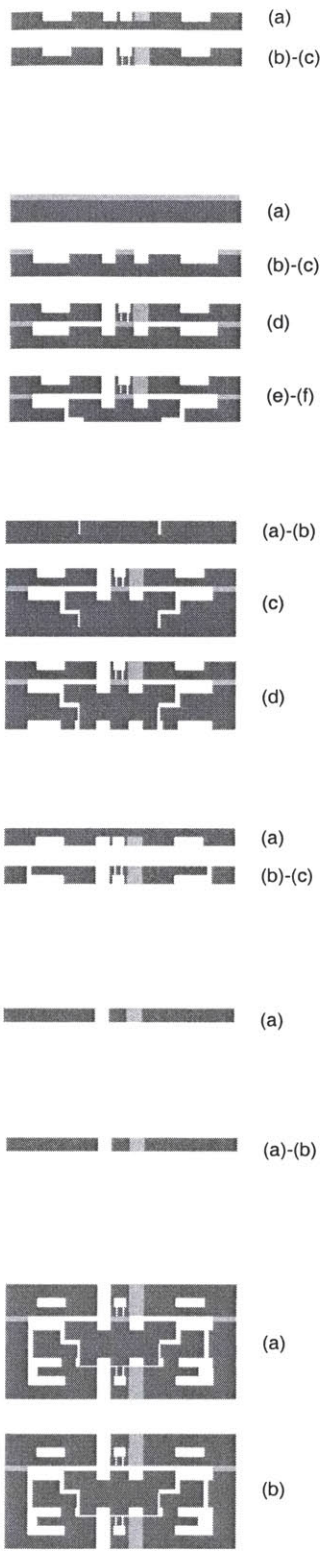

Figure 4-10: Demo engine fabrication process flow.

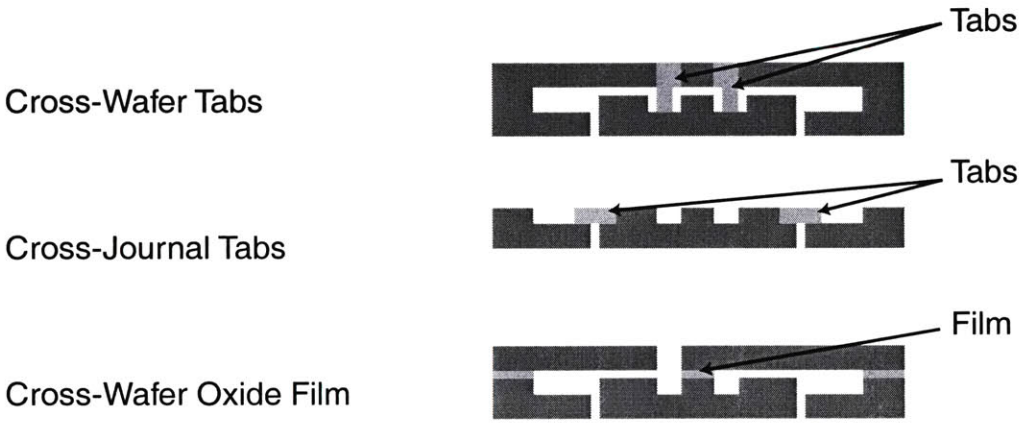

Figure 4-11: Schemes for rotor retention.

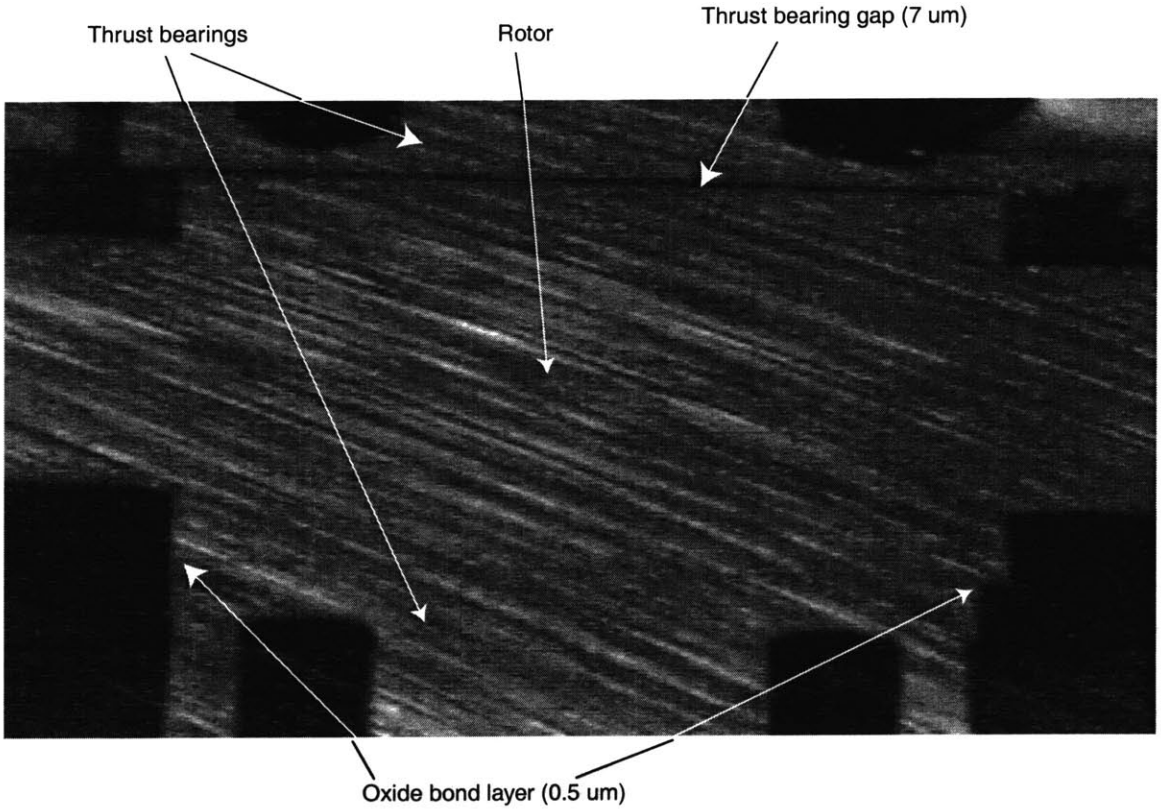

Figure 4-12:Cross-section of rotor hub showing thrust bearing gap and bonded oxide film

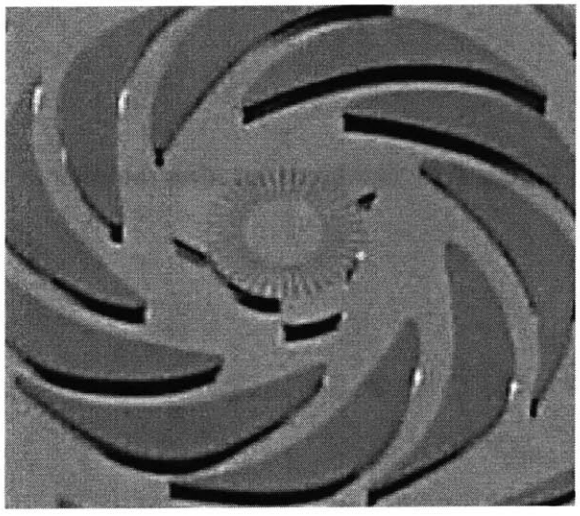

Figure 4-13: Close-up image of compressor wafer showing oxide bond pads on center hub

Deposit oxide.

Pattern and etch oxide.

Coat with resist.

Pattern resist.

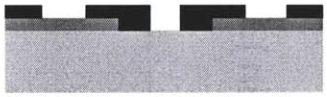

Transfer resist pattern to oxide with BOE etch.

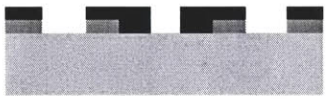

Etch silicon with resist as mask.

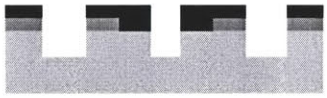

Strip resist.

Etch silicon with oxide as mask.

Process complete.

Figure 4-14: Nested mask process.

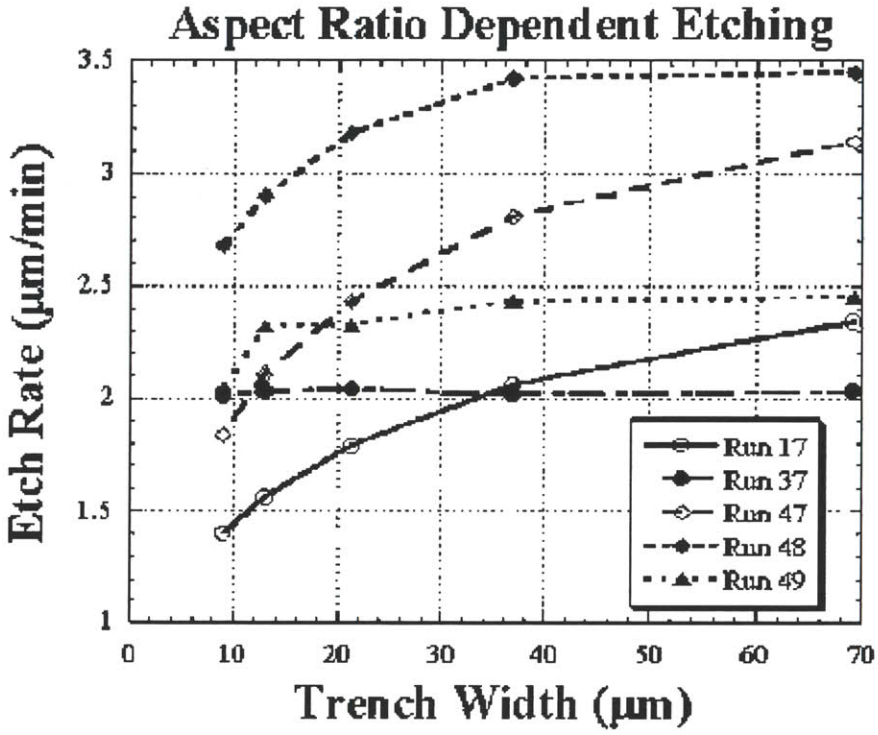

Image courtesy A. Ayon.

Figure 4-15: Aspect-ratio dependent etching from Ayon *et al.*

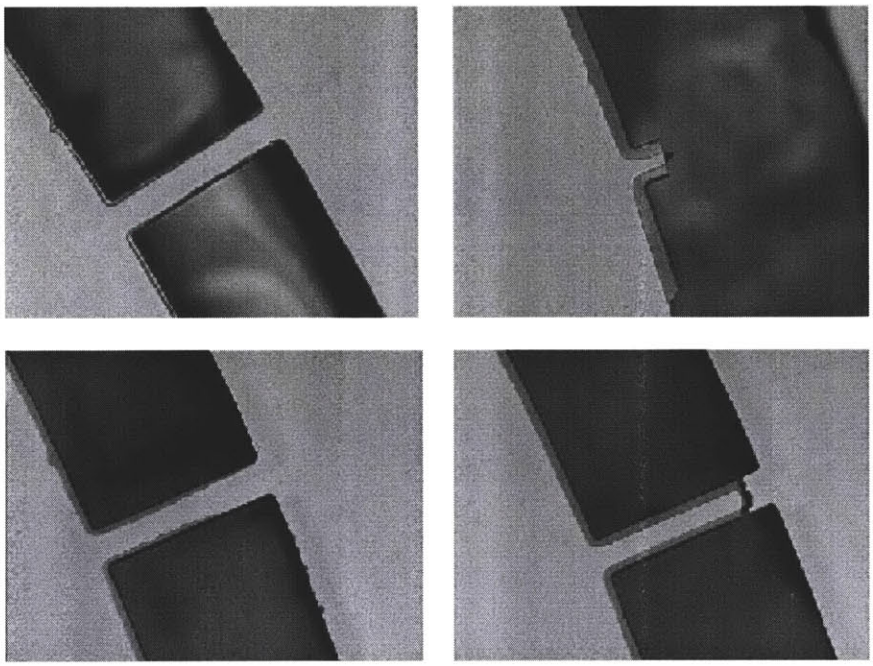

Clockwise from top left: (1) A normal bridge showing no damage. Etched using a 'target' mount. (2) A broken bridge showing accelerated etching of the isolated structure. The dark gray 'border' surrounding the feature is the oxide mask. The etch clearly undercuts the mask. (3) A cracked bridge showing clearly the difference between the etch of the isolated structure and the base structure. (4) A gradiated bridge that shows accelerated etching following a thermal gradient. Light grey regions are silicon seen through an oxide mask. Dark grey regions are undercut oxide mask. The isolated structure is on the left in each picture.

Figure 4-16: Thermal isolation during cooling jacket etch.

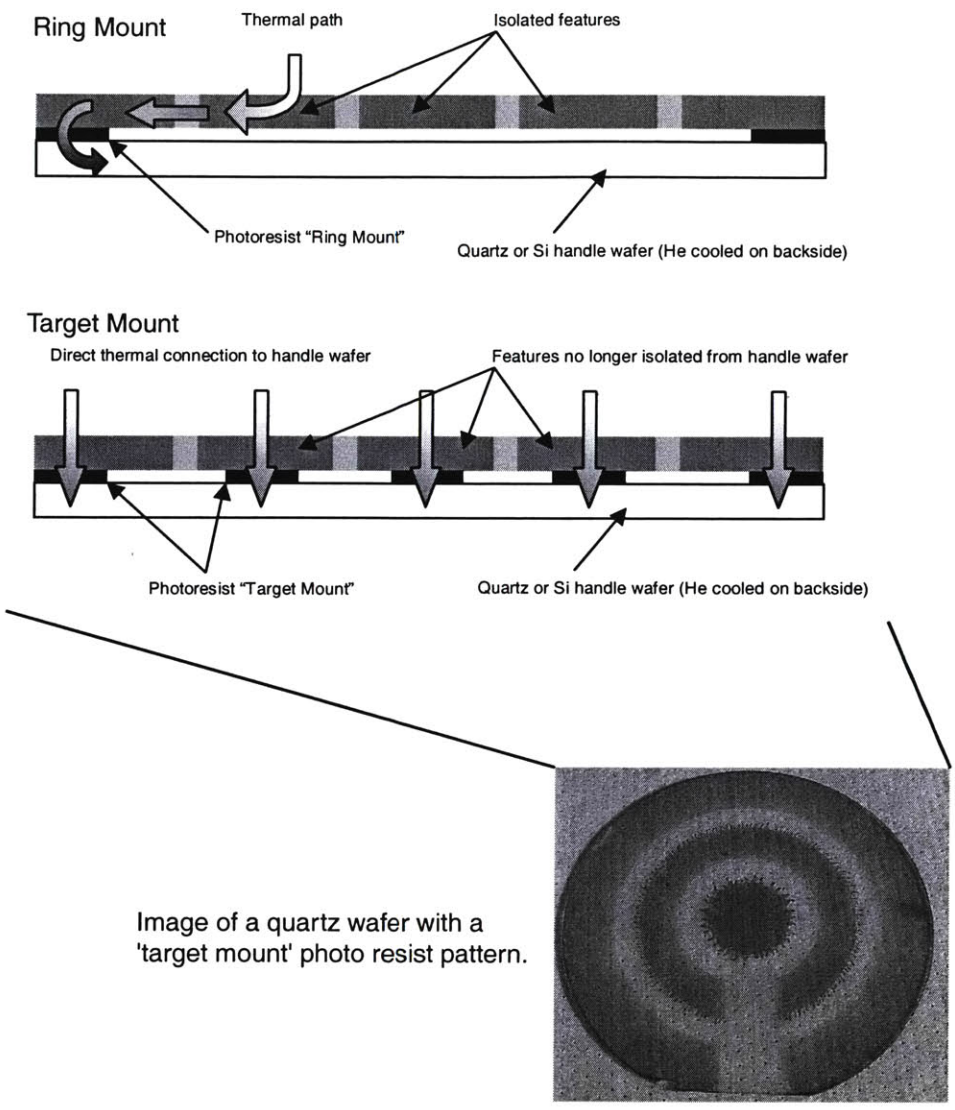

Figure 4-17: 'Target mount' handle wafers.

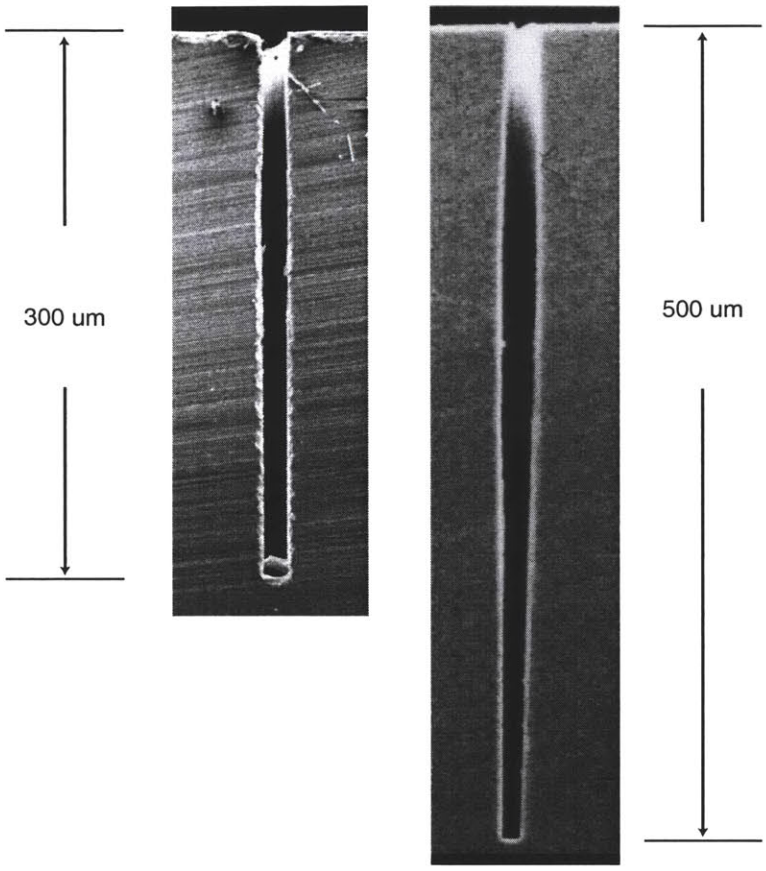

Figure 4-18: Deep journal bearings.

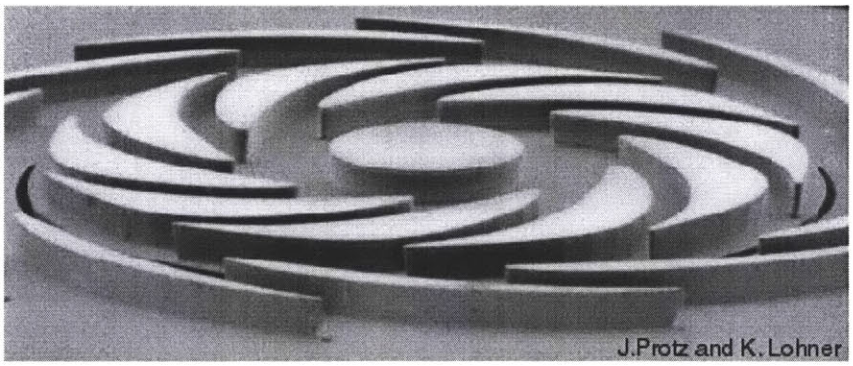

Figure 4-19: 400um blades on a demo engine compressor.

CHAPTER 5

EXPERIMENTAL SETUP

This chapter describes the experimental setup and instrumentation for the demo micro engine device tests. The experimental setup included a mechanical package that interfaced the micro-scale test devices to the conventional-scale sensors, an integrated instrumentation and gas handling system, and a computerized data acquisition and reduction system. The instrumentation system is designed for both the turbocharger and the demo engine test devices. It is derived from the instrumentation systems used in [1,2] and shares many features with these systems.

5.1 PACKAGING

The demo engine test devices require fluidic packaging to interface them with the external environment. The packaging brings in fuel for the combustor, external supply air for the gas bearings and turbine, and pressure lines for the various pressure taps. The packaging must simultaneously conform to the constraints imposed by fabrication, device operation, and testing. This led to two different packaging schemes: a "cold package" for room temperature testing of the turbomachinery, and a "hot package" for tests with an operational combustor. Only the cold package was used for the experiments presented here.

5.1.1 COLD PACKAGING

Because it does not include an operating combustor, the turbocharger runs at room temperature. The demo engine is also tested at room temperature to characterize the turbomachinery. The primary role of the packaging is to supply leak-free fluidic connections to the macro-scale device instrumentation. The packaging scheme should not require additional die processing beyond

rotor release. The packaging should allow convenient disassembly and re-assembly for rapid testing.

The cold package design is similar to the 3-plate Plexiglass/Aluminum packages used in [1] and [2]. The package consists of top and bottom plates of stainless steel that sandwich the die and an aluminum spacer plate that positions the die. Fluidic interconnect flow paths are machined into the stainless steel plates. O-rings seal the fluidic ports at the plate/die interface. The aluminum spacer is two mils thicker than the die, ensuring that the o-rings, not the steel plates, contact the device. O-ring compression is nominally 33%. Figure 5-1 illustrates complete cold package.

A Plexiglass/Aluminum cold package was also built. This package leaked at the o-ring seals and was not used for testing. The Plexiglass/Aluminum package is illustrated in Figure 5-2 to aid visualization of the cold packaging scheme.

The demo engine and turbocharger have 16 fluidic interconnects. All 16 connections are on the front side. This is in contrast to the micro bearing and motor compressor packages of [1] and [2]. This front-side-only approach maintains compatibility with the 'hot package' process detailed below. There are four 2 mm OD interconnects and twelve 0.900 mm OD interconnects. Two interconnects are for fuel and are not used for cold testing. All interconnects are spaced 3.75 mm apart on a 15 mm square. To achieve the close spacing, all interconnects are sealed with Buna-Nitrile (BN) specialty o-rings (0.035 in. x 0.016 in. and 0.078 in. x 0.016 in.) from Apple Rubber Products Inc.

The package is currently designed to draw compressor main air from the atmosphere and exhaust turbine main air into the atmosphere. However, both the inlet and exhaust flow paths have provisions for o-ring seals and may be easily modified for pressurization or mass flow measurement. Consult the appendices for detailed drawings of the cold package.

5.1.2 HOT PACKAGING

The cold package described above is suitable for room-temperature tests. Extended testing of the demo engine devices at design operating temperature requires an alternate packaging scheme.

Though it was not used for the present tests, a high-temperature package was developed as part of the demo engine development effort. The details of the hot package are described below.

The demo engine combustor is designed to run with gas temperatures as high as 1600K, giving static structure temperatures of 800 K and 1000 K on the front and back of the die, respectively. Elastomer o-ring seals cannot operate for extended periods at these temperatures. Conventional Buna-Nitrile (BN) o-rings are good to 400 K (250 F). "High-temperature" fluorocarbon and silicone o-rings can survive up to 500 K (450 F). As a result, extended tests of the demo engine require an alternate packaging scheme. The chosen scheme uses glass-bead braze connections to Kovar micro tubes. The Kovar/glass combination was originally developed for the microrocket [4]. The combustor 'hot rig' also used this Kovar/glass approach [3].

Figure 5-3 shows a hot-packaged dummy microengine device. The device has 16 fluidic interconnects. All 16 connections are on the front side to simplify the packaging process. Kovar tubes with outside diameters of 2mm and 0.900 mm connect the die to an intermediate metal "braze-plate." The tubes are sealed to the die with glass beads. The tubes are sealed to the metal plate with copper-silver braze. Glass and braze connections are formed in a single pass through a controlled-atmosphere furnace at 1300K. The packaging was performed by Thunderline-Z. Consult [5] for specific process details. The braze-plate bolts to a stainless steel block with provisions for macro-fluidic connections identical to those used for the cold package. Elastomer o-rings form a seal between the braze-plate and the macro-connection plate. The current package is designed for atmospheric operation. An extended package with the ability to pressurize the inlet flow is under development.

Initial testing by London shows that the glass/Kovar packaging scheme can operate at pressures in excess of 2000 psi at room temperature [4]. Mehra operated up to 50 psi with die temperatures exceeding 800K [3]. Harrison has performed extensive characterizations of the glass/Kovar seal process and properties [5].

5.2 Gas Handling and Instrumentation System

The integrated gas handling system and instrumentation system supplies nitrogen or air to the test device, measures pressures and mass flows into and out of the device, and sensors rotor speed.

Figure 5-4 shows a schematic diagram of the demo engine gas handling and instrumentation system. Figure 5-5 shows a photograph of the gas handling system. This system is based on the gas handling rig designed by Lin for micro bearing rig experiments [1].

The gas handling system has three major branches corresponding to the thrust bearing, journal bearing, and turbine main flow systems. The thrust bearing and main flow branches are supplied via a primary pressure regulator that regulates 160 psi bottled nitrogen or bottled dry air. The journal bearing branch is tapped from the turbine main flow branch.

The first branch of the gas handling system supplies the forward and aft thrust bearings through a pair of pressure regulators. All thrust bearing mass flows are measured by 0-500 sccm MKS 179A electronic mass flow meter. All pressures are measured by 0-100 psi Omega 242PC100G gauge pressure transducers.

The second branch supplies main air to the turbine for turbocharger tests or demo engine startup. The pressure in this branch is controlled by a second pressure regulator and a set of manual needle valves. Turbine mass flow is measured by a 0-20,000 sccm MKS 179A electronic mass flow meter. Turbine supply pressure is measured by a 0-100 psi Omega 242PC100G gauge pressure transducer.

The third branch supplies the air to the journal bearing for hydrostatic journal pressurization. This branch is tapped off just downstream of the turbine main flow pressure regulator. Flow through this branch is controlled by a set of manual needle valves. Journal bearing supply mass flow is measured by a 0-100 psi Omega 242PC100G gauge pressure transducer. Differential pressures between the journal bearing supply and the compressor and turbine inter-row pressure taps are measured by a pair of 0-15 psi Omega PX139-015D4V differential pressure transducers.

The remaining pressure demo engine taps are connected to 0-100 psi Omega 242PC100G gauge pressure transducers. All pressure transducers are supplied by a common 10V power supply. All electronic mass flow meters are driven by a bank of MKS Type 247 4-channel mass flow readout modules.

The gas handling system also has provisions for supplying fuel to the demo engine for integrated combustor tests. Hydrogen or hydrocarbon fuels are in a separate flow line.

The rotational speed of the demo engine was measured by a Philtec D6-H2TV high-frequency fiber-optic position sensor. The sensor measures the passing of three tabs built into the compressor and turbine hubs (see Figure 5-6). The speed sensor output is converted into a rotational frequency by passing it through an HP87410A DC-10MHz spectrum analyzer and measuring the maximum amplitude frequency. The Philtec sensor has a specified bandwidth of 300 MHz making it useful for engine speeds of up to 1.7 million RPM. It is positioned in the engine inlet with a Newport 461 high-precision XYZ stage. For additional details on the Philtec sensor, consult [1,2].

5.3 DATA ACQUISITION SYSTEM

The demo engine experimental setup shared its data acquisition system with the setup of [2]. The setup is illustrated in Figure 5-5. A 300 MHz Dell Optiplex GX1 PC acquired and recorded the output of the pressure transducers, mass flow sensors, and speed sensor. The pressures and mass flows were sampled at 1.2 MHz on a National Instruments PCI-6071E A/D board multiplexed to 64 channels. The demo engine used channels 33-64. Five data points were recorded every second, each data point representing the average of 250,000 samples. All pressured transducers were connected to the A/D board as differential inputs. All mass flow meters were connected as single-ended inputs with a common ground. The A/D system was programmed in the LabVIEW programming environment. Speed data from the spectrum analyzer was downloaded via a GPIB connection. The PC stored all data in a variable-size circular data buffer. For additional details on the data acquisition system, consult [2].

5.4 REFERENCES

[1] C. C. Lin, *Development of a Microfabricated Turbine-Driven Air Bearing Rig.* PhD thesis, MIT, Department of Mechanical Engineering, 1999.

[2] L. G. Frechette, *Development of a Silicon Microfabricated Motor-Driven Compressor*, PhD Thesis, MIT, Department of Aeronautics and Astronautics, 2000.

[3] A. Mehra, *Development of a High Power Density Combustion System for a Silicon Micro Gas Turbine Engine*, PhD thesis, MIT, Department of Aeronautics and Astronautics, 2000.

[4] A. P. London, *Development and Test of a Microfabricated Bi-Propellant Rocket Engine*, PhD Thesis, MIT, Department of Aeronautics and Astronautics, 2000.

[5] T. Harrison, MS Thesis, MIT, Department of Aeronautics and Astronautics, 2000.

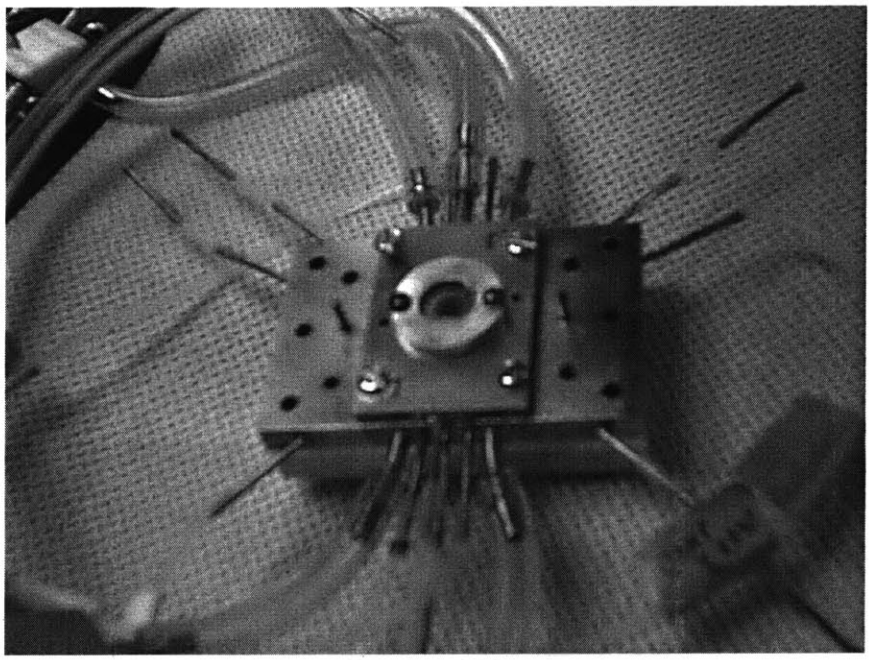

Figure 5-1: Metal cold package used for experiments.

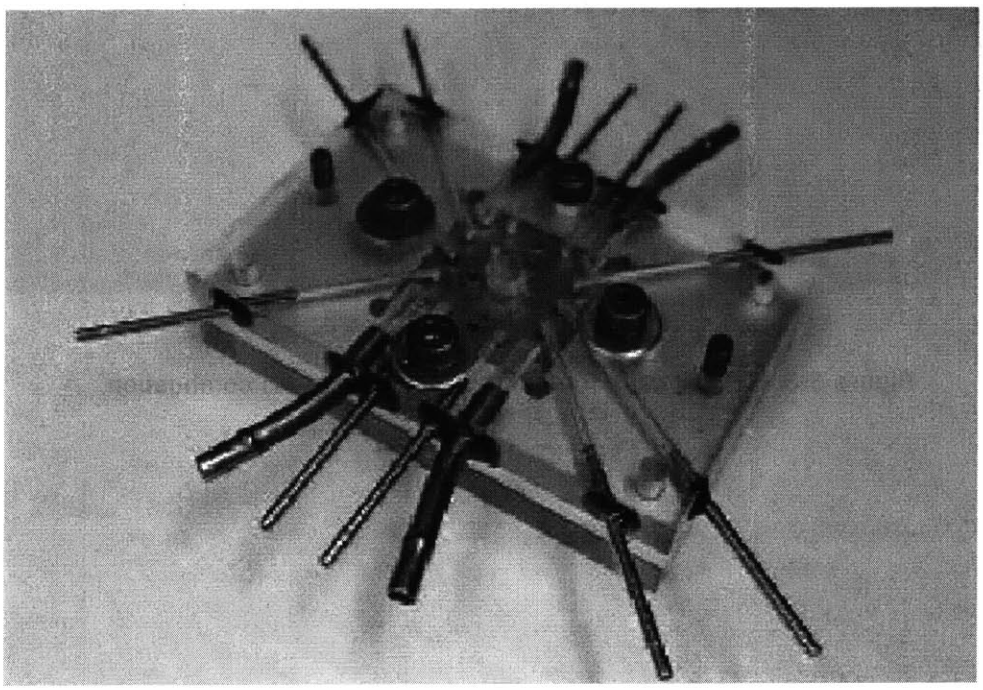

Figure 5-2: Plexiglass cold package showing device and flow passages.

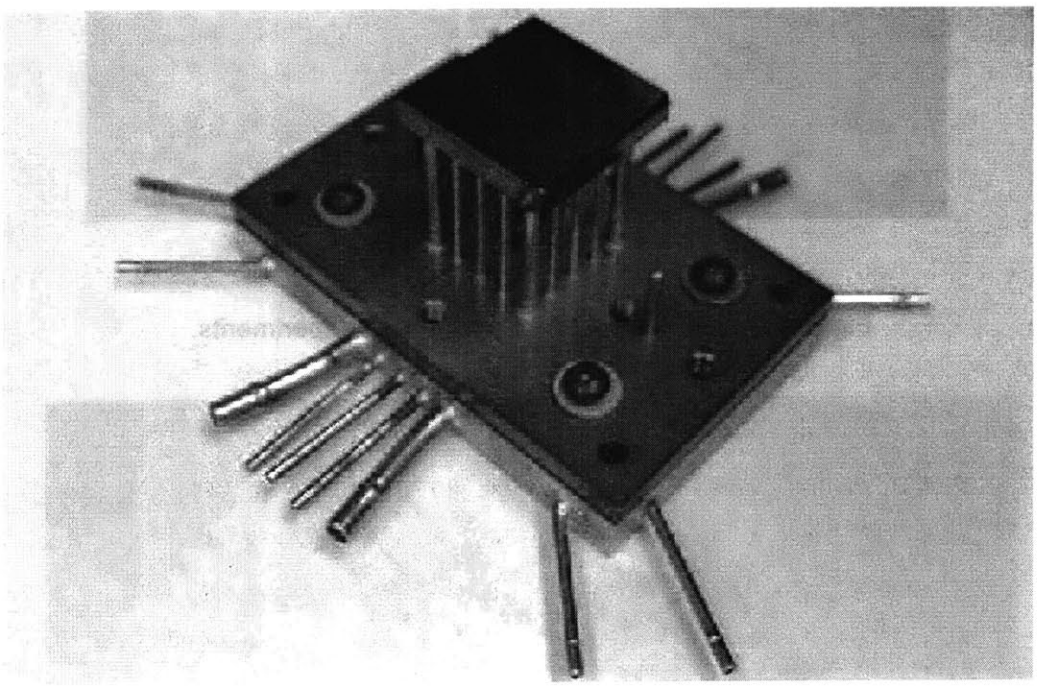

Figure 5-3: Hot package for long duration tests with combustion.

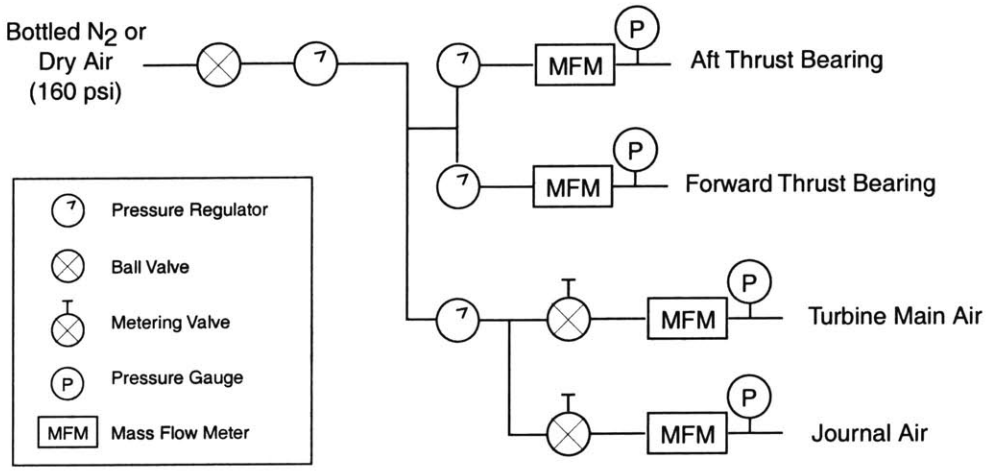

Figure 5-4: Schematic of gas handling system.

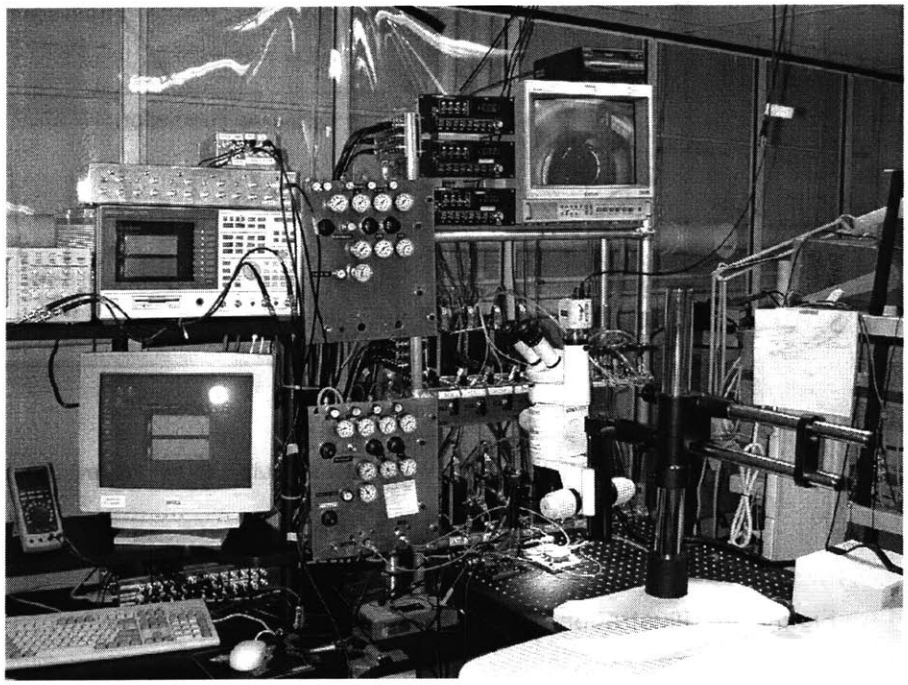

Figure 5-5: Photograph of gas handling system.

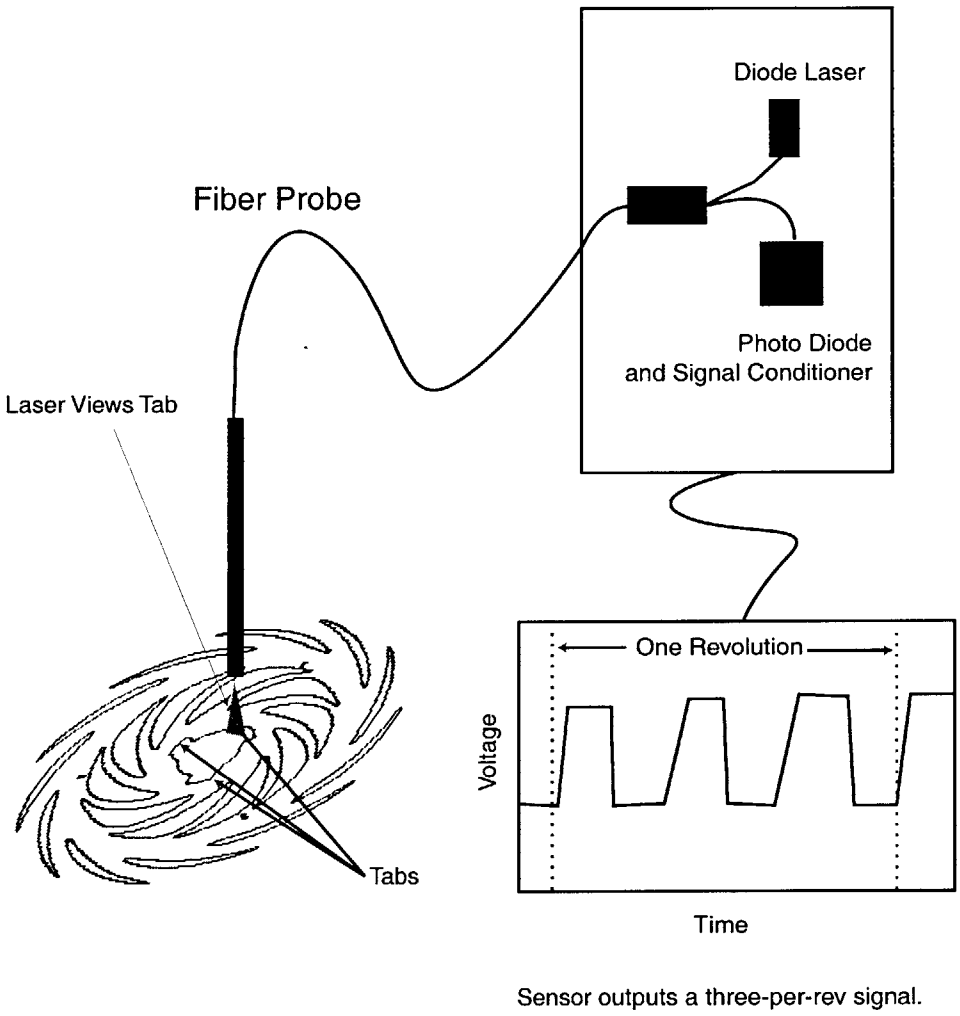

Figure 5-6: Illustration of fiber optic speed sensing system.

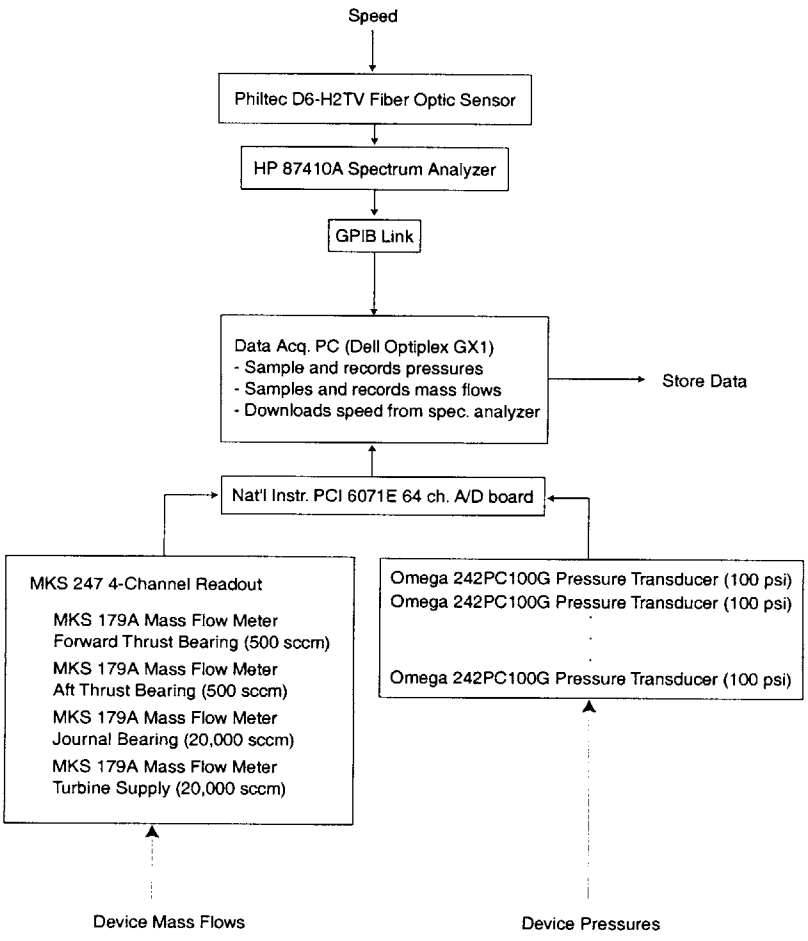

Figure 5-7: Schematic of data flow in data acquisition system.

CHAPTER 6

EXPERIMENTAL RESULTS

This chapter describes the results to date of the turbocharger experimental testing effort. The test effort indicates that the current devices are limited to low speeds (30,000 RPM or 2% of design speed) by imbalance.

Four types of tests are considered here: thrust bearing static flow characterization, journal bearing static flow characterization, and rotor spin tests. The static flow tests characterized the functional behavior of the thrust bearings and journal bearing pressurization system and validated that behavior against theoretical predictions. The released rotor dynamic tests characterized the behavior of spinning devices.

6.1 THRUST BEARING EXPERIMENTS

Thrust bearing static flow tests identified the as-fabricated geometry of test dies. Two thrust bearing tests were used. The first validated thrust bearing flow rates against theoretical predictions. The second identified the proper operating point for later spin tests.

The first thrust bearing flow test indirectly measured the geometry of the thrust bearings. Two cases were tested. First, unreleased dies were pressurized. In this case, the aft thrust bearing has a fixed, full-open gap of 7 um. In the second case, released dies are tested by venting one thrust bearing and pressurizing the other. This closes the vented bearing's gap, again resulting in a known, full-open 7 um gap. The flow measurement is therefore an indirect measurement of the geometry of the aft thrust bearing. Figure 6-1 illustrates the measured flow properties for the

thrust bearings of several different die from builds 6 and 7 of the turbocharger and from build 8, the first demo engine build.

The plot also shows the theoretical thrust bearing flow properties based on a bearing with a total gap of 7 um (3.5 um for each thrust bearing when centered) and twenty 100 um long restrictors. Theoretical predictions are plotted for both 12 um diameter and 10 um diameter restrictors. The designed restrictor diameter is 11 um and in-fab measurements showed a variation between 10 um and 12 um. The theoretical results were generated by Jacobson and assume a compressible flow [1].

The comparison of experimental and theoretical results shows that the turbocharger thrust bearings do in fact possess the design geometry and, therefore, should provide the requisite stiffness. Lin has already demonstrated that satisfactory static flow results also predict satisfactory bearing stiffness for this type of hydrostatic thrust bearing [2].

The second set of thrust bearing experiments identified the thrust bearing operating point for spin tests. In these experiments, one bearing is pressurized to a modest pressure (30-50 psi) while the other is varied in pressure from low (0 psi) to high pressure (100 psi). By observing the change in mass flow through the bearing with fixed pressure, one can identify when the bearing is centered. During subsequent spin tests, the rotor is kept centered axially by varying the pressure in one bearing to maintain the mass flow in the second, fixed-pressure bearing. Experiments showed a smooth transition from high flow to low flow, indicating a stiff bearing.

6.2 Journal Bearing Experiments

The journal bearing was characterized with two different static flow tests. The first test measured the behavior of the hydrostatic journal bearing supply lines. The second measured and compared the flow properties of the journal bearing and compressor rim seal to CFD calculations and theoretical predictions. The tests identified two drawbacks of the current geometry that should be corrected in future builds.

Journal Supply Line Tests

In the first test, the die was completely vented, the journal bearing supply plenum (compressor backside plenum) was pressurized, and the supplied mass flow was measured. This test measures the cumulative mass flow through the journal bearing as a function of supply pressure. Figure 6-3 illustrates the test results for several released and unreleased dies. The results show a lower flow rate than expected. At a supply pressure of 10 psi, the anticipated cumulative flow through the compressor gap and journal bearing is 8000 sccm. The measured flow is less than 1000 sccm.

The discrepancy between theory and measurements is apparently a result of choking in the die-internal supply lines leading to the journal bearing. All of the tests show that mass flow is linear with supply pressure. This suggests a choked flow. The internal supply line is a one-centimeter long, 350 um x 400 um square-cross section passage. The plot compares the data to the theoretical flow through a choked 350 um x 400 um passage with a discharge coefficient of 0.75. The measured and predicted slope agree to within +/- 10%. Choking was confirmed by plugging the compressor inlet and discharge. This forces all flow to move through the journal bearing. An increased flow rate out of the turbine was plainly audible, however the measurement of supplied mass flow did not change, indicating choking upstream of the journal bearing plenum.

The plenum and supply lines currently used to pressurize the bearing were originally designed to be used as a thrust-balancing and side pressurization system for a hydrodynamic journal bearing. Under this scheme, the plenum would provide small pressure forces. The hydrodynamic bearing does not require pressure drop across the bearing and there would be very little flow; less than 2% of the core engine mass flow. The decision to use these flow lines as a hydrostatic bearing came after the micro bearing rigs of [2] and [3] made it clear that a hydrostatic allowed high-speed operation. With hydrostatics, the bearing requires flows that are 30% or more of the core engine flow. Larger lines would have been preferred, but by this stage, the devices were already in process.

Choking drives up the external supply pressure required to achieve a given journal mass flow. Although the pressure is the journal bearing plenum may be only a few psi, the supply line will require tens of psi. The current tests have been limited to supply pressures of 20 psi. For the current geometry, this corresponds to a theoretical bearing natural frequency of 30,000 RPM.

The maximum possibly supply pressure with the current equipment is 120 psi, corresponding to a natural frequency of 80,000 RPM.

Two changes are suggested to solve this problem. The first is to increase the size of the supply lines. This requires a new mask for the aft thrust bearing wafer plenum etch (the etch also defines fluidic interconnects) and may require larger through-NGV supply lines (the NGV lines will choke next if the supply line is enlarged). These changes can only be implemented in new device builds. A compressor rim seal should also be included to eliminate the compressor gap leakage path.

The second approach is to supply the journal bearing by pressurizing the compressor region and driving flow into the journal bearing through the compressor gap. This approach takes advantage of the lack of a compressor rim seal and it does not require changes to the device masks. The disadvantage of this approach is that it requires separation of the compressor discharge and turbine supply pressure. This makes it difficult to implement in the demo engine where the compressor and turbine are linked via the combustor.

The second approach was attempted experimentally. The results are described in later sections.

Journal Flow Properties

A second set of journal experiments was performed to identify the journal flow properties. In these experiments, flow was driven independently through the compressor and journal gaps. Flow through the compressor gap was achieved by plugging the turbine exhaust and supply and pressurizing the journal tap. This forces flow from the journal supply through the compressor gap. Because the turbine is plugged, it acts as a presssure tap for the supply air. Flow through the journal was achieved by plugging the turbine inlet and venting compressor inlet while pressurizing the turbine through the turbine exhaust. All other connections were plugged. This forces flow sequentially through the journal and compressor gaps. However, because the journal is much smaller, the bulk of the pressure drop will occur here.

Figure 6-2 compares the measured and theoretical results of this experiment for two different die. Both analytical [4] and 2D [5] CFD theoretical results are considered. The analytical prediction is parameterized by an unknown discharge coefficient. A coefficient of 0.40 leads to good

agreement with the experimental measurements. The results show that the analytical theory agrees with the experiments within the error bounds of the measurements. The CFD slightly (10%) overpredicts the compressor gap flow rate, but the experiments and predictions both show that the compressor gap has three to four times the flow rate through the journal bearing gap for the same pressure drop.

The large compressor gap flow rate results from the lack of a compressor disk 'rim seal.' The baseline demo engine design called for a rim seal to separate the compressor backside plenum from the compressor gap. As mentioned in previous chapters, this seal was removed to simplify the fabrication process and to alleviate a structural concern associated with rotor tip deflection at high speeds. Removing the seal opens a leakage path between the compressor and the compressor backside plenum. If operated hydrodynamically or from internal pressures, this leakage path would cause little concern. However, when the journal is pressurized externally to pressures much higher than the compressor discharge pressure, there is substantial leakage through this gap. The experimental and theoretical results show that this leakage is 3-4 times the journal bearing flow rate. This large compressor gap flow rate is evidenced experimentally by the fact that the compressor is driven in reverse when the journal is pressurized and the turbine supply is plugged. The substantial compressor reverse flow overpowers the turbine forward flow.

The compressor leakage flow has little impact on bearing performance. Jacobson's calculations show that the presence of the compressor gap flow increases the journal bearing natural frequency by less than 10%. However, the extra leakage flow does impact the supply lines. The choked supply lines must not only supply the journal bearing mass flow they must also supply the compressor gap leakage flow. This drives up the supply pressure required to obtain a given journal bearing mass flow and, hence, natural frequency.

The predictions are based on the choked inlet supply line described above and on Jacobson's model of journal bearing behavior and compressor gap behavior[15] show that considerable mass flow is required to achieve bearing stiffness. Even without the compressor gap, the ratio of supply pressure to journal bearing pressure is 3:1. With the compressor gap, this ratio goes to

---

[15] Predictions assume a journal and gap discharge coefficient of 0.2.

12:1. At these ratios, it is impractical to supply the journal bearing with the mass flow needed to achieve high (order 250,000 RPM) natural frequencies.

This problem may be solved by including a compressor rim seal to reduce the leakage. Inclusion of a seal requires mask changes and a new device build. Alternatively, if the journal is pressurized by pressurizing the compressor as recommended above, the compressor gap leakage flow is the journal supply line and low pressure drops (large 'leakage' flows) become, in fact, desired.

6.3 Rotor Spin Tests

The first and second successful builds (build 6 and build 7) of the turbocharger resulted in seven testable devices. All seven of these devices were spin tested. As of this writing, the maximum rotational speed achieved by the turbocharger is 20,000 RPM. This is considerably below the 1.2 million RPM design speed. It is also below the 1.5 million RPM (750,000 RPM scaled to the demo engine) speed achieved by the micro bearing and micro motor compressor rigs of [2] and [3].

Experimental evidence suggests that the operating speed of the fabricated turbocharger devices is limited by the combination of three factors: (1) choked flow in the journal bearing supply system, (2) leakage flow from the journal bearing plenum into the compressor, and (3) imbalance. The first two factors are operational convenience issues and do not represent a genuine limit on the current demo engine design. The third factor fundamentally limits rotor speed and hence operation of the engine. This factor must be solved before the device can be driven to design speeds.

Two primary methods of operation were attempted. The first relied on pressurization of the journal bearing via the journal bearing pressure tap that runs through the NGVs. The second achieved pressurization of the journal by pressurizing the compressor flow path, supplying the journal via leakage through the compressor running gap. Each method had several variants, depending on which fluidic interconnects were plugged or vented

Pressurization of the journal via the journal pressure tap allows direct measurement of the total compressor gap and journal bearing mass flow. However, because the pressure tap is used as the supply line, the journal bearing pressure is unknown. In this variation, the journal was pressurized while the compressor inlet and discharge were vented, the turbine discharge was vented, and the turbine inlet was supplied with main air from the gas handling system. This is the originally envisioned pressurization scheme for the turbocharger. A second variation was similar except that the compressor discharge and inlet were plugged, forcing most of the journal flow into the turbine flow path (the compressor inlet seal is leaky, allowing some flow out the compressor inlet). This configuration minimizes journal supply flow rate for a given stiffness and reduces the effect of flow through the compressor. Both of these variations suffer from reverse flow in the compressor. A third variation used a plugged compressor inlet and a vented compressor discharge. This reintroduces a large leakage through the compressor running gap, but eliminates the reverse flow in the compressor.

The second method of journal bearing pressurization works by pressurizing the compressor region and driving flow into the journal bearing through the compressor gap. This approach takes advantage of the lack of a compressor rim seal. The advantage of this approach is that it allows the journal pressure tap to be used as a direct measurement of journal bearing pressure. The disadvantage is that the flow rate through the journal cannot be measured. A second disadvantage of this approach is that it requires separation of the compressor discharge and turbine supply pressure. This makes it difficult to implement in the demo engine where the compressor and turbine are linked via the combustor.

The micro turbochargers were tested experimentally. Regardless of the pressurization approach, the micro turbocharger qualitatively exhibited the same spinning behavior as early builds of the micro bearing test rig [6], suggesting that the turbocharger device is not subject to any additional physical effects. Figure 6-4 illustrates a spectrogram from a turbocharger device accelerating from 3000 RPM to 4000 RPM. The spectrogram shows a series of peaks synchronous with the rotor frequency. The speed response is first order. The spectrogram does not show any peaks associated with a fixed frequency. Such a peak would indicate the hydrostatic natural frequency. Based on the bearing models, the turbocharger is believed to be operating sub-critically. The absence of a fixed-frequency peak supports this hypothesis as the experiments of Jacobson *et al*

[6] with the micro bearing rig only showed a fixed-frequency peak when operating super-critically.

Impact of Imbalance

The observations above explain a low (order 10,000 RPM) journal bearing natural frequency. Alone, they do not explain a low maximum operating speed. Lin and Frechette's devices demonstrated operation at speeds of up to 1.5 million RPM, giving tip speeds in excess of 250 m/sec[16] [6]. At these speeds, the devices were operating at more than 5 times their bearing's measured natural frequency. By extension, the turbocharger as run should have achieved speeds in the 50,000-100,000 RPM range.

The explanation lies in rotor imbalance. The imbalance level of the turbocharger is much more sensitive to process parameters than the imbalance level of the micro bearing rigs. The only two sources of imbalance in the micro bearing rig are non-uniformity of the turbine blade etch and front-to-back mask misalignment between the journal bearing and the blades. The turbocharger must face these challenges for both the compressor and the turbine. In addition, the imbalance level of the turbocharger is sensitive to the bond alignment between the two wafers. Finally, due to the layout of the dies on the wafer, the turbocharger blade etches show much more non-uniformity (15 um vs 5 um for outer die) than the micro bearing etches.

The overall result is that the turbocharger has considerably more imbalance. Based on metrology, the demo engine has an imbalance level of 70-120% versus less than 10% for high-speed micro turbine dies.

The effect of imbalance is to reduce the speed at which the rotor will go unstable for a given natural frequency. As the rotor speed approaches the natural frequency, the bearing becomes easily excited by forcing. The forcing level is proportional to the square of the rotor speed and to the level of imbalance. The larger the imbalance, the lower the speed required to achieve a given level of forcing. The rotor displacement associated with the forcing will excite potentially

---

[16] The micro bearing rigs have a journal diameter of 4 mm, 33% smaller than the 6 mm turbocharger journal diameter and 50% smaller than the turbocharger's 8 mm diameter compressor. For a given speed in RPM, the wall speed in the bearing in correspondingly lower. For similar geometries, centrifugal effects increase with tip speed not rotational frequency.

destabilizing hydrodynamic modes, leading to a wall strike. Also, beyond the natural frequency, the rotor motion inverts and the rotor spins around its center of mass rather than its geometric center. Clearly, if the imbalance level exceeds 100%, this will lead to an immediate wall strike. In this way, the turbocharger imbalance level should lead to crashes at much smaller multiples of the natural frequency than the more-balanced micro-bearing rig experiences.

If the turbocharger and demo engine could be balanced, they should achieve higher operating speeds regardless of the above-described limitations on natural frequency resulting from the internal device geometry.

Assessment of Current Geometry

The operating speed of the fabricated turbocharger devices is limited by the combination of three factors:

(1) Choked journal bearing supply lines – The fluidic lines internal to the die that supply the hydrostatic journal bearing are too small to handle the flow without choking. Choking drives up the supply pressure required to achieve a given journal mass flow.

(2) Leakage flow through the compressor – When the journal bearing is pressurized, flow leaks from the journal bearing plenum into the compressor through the compressor running gap. This flow has a limited (less than 10%) impact on the journal bearing's behavior, but substantially increases the total supply mass flow for a specified stiffness. The extra flow exacerbates the choking problem.

This problem may be solved by including a compressor rim seal to reduce the leakage. Inclusion of a seal requires mask changes and a new device build. Alternatively, if the journal is pressurized by pressurizing the compressor as recommended above, the compressor gap leakage flow is the journal supply line and low pressure drops (large 'leakage' flows) become, in fact, desired.

(3) Imbalance – Imbalance is the fundamental limit on the turbocharger operating speed. Imbalance is due to the misalignment of bonds and etches.

6.4 Recommendations for Future Work

The observed experimental results suggest the following changes to the design and operation of the micro turbocharger and demo engine:

(1) Improve the balance of the rotor through dynamic balancing or through improved fabrication processes. The turbocharger's measured high levels of rotor imbalance combined with other researchers' experimental demonstrations that imbalance limits rotor speed [6] indicate that the turbocharger and demo engine cannot achieve design speed at the current levels of imbalance.

(2) Enlarge the flow passages upstream of the journal bearing plenum to accept the anticipated high journal bearing mass flows (30% of turbine core mass flow). This change improves the operability of the device. If the tortuous isolated combustor geometry is retained, this recommendation may entail reducing the combustor isolation or adding backside fluidic interconnects. It may also entail larger NGVs to accommodate larger through-NGV interconnects.

(3) Implement a compressor disk rim seal to isolate the compressor backside plenum from the compressor core flow. This reduces the flow levels required for external journal pressurization and allows independent control of the journal and compressor pressures. A configuration analogous to the 'compressor tap' operation described above could still be implemented by externally shorting the compressor inter-row tap in the second wafer level to the journal supply line.

With these recommendations implemented, the demo engine and turbocharger should be able to reach full speed. At high speeds, the turbomachinery should produce measurable changes in pressure. It should also be possible to implement simultaneous spinning and combustion with injected or pre-mixed hydrogen fuel. Given full-speed operation, the following experiments can be conducted to estimate overall engine references:

6.5 REFERENCES

[1] S. A. Jacobson, Personal Communication, 2000.

[2] C. C. Lin, Development of a Microfabricated Turbine-Driven Air Bearing Rig. PhD thesis, MIT, Department of Mechanical Engineering, 1999.

[3] L. Frechette, Development of a Silicon Microfabricated Motor-Driven Compressor, PhD Thesis, MIT, Department of Aeronautics and Astronautics, 2000

[4] S. A. Jacobson, Personal Communication, 2000.

[5] Y-F Gong, Personal Communication, 2000.

[6] L. G. Frechette, S. A. Jacobson, K. S. Breuer, F. F. Ehrich, R. Ghodssi, R. Khanna, C. W. Wong, X. Zhang, M. A. Schmidt, A. H. Epstein, "Demonstration of a Microfabricated High-Speed Turbine Supported on Gas Bearings," presented at Solid-State Sensor and Actuator Workshop, Hilton Head Island, SC, June 2000.

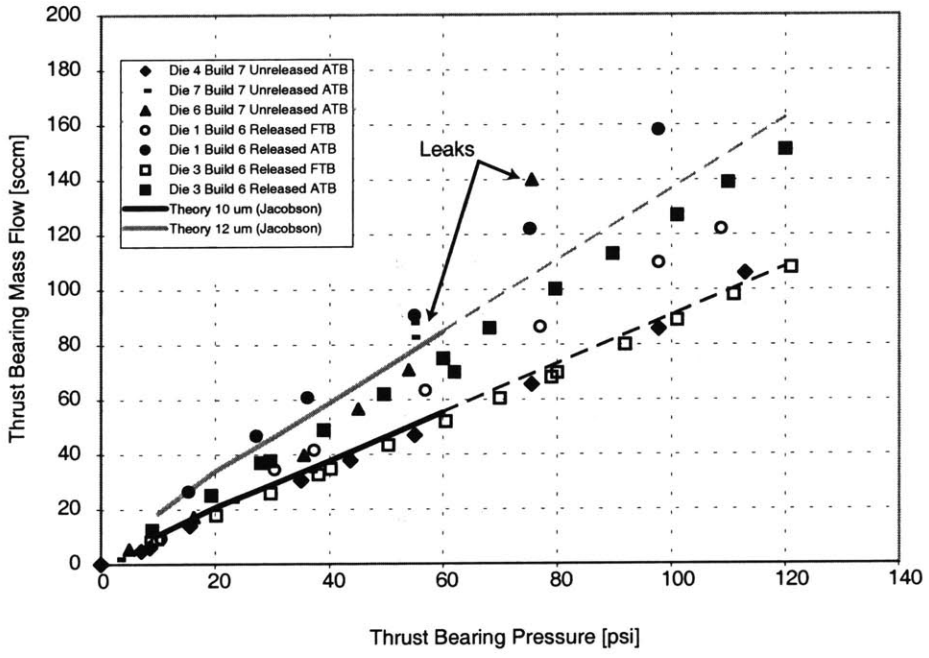

Figure 6-1: Results of thrust bearing static flow tests.

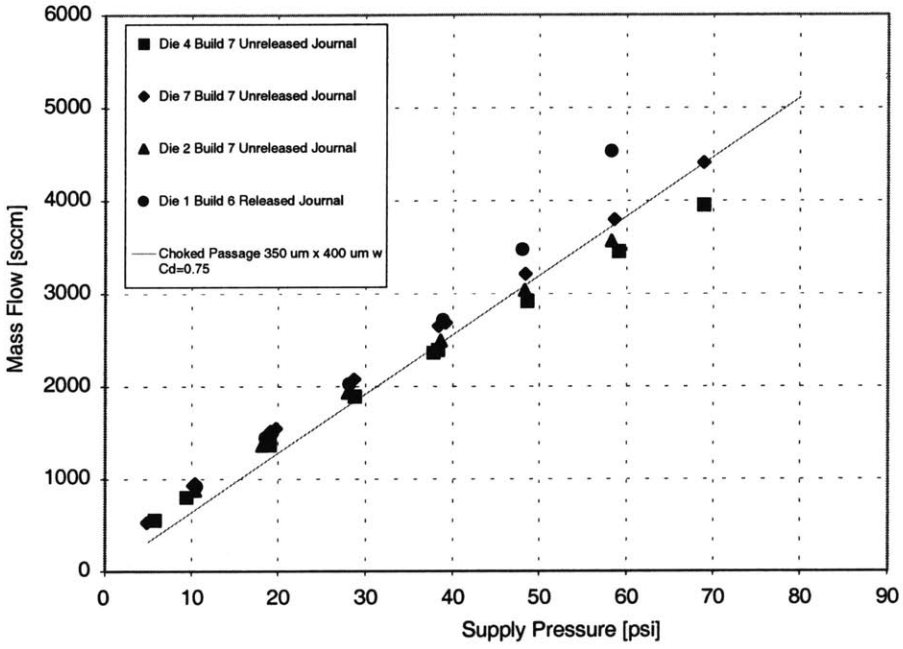

Figure 6-3: Flow test through journal tap showing choked behavior.

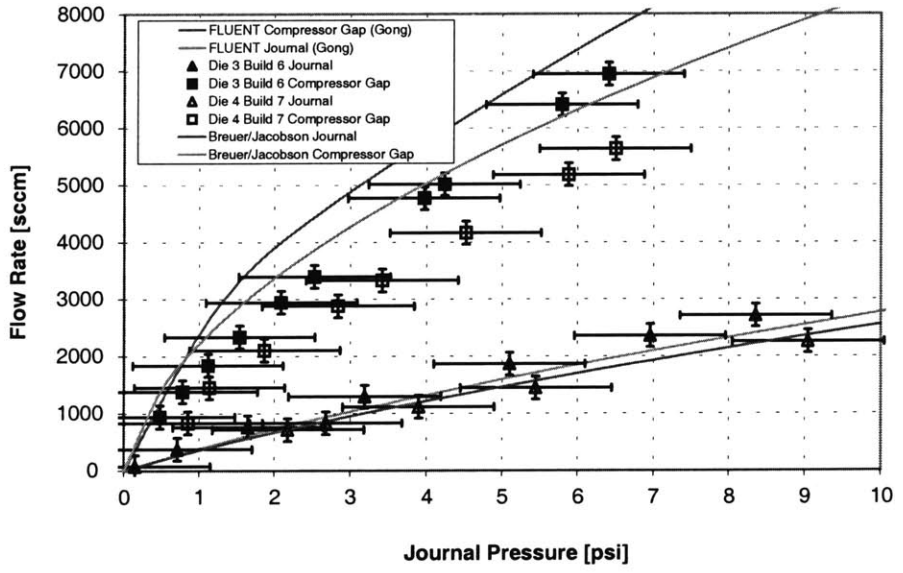

Figure 6-2: Comparison of journal flow rate to analytical and CFD models.

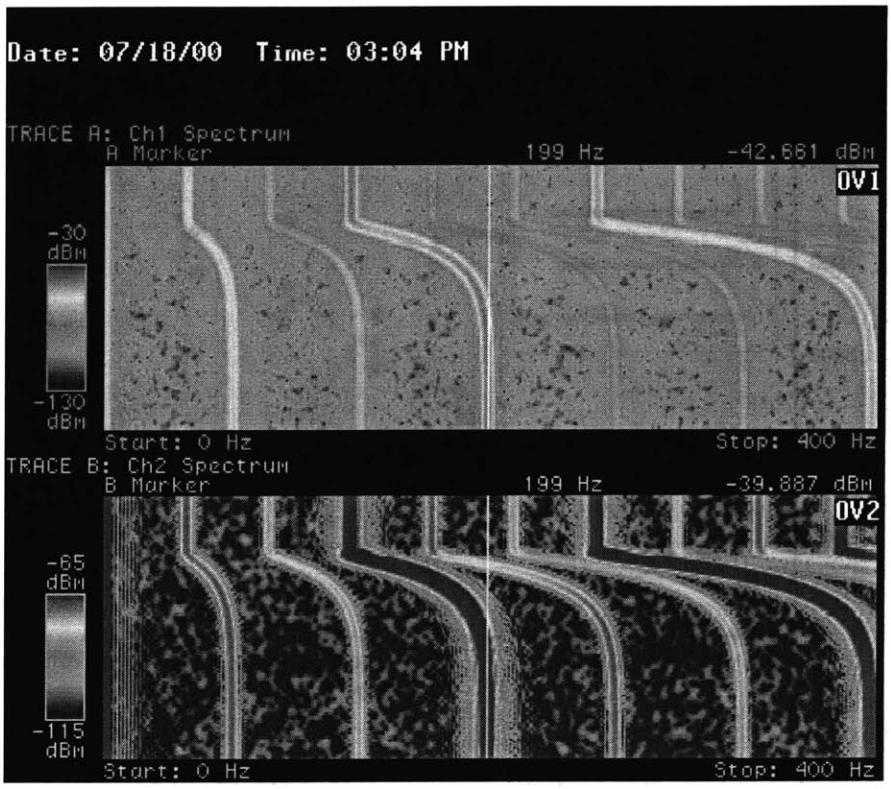

Figure 6-4: Spectrogram for turbocharger accelerating to higher speed.

CHAPTER 7

CONCLUSION

This thesis describes the design and development of a microfabricated gas turbine engine.

7.1 CONTRIBUTIONS

The significant contribution of this work is a design for a gas turbine engine that simultaneously meets the aerodynamic, thermodynamic, and structural constraints of gas turbine design and the manufacturing constraints imposed by the current state of the art in microfabrication.

This contribution entails the following steps:

(1) Design of a device.

(2) Design of a fabrication process (The process was implemented by MIT microfab experts).

(3) Initial testing of a fabricated turbocharger.

This contribution includes the following accomplishments:

(1) An integrated, all-silicon, demonstration microengine was designed using the best available knowledge of micro scale turbomachinery, bearings, combustion, structures, materials, and micro fabrication. This design includes a two-wafer rotor designed to implement an innovate turbine cooling scheme and a micro-combustor with wrap-around thermal isolation.

(2) A set of simple 1-D models for thermal and aerodynamic performance were developed and used to extensively assess the overall system behavior of the design. These models were incorporated into cycle studies of overall engine performance.

(3) The 'etch and bond' turbomachinery fabrication process was redesigned to include nested masks, allowing larger features and a more complex two-wafer rotor geometry. The redesigned process also includes a new thin-film based, parallel-release, rotor retention scheme.

(4) Operation of a fabricated device was demonstrated in a low-speed cold test. The devices were limited to operation at speeds below 30,000 RPM. Metrology and static flow experiments show that imbalance is the likely limiting factor. Static flow characterizations also identified several recommended areas of improvement for the design.

7.2 LESSONS LEARNED

Several important lessons were learned through the course of this work. The lessons of the demo microengine development efforts carried out to date can be divided into two general categories. The first set of lessons are based on the experiences gained during the turbocharger and demo engine fabrication efforts. The second set of lessons are based on the increasingly sophisticated computational analyses of the engine fluid dynamics and thermodynamics. These lessons lead to suggested re-designs for the compressor, turbine, and combustor geometries. Both sets of lessons are summarized below.

Fabrication Lessons

The single most important lesson learned is appreciation of the powerful design constraints imposed on the demo engine by manufacturing. Microfabrication capabilities imposed silicon as the structural material and placed constraints on the size and geometry of the combustor and turbomachinery. However, even more importantly, microfabrication was the primary driver of the development schedule. Unlike the motor compressor of [1] which was an evolution of the micro bearing rig [2], the demo engine was an all-new design that called for many new features that were not present in previous MEMS micro turbomachines. Also, many features were

proposed but not implemented. Although many of the proposed design features are technically feasible (e.g. 400 μm blades and 500 μm journals), the development effort required for these advanced features is substantial. This severely hampers progress towards operational testing. In the case of a research vehicle, where the ultimate goal is an experiment, not process development, the designer should make every effort to avoid modifications to existing processes. The designer should instead focus on building testable devices that fit within the constraints of achievable processes, even if this leads to lower performance.

Geometric specification is a second important lesson. Lin noted the importance of ensuring that the fabricated device meets the design specifications [2]. That lesson was used here for features such as the journal bearing, thrust bearing, and the blades. As the experimental testing showed, the results were very positive. The fabricated geometries closely match theoretical predictions. However, the converse lesson, ensuring that the design accounts for fabrication capabilities, is equally important. For example, imbalance is a key issue for operation. Imbalance depends on etch uniformity. The original design did not adequately consider the existing and achievable etch uniformity. Had this issue been considered in more detail during the initial design stage, it may have led to a focusing of fabrication resources on etch uniformity rather than journal bearing depth or parallel wafer processing.

Simple geometry is a third important lesson. The development effort gave both positive and negative lessons here. The negative lessons include the unsuccessful parallel-wafer, cross-journal tab concept discussed in Chapter 4, Fabrication, and the complicated, cross-bond, through-NGV journal pressurization flow path discussed in Chapter 6, Experimental Results. The interconnect geometry, in particular, made mask revisions tedious and difficult. Positive lessons include the simple and successful oxide-film rotor retention scheme and the simple, two-wafer rotor design. Future researchers should work to avoid untested structural concepts, complicated cross-wafer geometries, and unusual flow paths.

Analysis Lessons

An important lesson of the design effort is the coupling between the thermo-fluidics and the structural design of the engine. Unlike conventional gas turbine engines, there is substantial heat transfer in the demo engine compressor. This heat transfer is used to cool the turbine structure.

However, it also substantially degrades compressor performance and causes a tight coupling between cycle performance and structural design. Even with advanced materials and cooling schemes, this coupling cannot be entirely eliminated because of the small scale of the device. Future research should focus on reducing heat transfer into the turbine through the use of film cooling, advanced materials, etc. Work should also focus on compressor designs that are robust to high wall temperatures.

A related lesson is the importance of high-fidelity modeling of the turbomachinery. From the start, the demo engine was designed to use turbine-to-compressor heat transfer as a cooling mechanism. The qualitative 1D principles were well understood as were the fluidic/structural interactions. However, the theoretical performance impact that this would have on the cycle was not fully understood because there were no 3D calculations. The demo engine was designed around a 2D analysis of the turbomachinery. The necessary 3D tools were simply not available at the time of design. Later results 3D compressor results showed a much larger impact than originally expected and once these results were available, calibration of the 1D models was straightforward. In the absence of a strong experimental base, a coupled 1D and 3D CFD analysis should be used as the primary tool for micro turbomachinery design.

7.3 REDESIGN

This section describes a proposed redesign of the demonstration engine that accounts for the fabrication and design lessons learned as a part of this work. Redesign is a somewhat intuitive process and a number of scenarios are possible. The design presented here seeks maximizes the practicality of the design. This leads to the maximum use of existing process technologies at the expense of other desirable properties such as high device power output. This result is a smaller engine that should be viewed primarily as an experimental vehicle rather than a prototype production device. This new design also retains externally pressurized bearings, thereby avoiding the issue of starting.

The lessons described above indicate that the current demo engine design cannot be built and operated as a closed-cycle jet engine. Although the initial design presented in chapter 2 should work in theory, this design could not be fabricated using existing technology. In particular, the

design calls for hydrodynamic bearings and tall (400 μm) turbomachinery blading. Neither feature can be implemented using current state-of-the art microfabrication technologies. The as fabricated devices introduced shorter blading and a hydrostatic bearing to simplify fabrication. However, analysis for this geometry indicates that such an engine cannot close a cycle. Furthermore, results from the MIT hot static structure rig [3] show that the current combustor design cannot operate with the design mass flow and the expected low pressure ratio of 1.8. Finally, the three-dimensional CFD analyses of the current compressor blading show a lower than expected efficiency, suggesting the need for a turbomachinery redesign.

Redesigned Geometry

Based on the lessons learned, an attempt was made to redesign the layout for the demonstration engine. The new design keeps the existing fabrication process, but calls for a 300 μm hydrostatic journal bearing and a lower engine mass flow. The lower engine mass flow increases the combustor residence time. The journal bearing is supported by bleed air from the compressor discharge. Using the experimental measurements of journal flow from Chapter 6, experimental results, the hydrostatic journal will bleed 20% of the compressor mass flow at a pressure ratio of 1.8. The design turbine efficiency was decreased to 0.60 to better represent preliminary 3D turbine calculations. The combustor exhaust temperature was increased to 1750 K to maintain the same average turbine inlet temperature of 1600 K (the journal bleed will be a comparatively cool 950 K). This new design marginally breaks even. The cycle and parameters are summarized in Table 7-1.

Other variations were also considered including engines with smaller rotors and shorter blades. Overall, the engine is very constrained by the low turbomachinery efficiencies associated with the heat transfer from the turbine into the compressor. The addition of large bleeds for hydrostatic bearings exacerbates the problem. If the bearings are supplied externally or if the heat transfer can be reduced, the cycle should close. Ultimately, improved engines will require a different turbine cooling scheme or improved turbine materials.

Future Work

The work presented here represents the first steps toward a successful integrated micro engine. However, several additional steps are required to reach that goal. These include steps in fabrication, design, and testing.

The fabrication efforts should focus on improving the match between the specified geometry and the fabricated geometry. In the short term, the most important fabrication areas are rotor uniformity and alignment for imbalance reduction. Once a balanced rotor is demonstrated operating at high speeds, the focus should shift to achieving the taller blades, deeper journal, and deeper combustor originally called for in the 'baseline' demo engine design.

Design efforts should focus on two areas. The first area is simplification and modification of the existing design based on the observed experimental results. Future builds of the turbocharger and demo engine should include a compressor rim seal and an improved journal bearing pressurization scheme. This may require elimination of the through-NGV interconnects. The second area of focus should be on new turbomachinery designs. Preliminary 3D results indicate that the demo engine turbine has low efficiency and is not matched to the compressor. The turbine should be redesigned to achieve matching and higher efficiency. The CFD analyses show that the current high-backsweep compressor design is sensitive to heat addition and has low (0.3-0.4) efficiency. The compressor should be redesigned for low backsweep, improving pressure ratio and mass flow in the face of heat addition while preserving or improving efficiency. A more advanced turbine structure and cooling scheme should also be designed to reduce heat transfer into the compressor flow and boost overall efficiency.

Testing efforts should focus first on achieving high speeds. The addition of a compressor rim seal should allow direct pressurization of the journal bearing. Reduced imbalance should allow die operation at higher speeds. Once higher speeds are achieved, the direct overall spool efficiency should be measured using the scheme outlined in Chapter 6, Experimental Results. The die should then be tested with an operating combustor, demonstrating the first successful operation of a micro engine with integrated combustor and turbomachinery.

7.4 REFERENCES

[1] L. Frechette, *Development of a Silicon Microfabricated Motor-Driven Compressor*, PhD Thesis,
MIT, Department of Aeronautics and Astronautics, 2000

[2] C. C. Lin, *Development of a Microfabricated Turbine-Driven Air Bearing Rig.* PhD thesis, MIT, Department of Mechanical Engineering, 1999.

[3] A. Mehra, *Development of a High Power Density Combustion System for a Silicon Micro Gas Turbine Engine*, PhD thesis, MIT, Department of Aeronautics and Astronautics, 2000.

Table 7-1: Demo Engine Redesign Based on Lessons Learned.

		Baseline		Small Rotor
		Baseline	Redesign	Redesign
Compressor Diameter	[mm]	8	8	5.3
Turbine Diameter	[mm]	6	6	4
Blade Height	[um]	400	400	200
Journal Bearing Depth	[um]	500	300	300
Journal Bearing Type		Hydrodynamic	Hydrostatic	Hydrostatic
Journal Bearing Bleed	[g/sec]	-	0.05	0.03
JB Bleed % Design Core	[%]	-	20%	27%
Combustor Volume				
Combustor Residence Time				
Tt2	[K]	288	288	288
Tt3	[K]	532	601	481
Tt4	[K]	1600	1800	2000
Tt5	[K]	1376	1483	1733
Tt7	[K]	1376	1483	1733
JB Bleed Temp	[K]	-	950	950
Combustor Exit (Tt4) Temp	[K]	1600	1800	2000
Avg. Turbine Inlet (Tt41) Temp	[K]	1600	1630	1720
Compressor mdot	[g/sec]	0.36	0.24	0.12
Compressor PR	[-]	1.80	1.80	1.60
Combustor PR	[-]	0.98	0.98	0.98
Turbine PR	[-]	1.63	1.71	1.55
Nozzle PR (EPR)	[-]	1.08	1.03	1.01
Comp Isen Eff	[-]	0.50	0.50	0.60
Turb Isen Eff	[-]	0.70	0.60	0.50
Combustor Eff	[-]	0.99	0.99	0.99
Bearing Drag	[W]	13.00	5.00	3.33
Heat Transfer	[W]	50.00	-	-
Compressor Bleed	[%]	5%	20%	20%
Turbine Injection***	[%]	-	-	7%
Thrust	[g]	8.79	3.11	0.93
Shaft Power*	[W]	7.60	1.45	0.22
H2 Fuel Burn	[g/hr]	14.62	9.21	5.83
H2 TSFC	[g/g-hr]	1.66	2.96	-
H2 Isp	[sec]	2166	1216	-
H2 PSFC	[g/W-hr]	1.92	6.35	-
Butane Fuel Burn	[g/hr]	40.51	25.53	16.17
Butane TSFC	[g/g-hr]	4.61	8.21	-
Butane Isp	[sec]	782	439	-
Butane PSFC	[g/W-hr]	5.33	17.59	-
Thermal Efficiency**	[%]	2.3%	0.8%	0.2%

* Shaft power assumes continued expansion through turbine

** Thermal efficiency is for turboshaft power output vs fuel energy input.

*** The small rotor cycle does not close and requires turbine injection (shown as a percentage of compressor flow) to reach design speed.

APPENDIX A

MICRO AIR VEHICLE SYSTEM STUDY

This appendix describes a trade study comparing a turbojet-powered micro air vehicle (MAV) to a conventional electrically-powered micro air vehicle.

The best propulsion system for a micro air vehicle is one which optimizes the overall mission-dependent performance of the airplane. A system trade study was performed to compare the relative merits of electric and turbojet propulsion for a micro air vehicle.

The study took as its baseline a design the Lockheed-Martin MicroStar MAV [1]. The study assumed a baseline fixed takeoff weight of 85 grams and compared gross payload (mass of the payload plus payload batteries) versus vehicle endurance at two different flight speeds. The relevant aircraft parameters are summarized in Table A-1. The study assumes that the weight of the airframe, structure, avionics, and avionics batteries are fixed. Two levels of battery performance are considered: (1) an advanced lithium chloride [2] battery with a power density of 0.25 W/g and an energy density of 350 J/g, and (2) a NiCd battery with a power density of 0.25 W/g and an energy density of 175 J/g. Two levels of micro engine performance were considered: (1) A 725 sec Isp hydrocarbon fueled version of the baseline demo engine design studied, and (2) A 1065 sec Isp 'flight engine' evolved from the demo engine. The study compared the endurance of each aircraft as determined by the Breuget range equation.

The results of the study are summarized in Figure A-1. At a flight speed of 15 m/sec, the demo engine-powered MAV and the advanced lithium battery-powered MAV have about equal performance, giving a 20g payload for a 15 min flight. This is approximately twice the payload of a NiCd battery-powered MAV. The flight engine gives a 70% increase in endurance over both

the demo engine and lithium batteries. At 30 m/sec, the NiCd-powered MAV can only cary 10g for 1 minute. By contrast, the lithium batteries offer four times this performance. The demo turbojet offers ten times the performance and the flight engine offers 17 times the performance. At 30 m/sec, a flight engine-powered MAV can carry a 20 gram payload for 30 minutes giving a range of 36 km.

The conclusions of the study are as follows:

(1) For short missions requiring little fuel of battery weight, the lighter weight of the micro engines compares to a motor/propellor combination lead to larger payloads for micro engine powered aircraft.

(2) For very long missions, the aircraft weight is dominated by fuel or battery weight. The higher energy density of a hydrocarbon fuel (~43 MJ/kg) compared to a battery (~0.5 MJ/kg) and the fact that the fuel is consumed, reducing the vehicle weight with time, make even a very low-performance turbojet competitive with the best batteries.

(3) As flight speed increases above 15 m/sec, turbojet propulsion rapidly outperforms electric propulsion.

A.1 REFERENCES

[1] J. Harris, Private Communication via A. H. Epstein, Oct. 1998.

[2] D. C. Johnson *et al*, "Micro Air Vehicle Mission and Technology Assessment," Project Report MAV-1, Lincoln Laboratory, Lexington, MA, Nov. 1997.

Table A-1: MAV Design Parameters Used for System Study.

Lift-to-drag ratio	5:1
Gross takeoff weight (fixed)	85 grams
Weight of structure	7 grams
Weight of non-payload avionics	16 grams
Electric motor and propeller	13.5 grams
Electric to propulsive effic.	37%
2 micro engines + accessories	11 g

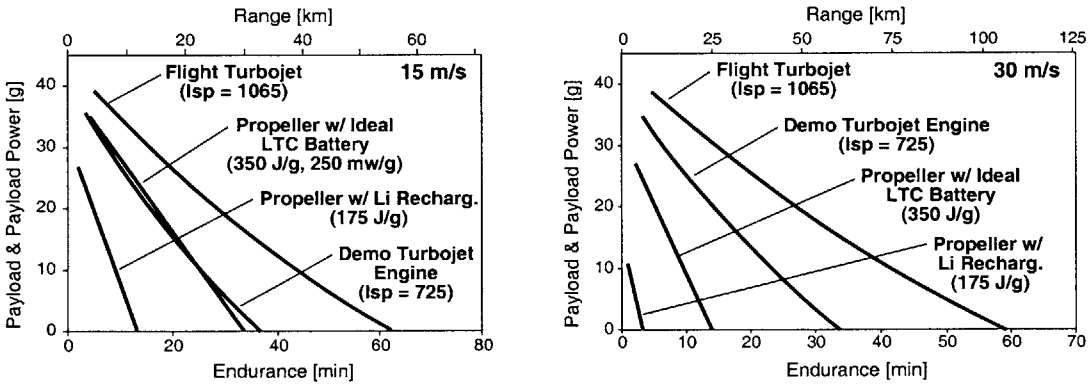

Figure A-1: Results of MAV propulsion trade study.

APPENDIX B

CYCLE ANALYSIS SPREADSHEET

This appendix contains the Excel spreadsheet used for cycle calculations.

File: sens6b_official_PhD_thesis_rev2.xls -- Demo Engine performance for thesis.
Author: J. Protz
Updated: 10-Apr-00
Notes: This study uses the 'reference cycle' used in gasturb pltos

			Low OPR = 1.8		High OPR = 3	
			Nominal	No Heat	Nominal	No Heat
Parameters	Rair	[kJ/kg-K]	0.287	0.287	0.287	0.287
	gamma_c	[-]	1.400	1.400	1.400	1.400
	gmoog_c	[-]	0.286	0.286	0.286	0.286
	1/gmoog_c	[-]	3.500	3.500	3.500	3.500
	cp	[kJ/kg-K]	1.005	1.005	1.005	1.005
	R_exhaust	[-]	0.289	0.289	0.289	0.289
	gamma_c	[-]	1.280	1.280	1.280	1.280
	gmoog_c	[-]	0.219	0.219	0.219	0.219
	1/gmoog_c	[-]	4.571	4.571	4.571	4.571
	cp	[kJ/kg-K]	1.320	1.320	1.320	1.320
	Tt_inlet	[K]	288.0	288.0	288.0	288.0
	H2 h_fuel	[kJ/g]	120.0	120.0	120.0	120.0
	HC h_fuel	[kJ/g]	43.4	43.4	43.4	43.4
Inputs	mdot	[g/sec]	0.36	0.36	0.36	0.36
	OPR	[-]	1.80	1.80	3.00	3.00
	eff_c	[-]	0.50	0.50	0.65	0.65
	eff_t	[-]	0.70	0.70	0.70	0.70
	shaft offtake	[W]	13.0	13.0	5.0	5.0
	Tt4	[K]	1600	1600	1600	1600
	Combustor PR	[-]	0.98	0.98	0.98	0.98
	bleed	[%]	5%	5%	5%	5%
	Heat Transfer	[W]	50.0	0.0	50.0	0.0
	Burner Eff	[-]	0.99	0.99	0.90	0.90
	Recup eff	[-]	0.00	0.00	0.00	0.00
Intermediate	bleed mdot		0.018	0.018	0.018	0.018
Variables	turbine mdot		0.342	0.342	0.342	0.342
	Comp Work	[W]	38.1	38.1	59.1	59.1
	Turbine Work	[W]	51.1	51.1	64.1	64.1
	Comb Exit P	[atm]	1.76	1.76	2.94	2.94
	Turbine PR	[-]	0.61	0.61	0.54	0.54
	Heat Transfer	[W]	50.0	0.0	50.0	0.0
	Turbine TR		0.86	0.93	0.84	0.91
	EPR		1.08	1.08	1.58	1.58
	Exit Tt		1376	1487	1347	1458
	Exit Mach numbe	[-]	0.36	0.36	0.87	0.87
	Exit Tstatic		1352	1461	1219	1319
	Exit Vel	[m/sec]	252	262	583	606
	Compressor Tt_exit		473	368	518	412
	Burner Power	[W]	514	562	543	596
	Fuel/Air Ratio	[-]	0.01252	0.01369	0.01323	0.01452
	Recup Heat	[%]	0.00000	0.00000	0.00000	0.00000
Output	Thrust Power	[W]	10.86	11.73	58.09	62.86
	Turboshaft Powe	[W]	7.60	8.21	40.66	44.01
Variables	Thrust Force	[N]	0.086	0.090	0.199	0.207
	Thrust Force	[gf]	8.8	9.1	20.3	21.2
Core	Fuel Burn (H2)	[g/hr]	15.4	16.9	16.3	17.9
Performance	TSFC	[g/hr/gf]	1.8	1.8	0.8	0.8
	Isp	[sec]	2054	1953	4495	4262
	PSFC	[g/w/hr]	2.03	2.05	0.40	0.41
	Fuel Burn (HC)	[g/hr]	42.71294	46.70202	45.142	49.52999
	TSFC	[g/hr/gf]	4.85662	5.108583	2.219374	2.340792
	Isp	[sec]	741	705	1622	1538
	PSFC	[g/w/hr]	5.62	5.69	1.11	1.13
Device	Generator Efficie	[%]	0.3	0.3	0.5	0.5
Performance	Electrical Power	[W]	2.280689	2.464256	20.33128	22.00265
	Overal PSFC	[g/w/hr]	18.72809	18.95178	2.220322	2.251092
	Specific Energy	[w-hr/kg]	53.39573	52.7655	450.3851	444.2289
	uEng/Battery		0.305118	0.301517	2.573629	2.538451
	Thermal Eff	[%]	0.021353	0.021101	0.118874	0.117249
TurboJet	Cruise Speed	[m/sec]	15	15	15	15
	mdot/mdot_fuel/ç	[-]	3.043366	2.792131	2.885096	2.638538
	Isp_static	[sec]	741	705	1622	1538
	Isp_correction	[sec]	46	42	43	40
	Isp_cruise	[sec]	696	663	1579	1498
	Cruise/Static	[-]	0.938415	0.940567	0.97332	0.974266
	Fuel Power		514	562	543	596
			508.6043	556.1043	488.6621	536.1621
			10.86	11.73	58.09	62.86
			0.8	0.8	0.8	0.8

APPENDIX C

TURBINE COOLING MODEL

This appendix describes the 1-D turbine structural cooling model.

The demo engine spool (compressor, turbine, and shaft) is a geometrically complicated structure with a variety of flow passages. Each surface of the spool is exposed to a different gas temperature and heat transfer coefficient. The flow temperatures are influenced by the structural temperatures. The result is a coupled structures-fluids problem. A comprehensive analysis of this structure would require a 3D FEM thermo/structure analysis similar to the analyses performed by Chen and Huang. A separate analysis of the flow would also be required. The FEM and fluids calculations would be iterated until a final solution is determined.

A full 3D thermal/structure/fluids analysis of the spool is too complicated to be practical for trade studies. Instead, a much simpler 1D model was developed. This model uses bulk heat transfer coefficients for the turbine and the compressor. Both structures are considered isothermal. A linear thermal gradient is assumed in the shaft connecting the turbine to the compressor. The fluids/thermodynamics problem is solved simultaneously with the thermal/structure problem. Compressor performance with heat addition is modeled using the correlation from chapter 3, Component Design.

The model uses the following assumptions:

(1) Compressor blisk is isothermal

(2) Turbine blisk is isothermal

(3) Linear thermal gradient in shaft

(4) 'Bulk' heat transfer coefficients are independent of flow or structural temperature

(5) Compressor performance changes with compressor heat flux according to correlation from Chapter 3.

(6) Rotor speed fixed at 125,000 rad/sec

(7) Heat transfer at blade tips, seals, and journal bearing negligible.

The problem is set up as a thermal resistance problem. The following models are used in the analysis:

(1) Compressor heat transfer. Heat transfer in the compressor is modeled by a 'bulk' heat transfer coefficient that relates heat flux to isothermal wall temperature and average compressor fluid temperature. Here, T_bar_c_fluid is the average blade-relative total temperature of the flow.

$$\dot{Q}_c = h_c \cdot A_c^{wet} \cdot (T_c^{wall} - \overline{T}_c^{fluid})$$

(2) Turbine heat transfer. Turbine heat transfer is also modeled by a 'bulk' heat transfer coefficient. Again, the fluid temperatures are in the blade-relative frame.

$$\dot{Q}_t = h_t \cdot A_t^{wet} \cdot (T_t^{wall} - \overline{T}^{fluid})$$

(3) Conduction in the shaft. The conductive heat transfer from the turbine to the compressor via the shaft is modeled by the following equation:

$$\dot{Q}_{shaft} = \frac{k \cdot A^{x\sec}}{l} \cdot (T_t^{wall} - T_c^{wall})$$

(4) Enthalpy rise in the compressor. Enthalpy rise in the compressor is given by the sum of the compressor shaft work (taken from correlation with Qdot) and the heat transfer. Here, T_{t2} is the absolute-frame impeller inlet total temperature, and T_{t25} is the absolute-frame impeller exit total temperature.

$$c_p \cdot \dot{m}_c \cdot (T_{t25} - T_{t2}) = W_c(\dot{Q}_c) + \dot{Q}_c$$

(5) Enthalpy drop in the turbine. The enthalpy drop in the turbine is given by the sum of the turbine shaft work and the heat flow out of the turbine. The turbine work is equal to the sum of the compressor work (a function of Qc) and the bearing and seal drag losses (approximately 13W). Here, T_{t41} is the absolute-frame NGVexit temperature and T_{t5} is the turbine rotor exit temperature.

$$c_p \cdot \dot{m}_t \cdot (T_{t41} - T_{t5}) = W_t + \dot{Q}_t$$

These equations are solved simultaneously along with the conservation of energy to determine the spool temperatures and heat transfer. The specific values used for each parameter are summarized in the table shown on the next page.

File: heattxfrgeomspec.xls -- Excel spreadsheet to define heat transfer calc parameters
Author: J. Protz
Date: 10 Dec 98

Geometry		Comp	Turb
Donut' Area	[mm2]	37.70	21.21
Blade Tip Plan Area'	[mm2]	21.88	2.12
Wetted Endwall Area*	[mm2]	15.82	19.08
Blade Wetted Area	[mm2]	36.04	13.97
Total Wetted Area	[mm2]	51.85	33.05
Total Wet/Donut**	[-]	1.38	1.56
Tip Plan/Donut	[-]	0.58	0.10
Fraction Holes	[-]	0.42	0.90
Total Wet/Blade Wet***	[-]	1.44	2.37

* Area of rotor side only. Does not include static casing.
** Use this to correct axisymmetric rotor model
** This is 3D wetted area / 2D wetted area

Heat Transfer			
h*	[W/m2-K]	1817.00	2580.00
hA-2D**	[W/K]	0.0654	0.0360
hA-3D	[W/K]	0.0942	0.0852

* Based on Guppy's 2D MISES. Consistent w/ Luc's Fluent 2D and Stu's analytic soln to +/- 15%
** 2D Mises w/ no endwall heat transfer
*** hA is 'bulk' Q = hA*0.5*(Tt_rel_in+Tt_rel_exit)

Fluid Temperatures			
Inlet Total Tempereature (Absolute)	[K]	300.00	1600.00
Inlet Total Tempereature (Relative)	[K]	362.00	1493.00
Relative-Absolute	[K]	62.00	-107.00
Work	[W]	40.00	53.00
Work/Cp*mdot	[K]	110.56	129.14
Heat	[W]	40.00	40.00
Heat/Cp*mdot	[K]	110.56	97.47
Exhaust Total Temperature (Absolute)	[K]	521.12	1373.39
Exhaust Total Temperature (Relative)	[K]	552.12	1384.39
Relative-Absolute	[K]	31.00	11.00
'Avg' Total Temperature (Absolute)	[K]	410.56	1486.70
'Avg' Total Temperature (Relative)	[K]	457.06	1438.70
Relative-Absolute	[K]	46.50	-48.00

* Static structures should use absolute frame. Rotating structures should use relative frame.

APPENDIX D

CROSS-JOURNAL TAB EXPERIMENTS

This appendix describes the development of 'cross-journal' tabs for rotor retention in a microengine.

Motivation and Approach

Demo engines require a mechanism to keep the rotating components (rotors) attached to the rest of the silicon wafer during processing while still allowing the rotors to be released once processing is complete.

The demo engine process was originally envisioned as a parallel wafer process. In a purely parallel process, each wafer is processed entirely independently of the other wafers in the stack. All six wafers are then bonded simultaneously to create a device stack. Existing rotor retention schemes require processing on a bonded pair because the rotor is defined after one or more wafers are bonded. An attempt was made to apply the concept of rotor retention tabs to a parallel wafer demo engine process by using intra-wafer "cross-journal" tabs.

Under the cross-journal tab scheme, the blade etch also defines tabs that span the rotor's journal bearing gap. In principle, these tabs anchor the rotor to the static structure, retaining it during subsequent fabrication steps, including bonding. The tabs are accessible from outside the die through view ports in the intermediate layers. The tabs may be broken off mechanically or they may be etched with laser assist (LAE).

Results and Conclusions

A tradeoff between mechanical strength and tab conspicuity drives tab size. Larger tabs are stronger, but they are also more difficult to remove and have a larger impact on the rotor structure. Initially, the tabs were sized to provide sufficient strength to survive processing. Calculations showed that 50 um wide tabs on the turbine and 75 um wide tabs on the compressor would be adequate to survive spin rinsing, a mechanically aggressive step in the fabrication process. However, these small tabs were almost invariably destroyed during the deep etching process. The small tabs were replaced with 100 um "fat tabs." The "fat tabs" were successful on the turbine wafer with its 20 um wide journal bearing. Figure XX illustrates a tab-retained turbine. The fat tabs were unsuccessful on compressor wafer with its 30 um gap. This led to several failed compressor builds. Ultimately, a special compressor tab experiment was performed with 12 different types varying in width from 100 um to 300 um and varying in length from 175 um to 325 um. Figure XX shows an SEM of an experimental die. The compressor tab experiment showed that 150 um wide by 325 um long tabs were the best. Narrower tabs were attacked during etching. Fatter tabs were too difficult to break off for rotor release.

The break-off tabs demonstrated unusual etch behavior. X. Zhang, R. Khanna, and A. Ayon studied the tab etching process for journal-then-tab etches. Their results showed that the tab etch has three possible phases. Initially, the tab etch has not reached the journal etch and the tabs are well-defined post-like features with straight side walls. These are "under-etched" tabs. Once the tab etch has passed the journal, the tab bridges the journal gap. At this point, the tab side walls deteriorate and become reentrant. The tab takes on a wedge-like shape. These are "over-etched" tabs. If the etch proceeds long enough, the "over-etched" tab pinches off and fails. Between these two phases, when the tab etch has exactly reached the journal, the tab still retains good definition with straight side walls, but it also bridges a fully open journal gap. These are "exactly-etched" tabs. Figure D-2 illustrates the three tab phases. The over-etched tabs cause poor yield due to rotor loss. The under-etched tabs cause poor yield due to inability to release the rotor. The etching time separating under-etched tabs from over-etched tabs is approximately 15 min. Because the tab etch is non-uniform, this virtually guarantees a low-yield mixture of over-etched, exactly-etched, and under-etched tabs on a single wafer.

Despite their parallel process appeal, the "cross-journal" tabs proved extremely difficult to implement. They required over six months of development time and, even then, proved generally unsatisfactory. The break-off process leaves debris and introduces cracks into the rotor. The tabs residuals are manifested as "bumps" on the rotor rather than "divots" and are, therefore, less of a structural concern. Nevertheless, they do contribute to rotor imbalance. Most significantly, the aforementioned etch sensitivity of the tabs made them unreliable during processing. Tabs would fail during all stages of processing including etching, cleaning, and bonding. Zero yields on a single wafer were not uncommon.

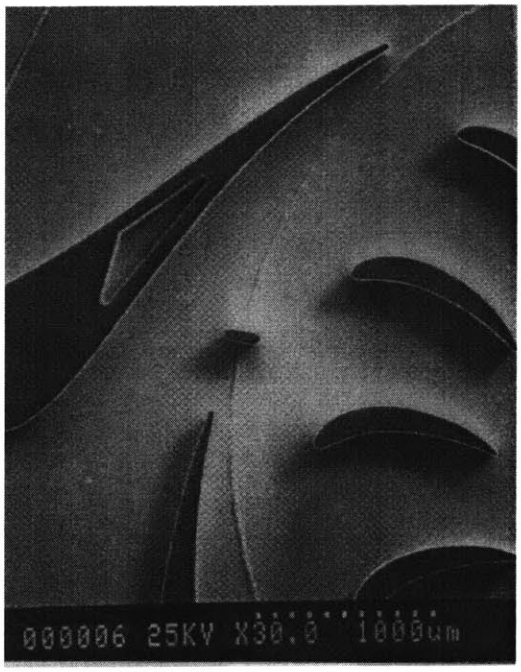

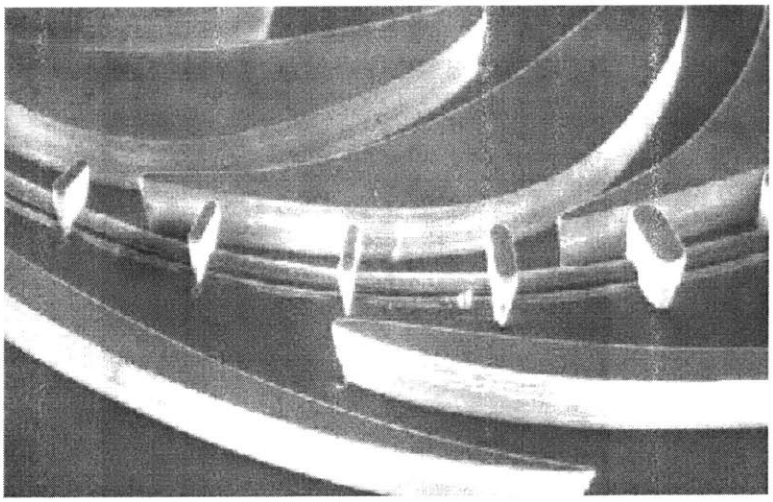

Figure D-1: Tab-retained turbine (production) and compressor (experiment).

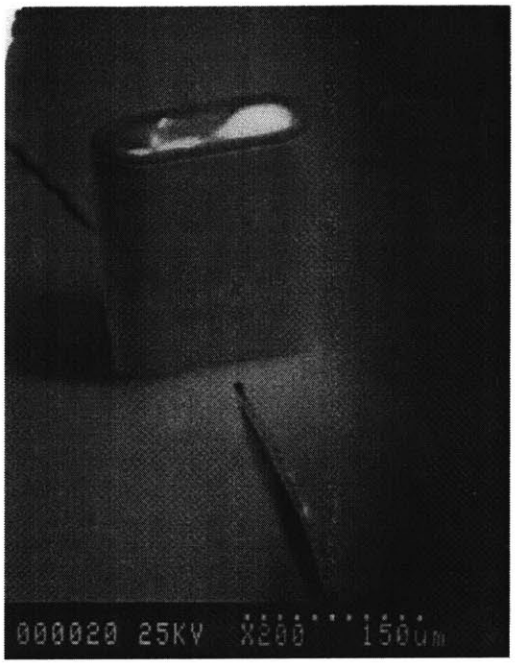

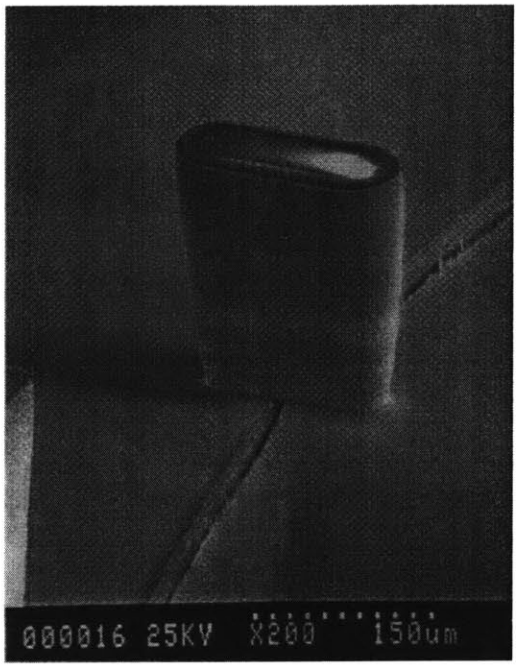

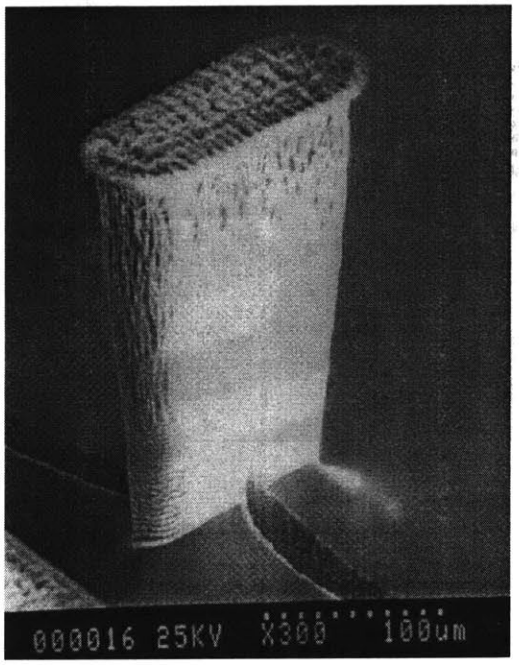

Figure D-2: SEMs of under-etched, exactly etched, and over-etched tabs (cw from top left)